

## **ABSTRACT**

ZENG, XIANGMING. Classification and Predictability of the Western Boundary Current Variability in the Gulf of Mexico and South Atlantic Bight. (Under the direction of Dr. Ruoying He).

Many instabilities exist in the western boundary current system in the North Atlantic, such as path shifts, meanders and eddy shedding. Regional climate systems, local weather systems and marine ecosystems can be significantly affected by these instabilities. Using state-of-art methods, this dissertation explores different patterns, predictability, and mechanisms of two major components of the Western Boundary Current system in the North Atlantic: the Loop Current (LC) in the Gulf of Mexico (GoM) and the Gulf Stream (GS) in the South Atlantic Bight (SAB).

First, variations of the LC in the GoM are investigated using over two decades of satellite altimeter data and the self-organizing map method. It is found that LC variations can be characterized by three spatial patterns: normal, extension and retraction. The corresponding temporal variations confirm that LC eddy shedding generally occurs during the transition from the extension to retraction patterns. On the weekly time scale, the wind stress curl (WSC) in the Caribbean Sea has a major influence on LC eddy shedding. The increase of Caribbean WSC from June to November favors more frequent LC eddy shedding during that period. On the interannual time scale, there is a potential linkage between the frequency of LC eddy shedding and El Niño activities.

Based on such analysis of the LC variation, a LC sea surface height (SSH) prediction system is developed to forecast the variation of the LC status and eddy shedding process. The empirical orthogonal function analysis method is first applied to decompose long-term

satellite-observed SSH into spatial patterns (EOFs) and time-dependent principal components (PCs). Then the nonlinear autoregressive neural network is developed to predict major PCs of the GoM SSH in the future. The prediction of SSH in the GoM is subsequently constructed by multiplying the EOFs and predicted PCs. Validations against independent satellite observations indicate that the neural network-based model can reliably predict the LC variations and its eddy shedding process for a 4-week period. In some cases, an accurate forecast for 5–6 weeks is possible.

The last part of this dissertation focuses on the variability of the GS path in the SAB and its corresponding mechanisms. Both long-term satellite observation analysis and advanced primitive equation ocean models are applied. Statistical analysis of long-term satellite altimeter observations shows the GS path has two modes in the SAB: weakly and strongly deflected. Over the last two decades, the largest GS offshore deflection in the SAB occurred in November 2009– April 2010. The triggering mechanisms are studied using both the forward and the adjoint modules of the Regional Ocean Modeling System (ROMS). The forward model simulation reasonably well captures the GS deflection in November 2009. The adjoint sensitivity analysis further reveals that a net increase of positive relative vorticity  $\zeta$  near the Charleston Bump generated by the dynamic interaction between the increased GS volume transport and the local bathymetry triggered the GS offshore deflection by virtue of conserving the potential vorticity  $(f + \zeta)/h$ . Quantitative vorticity analysis confirms such a finding.

© Copyright 2016 Xiangming Zeng

All Rights Reserved

Classification and Predictability of the Western Boundary Current Instabilities in the Gulf of Mexico and South Atlantic Bight

by  
Xiangming Zeng

A dissertation submitted to the Graduate Faculty of  
North Carolina State University  
in partial fulfillment of the  
requirements for the degree of  
Doctor of Philosophy

Marine, Earth, and Atmospheric Sciences

Raleigh, North Carolina

2016

APPROVED BY:

---

Dr. Ruoying He  
Chair of Advisory Committee

---

Dr. John Bane

---

Dr. Ping-Tung Shaw

---

Dr. Fredrick Semazzi

---

Dr. Nagiza Samatov

## **DEDICATION**

To people, who are still on the road.

## **BIOGRAPHY**

Xiangming Zeng was born and raised in a small village in Shandong, China. He received his bachelor degree in Mathematics in 2007 at Ocean University of China and master degree in Physical Oceanography in 2010 at Second Institute of Oceanography, China State Oceanic Administration. After working two years as a research associate in the same institute, he joined the Department of Marine, Earth, and Atmospheric Sciences at North Carolina State University in August 2012 to start his doctoral study.

Xiangming are very interested in using data and models to solve real world problems. He loves the elegant math behind models and fascinating ideas of exploring and explaining data. He'd like to use what he has learned to make the world a better place.

Xiangming passed his Ph.D. preliminary exams in April 2015, and is expected to complete his Ph.D. degree in July 2016.

## ACKNOWLEDGMENTS

I would like to thank my advisor, Dr. Ruoying He, for his continuous support of my Ph.D. research. I am very grateful to my committee: Dr. Ruoying He, Dr. John Bane, Dr. Ping-Tung Shaw, Dr. Fredrick Semazzi, and Dr. Nagiza Samatova, for their valuable guidance and suggestions. I would also like to thank all the current and past members of Ocean Modeling and Observing Group, Ms. Jennifer Warrillow, Dr. Joseph Zambon, Dr. Jeffrey Willison, Dr. Benjamin Johnson, Dr. Yanlin Gong, Dr. Haibo Zong, Ms. Laura McGee, Dr. Ke Che, Dr. Yizhen Li, Dr. Ping Zhai, Dr. Austin Todd, Dr. Yi Xu, Dr. Zhiren Wang, Dr. Zhigang Yao, Dr. Zuo Xue, Dr. Yuqi Yin, Dr. Chuanjun Du, Dr. Hui Qian, and others who gave me a lot of help during my Ph.D. study. Many thanks to the faculties, staffs, and friends in the Department of Marine, Earth, and Atmospheric Sciences, especially Dr. Paul Liu, Dr. Bin Liu, Xiaoyu Long, Yao Wang, Doreen McVeigh, and many other friends in my life, who made my life more colorful.

Finally, I would like to thank my wife, parents, sisters, and other family members for their consistent support and understanding. Without them, I cannot go this far.

## TABLE OF CONTENTS

<b>LIST OF TABLES .....</b>	<b>vii</b>
<b>LIST OF FIGURES .....</b>	<b>viii</b>
<b>Chapter I: Introduction.....</b>	<b>1</b>
<b>1. Western Boundary Current instabilities .....</b>	<b>1</b>
<b>2. Loop Current in the Gulf of Mexico .....</b>	<b>2</b>
<b>3. Gulf Stream in the South Atlantic Bight .....</b>	<b>4</b>
<b>4. Research objectives and dissertation outline.....</b>	<b>7</b>
<b>References .....</b>	<b>9</b>
<b>Figures.....</b>	<b>15</b>
<b>Chapter II: Clustering of Loop Current patterns based on the satellite-observed sea surface height and self-organizing map .....</b>	<b>17</b>
<b>Abstract.....</b>	<b>18</b>
<b>1. Introduction.....</b>	<b>18</b>
<b>2. Data and methods .....</b>	<b>20</b>
<b>3. Results .....</b>	<b>21</b>
3.1 Spatial variability .....	22
3.2 Temporal evolution.....	22
<b>4. Discussion .....</b>	<b>23</b>
<b>5. Summary.....</b>	<b>25</b>
<b>Acknowledgement.....</b>	<b>26</b>
<b>References .....</b>	<b>27</b>
<b>Figures.....</b>	<b>31</b>
<b>Chapter III: Predictability of the Loop Current variation and eddy shedding process in the Gulf of Mexico using an artificial neural network approach .....</b>	<b>35</b>
<b>Abstract.....</b>	<b>36</b>
<b>1. Introduction.....</b>	<b>36</b>
<b>2. Data and method.....</b>	<b>39</b>

2.1 Dataset.....	39
2.2 Artificial neural network (ANN) .....	40
2.3 EOF analysis.....	41
2.4 Prediction Procedure.....	42
<b>3. Results and discussion .....</b>	<b>45</b>
3.1 Sensitivity of PC number selection.....	45
3.2 SSH prediction skill assessment .....	46
3.3 Frontal position prediction skill assessment .....	49
3.4 One LC eddy shedding example.....	51
<b>4. Summary.....</b>	<b>52</b>
<b>Acknowledgement.....</b>	<b>54</b>
<b>References.....</b>	<b>54</b>
<b>Tables .....</b>	<b>61</b>
<b>Figures.....</b>	<b>62</b>
<b>Chapter IV: Gulf Stream variability and a triggering mechanism of its large meander in the South Atlantic Bight.....</b>	<b>76</b>
<b>Abstract.....</b>	<b>77</b>
<b>1. Introduction.....</b>	<b>77</b>
<b>2. Gulf Stream path variation over the last two decades.....</b>	<b>80</b>
2.1 Gulf Stream path detection .....	80
2.2 Self-Organizing Map analysis.....	82
<b>3. Triggering mechanism analysis .....</b>	<b>84</b>
3.1 Ocean model configuration and validation.....	84
3.2 Adjoint sensitivity model.....	86
3.3 Forward model results.....	90
3.4 Validity of tangent linear assumption and index function definition .....	92
3.5 Adjoint sensitivity analysis.....	94
<b>4. Barotropic vorticity budget.....</b>	<b>96</b>
<b>5. Summary.....</b>	<b>98</b>

<b>Acknowledgement</b> .....	<b>100</b>
<b>References</b> .....	<b>101</b>
<b>Figures</b> .....	<b>109</b>
<b>Chapter V: Summary</b> .....	<b>126</b>

## LIST OF TABLES

Table 1. Principal Component (PC) number settings for Gulf of Mexico (GoM) sea surface height and corresponding time-averaged (2010-2013) spatial correlation coefficients (**bold numbers**) and root mean square errors (unit: m) between prediction and observation. PC percentage is the percentage variance accounted for by different PCs. 61

# LIST OF FIGURES

## Chapter I

Figure 1. (a) Eddy kinetic energy ( $\text{m}^2/\text{s}^2$ ) derived from 21 years' mean AVISO sea level anomaly satellite data. (b) Study domain. Black arrows are geostrophic currents ( $> 0.1$  m/s) derived from 21 years' mean AVISO sea surface height data. They can be considered to be part of the Western Boundary Current system in the North Atlantic. Contours are isobaths at 100, 1000, and 3000 m. .... 15

Figure 2. Topography of the South Atlantic Bight. Water depth is shown in meters. Contours are 200, 600, 700, 1000, and 3000 m isobaths. The Charleston Bump is shown by the arrow. .... 16

## Chapter II

Figure 1. Study domain. Red box is the Gulf of Mexico (GoM) area; blue box is the Caribbean Sea (CS) area; green box is the Bahamas area. The box areas are used for wind stress curl calculations. Grey lines are depth contours in meters. Black arrows are geostrophic velocity calculated from long-term mean AVISO sea surface height data (only the velocities  $> 0.1 \text{ m s}^{-1}$  are plotted). The Loop Current is visible via the velocity arrows in the GoM box. .... 31

Figure 2. Self-organizing map analysis results. (a) Sea surface height (SSH) patterns: (P1) normal; (P2) extension; (P3) retraction. Top numbers are corresponding frequency of occurrence (FO) percentage. Vectors are geostrophic current. Green line is 0.45 m SSH contour line. Cyan lines are 1000 m isobaths. Color scale: SSH in meters. (b) Best matching unit (BMU) time series of the three patterns in (a). Red stars are the first day of each year. (c) Monthly FOs of the three patterns in (a). .... 33

Figure 3. (a) Weekly frequency of occurrence (WFO) for Pattern 3 (P3) and wind stress curl of the areas in Figure 1. Zero-lag correlation coefficients ( $r$ ) for the relation between the WFO of P3 and the wind stress curl, at 95% confidence level for each domain, are shown in brackets after the domain. (b) Normalized Ocean Niño Index (six-month moving average; shaded area) and annual mean frequency of occurrence (FO) for P3 (green line). Correlation coefficient ( $r=0.6$ ) with Ocean Niño Index lagged 90 days is shown at 95% confidence interval. .... 34

### Chapter III

Figure 1. Study domain. Black box is study area in the Gulf of Mexico (GoM). Stars are the seven reference stations for frontal position comparison. Grey lines are depth contours in meters. Black arrows are geostrophic velocity calculated from long-term mean AVISO sea surface height data (only the velocities  $>0.1$  m/s are plotted). The Loop Current is visible via the velocity arrows in the GoM box. Dash lines are tracks of hurricanes or tropical storms (TS) from July 2010 to July 2013. 1: TS Bonnie, July 22-25, 2010; 2: Hurricane Paula during October 11-15, 2010; 3: TS Don, July 27-30, 2011; 4: Hurricane Rina, October 22-29, 2011; 5: TS Debby, June 23-27, 2012; 6: Hurricane Ernesto, August 1-10, 2012; 7: Hurricane Isaac, August 20-30, 2012; 8: TS Andrea, June 5-10, 2013. The tracks of hurricanes and tropical storms are from NOAA National Climatic Data Center and The Johns Hopkins University Applied Physics Laboratory. 62

Figure 2. Comparison between predicted (circles) and observation-derived (stars) first leading principal component of GoM SSH from 2010 to 2013. Correlation coefficients are presented at the top of each figure. .... 64

Figure 3. Spatial correlation coefficients (CC) and root mean square errors (RMSE) of predicted and observed sea surface height in the study area from 2010 to 2013 with a six-week ahead weekly sliding prediction window, using 18 PCs. Circles are CC points, and triangles are RMSE points. Red lines in week 6 indicate the approximate passing time of Hurricane Rina in 2011, Hurricane Ernesto in 2012, and Tropical Storm Andrea in 2013. .... 66

Figure 4. Root Mean Square Error (RMSE) comparison of sea surface height between prediction (red) and persistence (black). Circles represent the location of week 1. The values are plotted every four weeks. .... 67

Figure 5. Averaged Root Mean Square Error (RMSE) of sea surface height for prediction (red) and persistence (grey). Thin lines are monthly means, and thick lines are means over the three-year prediction period. .... 68

Figure 6. Skill score comparison of sea surface height between prediction (red) and persistence (black). Circles represent the location of Week 1. The values are plotted every four weeks. Grey short lines represent the approximate passing time of hurricanes or tropical storms in Figure 1. Blue short lines indicate the time of Loop Current eddy shedding. .... 69

- Figure 7. Averaged skill score of sea surface height for prediction (red) and persistence (grey). Thin lines are monthly mean, and thick lines are means over the three-year prediction period. .... 70
- Figure 8. Frontal position Root Mean Square Error (RMSE) comparison of Loop Current and Loop Current eddies between prediction (red) and persistence (black). Circles represent the location of Week 1. The values are plotted every four weeks. .... 71
- Figure 9. Averaged frontal position Root Mean Square Error (RMSE) for prediction (red) and persistence (grey). The sudden jumps in Figure 8 were excluded when the average was calculated. Thin lines are monthly means, and thick lines are means over the three-year period. .... 72
- Figure 10. Comparison between forecasted and observed sea surface height in week 1-2 (panel A), week 3-4 (panel B), week 5-6 (panel C), representing a complete cycle of one Loop Current (LC) eddy shedding event. Black lines are 1000 m isobaths. Red areas are the LC and LC eddies. Green solid lines are 0.45 m contours for observation, and 0.51 m contours for prediction. Green dashed lines are the track of Tropical Storm Don during July 27-30, 2011. .... 75

#### **Chapter IV**

- Figure 1. Model domain. Black arrows are geostrophic currents ( $> 0.1$  m/s) derived from 21 years of mean AVISO Absolute Dynamic Topography data. They can be considered as the western boundary current system in the North Atlantic. Contours are 100, 1000, and 3000 m isobaths. .... 109
- Figure 2. Topography of the South Atlantic Bight. Water depth is shown in meters and extracted from the 1-minute GEBCO dataset. The Charleston Bump is indicated. .... 110
- Figure 3. Long-term (1993-2013) mean Absolute Dynamic Topography (ADT, color shading, unit: m) overlaid with Gulf Stream mean path (solid black curve) and corresponding envelope (dashed cyan curves) and one standard deviation (STD, dashed black curves). Transects 1 to 5 (solid lines perpendicular to the Gulf Stream mean path) were used to measure the position variation of the Gulf Stream. Gray contours are 200, 600, 1000, and 2000 m isobaths. Black box is for the index function definition in section 3. Florida (FL) and the Charleston Bump are indicated. .... 111
- Figure 4. Gulf Stream position relative to its mean path along each transect in Figure 3 (unit: km). Offshore direction is positive (gray), while onshore is negative (black). Blue

shaded region indicates the largest offshore event in 2009-2010. A 30-day low-pass filter was applied to the original data for visualization purpose. .... 113

Figure 5. Self-Organizing Map analysis of the Gulf Stream path in the South Atlantic Bight. (a) Weakly (P1) and strongly (P2) deflected patterns. The numbers are corresponding frequency of occurrence (FO) for each pattern. The mean path is indicated by the cyan curve. (b) Monthly FOs of the two patterns in (a). .... 114

Figure 6. Comparisons between Florida Current (FC) transport and monthly FO of strongly deflected pattern (P2). (a) Monthly mean FC transport ( $S_v$ ) and FO of P2 (%). Correlation coefficient is -0.81. (b) Monthly standard deviation (STD) of FC transport ( $S_v$ ) and FO of P2 (%). Correlation coefficient is 0.66. .... 115

Figure 7. Observed (blue) and simulated (red) daily sea level at three stations (a, b, and c) along the SAB, and water transport through the Florida Straits (d). Sea level data are normalized (minus mean divided by the corresponding standard deviation). Locations of the three stations and the FC transect is shown in Figure 8a. .... 117

Figure 8. Simulated surface velocity (vectors) and relative vorticity (color shading) from Nov. 17 to 26, 2009, every three days. Relative vorticity is normalized by dividing by the Coriolis parameter. Black stars in (a) indicate the location of the three sea level stations, and black hexagon represents Abaco Island. Purple solid line in (a) represents the location of the cable measuring the Florida Current (FC) transport. Black box (same as the one in Figure 3) delineates the region for index function calculation. Gray lines are the 200, 600, 1000, and 2000 m isobaths. The purple, red, and yellow transects in (a) are sites where water transport was calculated for the FC, Antilles Current, and Gulf Stream, respectively. .... 118

Figure 9. Simulated water transport through the three transects in Figure 8a. These indicate the water transport of Florida Current, Antilles Current, and Gulf Stream. .... 119

Figure 10. Comparisons between the nonlinear perturbation runs and tangent linear model solutions in terms of sea surface height (SSH) and velocity ( $u$  and  $v$ ). Gray lines represent the 50 perturbation experiments, and solid black lines are the corresponding mean. .... 120

Figure 11. Comparison between daily mean sea surface height (SSH, blue) in the box and Gulf Stream (GS) position (red) relative to the mean path along transect 2 in Figure 3.

The dashed rectangular box indicates the time window for adjoint sensitivity analysis. .....	121
Figure 12. Adjoint sensitivity to depth-averaged velocity. Vectors represent direction. Color indicates magnitude (unit: 1/s). Gray lines are the 200, 600, 1000, and 2000 m isobaths. Black boxes are the region for index function calculation. ....	122
Figure 13. Schematics of positive relative vorticity perturbation formation. Orange circles with plus signs indicate positive relative vorticity. Blue circles with minus signs represent negative relative voracity. Vectors are velocity fields. Shaded ellipse represents the Charleston Bump. ....	123
Figure 14. Ten-day (Nov. 17-26, 2009) averaged tendency, planetary vorticity advection (BETA), bottom pressure torque (BPT), and nonlinear advection (ADV) terms in the barotropic vorticity equation (unit: m/s <sup>2</sup> ). Gray lines are the 200, 600, 1000, and 2000 m isobaths. Cyan lines are the 1, 21, and 41 Sv batrotropic streamlines (integrated from coastlines). Green boxes define the region for the time series plot in Figure 16. Black boxes indicate the region for the index function calculation. ....	124
Figure 15. Spatial averaged terms of the barotropic vorticity equation (Eq. 11) within the green box in Figure 14 (unit: m/s <sup>2</sup> ). ....	125

# Chapter I: Introduction

## 1. Western Boundary Current instabilities

Some of the most prominent features of ocean circulation are the strong, persistent currents along the western boundaries of ocean basins, which are known as Western Boundary Currents (WBCs), such as the Gulf Stream in the Atlantic and Kuroshio Current in the Pacific. The formation of WBCs is mainly due to the beta effect of the Coriolis force varying with latitude (Stommel 1948). Originating from the equatorial regions, WBCs carry warm water from low to high latitudes, thus not only affecting the local circulation and marine ecosystem, but also contributing to the global meridional heat transport and moderation of Earth's climate (Imawaki et al. 2013).

WBCs have been hot research topics for decades. Stommel (1965) and Stommel and Yoshida (1972) contributed milestone studies for the Gulf Stream and Kuroshio, respectively. Hogg and Johns (1995) summarized the observational work for WBCs up to the mid-1990s. Imawaki et al. (2013) combined recent studies and presented the structure and dynamics of WBCs, as well as their roles in basin-scale circulation, regional variability, and their influence on atmosphere and climate. These studies indicate that WBCs typically have relatively stable main paths, water and heat transport, and high speed ( $\sim 1$  m/s) compared to other surface current systems in the ocean. Therefore, the instabilities of WBCs, such as variation of path and water transport, either can significantly influence the global climate system (e.g. Kwon et al. 2010), local marine ecosystems (e.g. Gawarkiewicz et al. 2012) and

weather systems (e.g. Minobe et al. 2010), or can be indicators of global climate variations (e.g. Wu et al. 2012).

Instabilities of WBC systems usually result in meanders and eddy shedding, and consequently, high eddy kinetic energy (EKE). Figure 1a shows the distribution of climatological means EKE in the North Atlantic, estimated from 21 years of satellite-observed sea level anomaly data. As expected, high EKE occurs near the WBC region with large instabilities (Figure 1b). The greatest EKE in Figure 1a is located in the open ocean region where the Gulf Stream veers away from the coastline to the east. Much studies have been done on the part of Gulf Stream and its interaction with topography and Atlantic Ocean circulation. In this study, I will focus on two of its upstream regions: the Gulf of Mexico and the South Atlantic Bight, where significant EKE are also observed.

## **2. Loop Current in the Gulf of Mexico**

Originating at the Yucatan Channel and exiting through the Florida Straits, the Loop Current (LC) is a dominant circulation feature in the Gulf of Mexico (GoM) (Figure 1b). One of the most notable characteristics of the LC is that it episodically sheds large, high-speed eddies with diameters of about 200-300 km and swirl speed of  $\sim 2$  m/s, which affect almost every aspect of the GoM including ocean circulation, biochemical properties, larval transport, and air-sea interaction (Oey et al. 2005a; Xue et al. 2013; Richards et al. 1993; Small et al. 2008). LC eddy shedding consists of highly nonlinear extension and retraction processes (e.g., Oey et al. 2005a). Sometimes, the LC can shed eddies without extension, and detached eddies can also re-attach. The time interval between eddy shedding events is found to be

irregular, ranging from 0.5 to 18 months (Leben 2005). Between eddy shedding, variations of LC frontal position are also significant. The north and west edges of the LC can vary from about 25.5°N to 27.5°N and 86°W to 90°W, respectively (Leben 2005; Gopalakrishnan et al. 2013).

Daily operations of approximately 4,000 oil and gas drilling platforms in the northern GoM are significantly affected by the LC and its high-speed eddies, which make planning and scheduling a challenge for this expensive enterprise (Leben and Honaker 2006; Sammarco et al. 2004). Accurate prediction of the LC and LC eddies is of critical importance for both scientific research and societal benefit. For example, in order to mitigate the adverse impacts of the *Deepwater Horizon* oil spill in 2010, intensive research on the LC and LC eddies was performed during and after the incident (e.g., Liu et al. 2013). The LC and LC eddies also play an active role in the rapid intensification of GoM hurricanes, such as devastating Hurricanes Katrina and Rita (Leben and Honaker 2006), which caused extensive loss of life and property damage in many Gulf coastal communities.

Much effort has been expended to predict LC variation and its eddy shedding process using remote sensing observations and primitive equation numerical models. Oey et al. (2005b) performed a study to predict the LC and its eddy frontal position using the Princeton Ocean Model (POM). Yin and Oey (2007) applied the bred-ensemble forecast technique to estimate the locations and strengths of the LC and LC eddies from July to September 2005. Counillon and Bertino (2009) presented a small-ensemble forecast using the Hybrid Coordinate Ocean Model to predict LC eddy shedding. A semi-theoretical basis was provided by Lugo-Fernández and Leben (2010) on the linear relationship between LC retreat

latitude and eddy separation period. Forristall et al. (2010) showed that of statistical methods have better skills on LC prediction than that of most dynamical models. Mooers et al. (2012) evaluated several different ocean models' performances at LC eddy shedding prediction using various prediction skill assessment methods in the report of the GoM 3-D Operational Ocean Forecast System Pilot Prediction Project. More recently, with the four-dimensional variation method, Gopalakrishnan et al. (2013) tested the predictability of the LC eddy shedding process using the Massachusetts Institute of Technology general circulation model (MITgcm). Xu et al. (2013) applied the local ensemble transform Kalman filter with the parallel POM to estimate the states of the LC and LC eddies from April to July 2010.

All the above studies are based on either simple empirical relations or primitive equation ocean models focusing on a single LC eddy or a small number of LC eddy shedding events. The lack of generality makes the assessment of their model predictability very difficult (e.g., Mooers et al. 2012). As a powerful tool in many areas, such as pattern recognition, parameter optimization, and time series prediction, the machine learning technique will be used to analyze and predict variations of the LC and LC eddies.

### **3. Gulf Stream in the South Atlantic Bight**

Further downstream, the Gulf Stream (GS) forms and flows through the Strait of Florida, and then moves farther northward along the shelf break of the southeast U.S. continental shelf (also known as the South Atlantic Bight, SAB), before leaving the shelf slope and turning into the deep ocean near Cape Hatteras (Figure 1b). Meanders and fluctuations of the GS path have been observed in this region, especially near the ridge and

trough bottom structure off Charleston, SC, known as the “Charleston Bump” (Bane and Brooks 1979; Figure 2). The offshore deflection of the GS usually propagates downstream of the Bump, which can even affect the position of the GS near Cape Hatteras.

The position of the GS can affect the coastal circulation, along- and cross-shelf water exchange, marine ecosystem, and regional weather system in the SAB. For instance, Miller and Lee (1995) shows as the GS flows along the shelf break of the SAB, the variation of its position can easily change the circulation on the continental shelf. Frontal eddies and water intrusion caused by the instability and variation of the GS play an important role in the water exchange between continental shelf and the open ocean (Lee et al. 1991; Castelao 2011). At the same time, these processes can also transport nutrients to the euphotic zone beneath the GS, which further affects productivity and biomass variation in the SAB (Lee et al. 1991; Signorini and McClain 2007). Because of the influence of hydrodynamics on fisheries, fish population and larval transport in the SAB are closely linked to the position of the GS (Werner et al. 1997; Epifanio and Garvine 2001). Furthermore, GS position can impact the distribution of sea surface temperature, which moderates the ocean-to-atmosphere heat fluxes and results in variation of the local weather system (Bane and Osgood 1989; Li et al. 2002; Joyce et al. 2009; Kwon et al. 2010; Minobe et al. 2010; Nelson et al. 2014).

The existence of GS meanders along the continental margin in the SAB has been recognized for decades. The first detailed observation of GS meanders was reported by Webster (1961) using measurements of surface salinity and velocity and water temperature within 200 m depth. Fuglister and Voorhis (1965) showed that the GS deflection in the SAB is also evident at 200 m depth. Bane and Brooks (1979) described and discussed the wavelike

propagation of the GS deflection from upstream to downstream in the SAB. From observations, Legeckis (1979) concluded that on a seasonal time scale, the time-dependent lateral movements of the GS downstream from the Charleston Bump increase by about a factor of three relative to the upstream movements, and the GS is topographically forced by the depth change near the Bump. Bane et al. (1981) presented a three-dimensional structure of GS meanders and estimated the meander phase propagation speed to be 35 km/day based on observation. Bane (1983) also reported that larger GS deflection in the SAB occurs in wintertime. Olson et al. (1983) concluded through frontal statistics and historical data analysis that the deflection observed at the Charleston Bump is not due to direct topographic effects. Bane and Dewar (1988) reported the bimodality of the GS path in the SAB, while Miller (1994) and Schmeits and Dijkstra (2001) further supported this idea with satellite data and high-resolution ocean general circulation model results, respectively. Through a model study, Xue and Mellor (1993) found a slightly longer wavelength and slower phase speed exists downstream of the Charleston Bump than upstream. Miller and Lee (1995) analyzed the energetics of numerical simulations and concluded that the development of the GS meanders and frontal eddies is controlled by a mixture of both baroclinic and barotropic instabilities of the mean GS flow. Simulations using idealized topography by Xie et al. (2007) showed that the GS meander is the result of the combined effect of isobathic curvature of the SAB bathymetry and the Charleston Bump. Mesoscale eddies in the SAB have an effect on the GS as well, and they are most frequently observed downstream of the Charleston Bump, where the amplitude of most eddies is increased with water depth (Castelao and He 2013). More recently, Gula et al. (2015) quantified the role played by

interactions of the GS with topographic features and the subsequent impact of nonlinear eddy-mean flow interactions through a high-resolution model.

Because of limited observations, the understanding of GS path variability over a longer time scale is very limited. With the continued development of satellite altimetry and new ocean modeling and adjoint sensitivity tools, it is now possible to use two decades' satellite observed sea surface height data and quantitative model simulation results to explore the long-term variation of the GS path and elucidate the mechanisms that determine such variation.

#### **4. Research objectives and dissertation outline**

The overarching objective of this dissertation research is to achieve a deeper understanding of the patterns, mechanisms, and predictability of WBC system variation in the GoM and the SAB using the state-of-art data analysis and numerical model diagnostic methods. Specific objectives are:

- I. Extract the pattern and evolution of LC and LC eddies in the GoM by clustering the corresponding satellite-observed sea level data over two decades (1992-2013). Identify possible environmental factors that affect the state of the LC.
- II. Explore the predictability of LC state using a new machine learning forecasting method and provide a comprehensive assessment on the prediction skills of this method.
- III. Quantify and classify variations of GS position in the SAB over a 21-year period (1993-2013) using satellite-observed sea surface height data.

IV. Identify dynamical mechanisms that cause variation of GS position using realistic ocean hindcast and adjoint models.

The outline of this dissertation is as follows: Chapter II focuses on the clustering of the LC patterns based on the satellite altimeter data. Different patterns of the LC are extracted from long-term satellite observation. The influence of wind stress and climate variation on the LC temporal variation is explored. Based on the analysis in Chapter II, a forecasting system is developed to predict the state of the LC and LC eddies in Chapter III. Validations against independent satellite observations are also provided. Chapter V focuses on the GS in the SAB. First, the long-term GS position variability is quantified using two decades' satellite altimeter data. Factors that may affect the GS position in the SAB are analyzed from statistical point of view. Then, a realistic ocean circulation model is developed to simulate the GS offshore meanders in November 2009. This meander kept evolving in the next 4-5 months, constituting the largest offshore meander event over last two decades. Triggering mechanisms of this meander in November are studied using the adjoint sensitivity and vorticity budget analysis methods. Finally, a summary of this dissertation is presented in Chapter IV.

The dissertation consists of three peer-reviewed publications: Zeng et al. (2015a) for Chapter II; Zeng et al. (2015b) for Chapter III, and Zeng and He (submitted) for Chapter V. Another publication (Zeng et al., 2015c) that is marginally related to the dissertation topic is not included in this dissertation.

## References

- Bane, J. M. (1983), Initial observations of the subsurface structure and short-term variability of the seaward deflection of the Gulf Stream off Charleston, South Carolina, *J. Geophys. Res.*, 88(C8), 4673–4684, doi:10.1029/JC088iC08p04673.
- Bane, J. M., and D. A. Brooks (1979), Gulf Stream meanders along the Continental Margin from the Florida Straits to Cape Hatteras, *Geophys. Res. Lett.*, 6(4), 280–282, doi:10.1029/GL006i004p00280.
- Bane, J. M., and W. K. Dewar (1988), Gulf Stream bimodality and variability downstream of the Charleston bump, *J. Geophys. Res.*, 93(C6), 6695–6710, doi:10.1029/JC093iC06p06695.
- Bane, J. M., and K. E. Osgood (1989), Wintertime air-sea interaction processes across the Gulf Stream, *J. Geophys. Res.*, 94(C8), 10755–10772, doi:10.1029/JC094iC08p10755.
- Bane, J. M., D. A. Brooks, and K. R. Lorenson (1981), Synoptic observations of the three-dimensional structure and propagation of Gulf Stream meanders along the Carolina continental margin, *J. Geophys. Res.*, 86(C7), 6411–6425, doi:10.1029/JC086iC07p06411.
- Castelao, R. (2011), Intrusions of Gulf Stream waters onto the South Atlantic Bight shelf, *J. Geophys. Res.*, 116(C10), C10011, doi:10.1029/2011JC007178.
- Castelao, R. M., and R. He (2013), Mesoscale eddies in the South Atlantic Bight, *J. Geophys. Res. Oceans*, 118(10), 5720–5731, doi:10.1002/jgrc.20415.
- Counillon, F., and L. Bertino (2009), High-resolution ensemble forecasting for the Gulf of Mexico eddies and fronts, *Ocean Dynamics*, 59, 83–95, doi:10.1007/s10236-008-0167-0.
- Cushman-Roisin, B., and J.-M. Beckers (2011), *Introduction to Geophysical Fluid Dynamics: Physical and Numerical Aspects*, Academic Press.
- Epifanio, C. E., and R. W. Garvine (2001), Larval Transport on the Atlantic Continental Shelf of North America: a Review, *Estuarine, Coastal and Shelf Science*, 52(1), 51–77, doi:10.1006/ecss.2000.0727.

- Forristall, G. Z., R. R. Leben, and C. A. Hall (2010), A Statistical Hindcast and Forecast Model for the Loop Current, *Offshore Technology Conference*, doi:doi:10.4043/20602-MS.
- Fuglister, F. C., and A. D. Voorhis (1965), A New Method of Tracking the Gulf Stream, *Limnol. Oceanogr.*, 10(suppl), R115–R124, doi:10.4319/lo.1965.10.suppl2.r115.
- Gawarkiewicz, G. G., R. E. Todd, A. J. Plueddemann, M. Andres, and J. P. Manning (2012), Direct interaction between the Gulf Stream and the shelfbreak south of New England, *Sci. Rep.*, 2, doi:10.1038/srep00553.
- Gopalakrishnan, G., B. D. Cornuelle, and I. Hoteit (2013), Adjoint sensitivity studies of loop current and eddy shedding in the Gulf of Mexico, *Journal of Geophysical Research: Oceans*, n/a–n/a, doi:10.1002/jgrc.20240.
- Gula, J., M. J. Molemaker, and J. C. McWilliams (2014), Gulf Stream dynamics along the Southeastern U.S. Seaboard, *J. Phys. Oceanogr.*, doi:10.1175/JPO-D-14-0154.1.
- Hogg, N. G., and W. E. Johns (1995), Western boundary currents, *Rev. Geophys.*, 33(S2), 1311–1334, doi:10.1029/95RG00491.
- Hsieh, W. W. (2001), Nonlinear principal component analysis by neural networks, *Tellus A*, 53(5), 599–615, doi:10.1034/j.1600-0870.2001.00251.x.
- Imawaki, S., A. S. Bower, L. Beal, and B. Qiu (2013), Western Boundary Currents, in *Ocean Circulation and Climate - A 21st Century Perspective, 2nd Edition*, pp. 305–338, Academic Press.
- Ishikawa, Y., T. Awaji, N. Komori, and T. Toyoda (2004), Application of Sensitivity Analysis Using an Adjoint Model for Short-Range Forecasts of the Kuroshio Path South of Japan, *Journal of Oceanography*, 60(2), 293–301, doi:10.1023/B:JOCE.0000038335.50080.ff.
- Joyce, T. M., Y.-O. Kwon, and L. Yu (2009), On the Relationship between Synoptic Wintertime Atmospheric Variability and Path Shifts in the Gulf Stream and the Kuroshio Extension, *J. Climate*, 22(12), 3177–3192, doi:10.1175/2008JCLI2690.1.
- Kwon, Y.-O., M. A. Alexander, N. A. Bond, C. Frankignoul, H. Nakamura, B. Qiu, and L. A. Thompson (2010), Role of the Gulf Stream and Kuroshio–Oyashio Systems in Large-

Scale Atmosphere–Ocean Interaction: A Review, *J. Climate*, 23(12), 3249–3281, doi:10.1175/2010JCLI3343.1.

Leben, R. R. (2005), Altimeter-Derived Loop Current Metrics, in *Circulation in the Gulf of Mexico: Observations and Models*, edited by W. Sturges and A. Lugo-Fernandez, pp. 181–201, American Geophysical Union.

Leben, R. R., and D. J. Honaker (2006), What Do We Know and What Can We Predict About the Timing of Loop Current Eddy Separation?, in *ESA Special Publication*, vol. 614, p. 19.

Lee, S.-K. (2001), On the structure of supercritical western boundary currents, *Dynamics of Atmospheres and Oceans*, 33(4), 303–319, doi:10.1016/S0377-0265(01)00056-2.

Lee, T. N., J. A. Yoder, and L. P. Atkinson (1991), Gulf Stream frontal eddy influence on productivity of the southeast U.S. continental shelf, *J. Geophys. Res.*, 96(C12), 22191–22205, doi:10.1029/91JC02450.

Legeckis, R. V. (1979), Satellite Observations of the Influence of Bottom Topography on the Seaward Deflection of the Gulf Stream off Charleston, South Carolina, *J. Phys. Oceanogr.*, 9(3), 483–497, doi:10.1175/1520-0485(1979)009<0483:SOOTIO>2.0.CO;2.

Liu, Y., A. MacFadyen, Z.-G. Ji, and R. H. Weisberg (2013), *Monitoring and Modeling the Deepwater Horizon Oil Spill: A Record Breaking Enterprise*, John Wiley & Sons.

Li, Y., H. Xue, and J. M. Bane (2002), Air-sea interactions during the passage of a winter storm over the Gulf Stream: A three-dimensional coupled atmosphere-ocean model study, *J. Geophys. Res.*, 107(C11), 3200, doi:10.1029/2001JC001161.

Lugo-Fernández, A., and R. R. Leben (2010), On the Linear Relationship between Loop Current Retreat Latitude and Eddy Separation Period, *Journal of Physical Oceanography*, 40(12), 2778–2784, doi:10.1175/2010JPO4354.1.

Miller, J. L. (1994), Fluctuations of Gulf Stream frontal position between Cape Hatteras and the Straits of Florida, *J. Geophys. Res.*, 99(C3), 5057–5064, doi:10.1029/93JC03484.

Miller, J. L., and T. N. Lee (1995), Gulf Stream meanders in the South Atlantic Bight: 1. Scaling and energetics, *J. Geophys. Res.*, 100(C4), 6687–6704, doi:10.1029/94JC02542.

- Minobe, S., M. Miyashita, A. Kuwano-Yoshida, H. Tokinaga, and S.-P. Xie (2010), Atmospheric Response to the Gulf Stream: Seasonal Variations, *Journal of Climate*, 23(13), 3699–3719, doi:10.1175/2010JCLI3359.1.
- Mooers, C. N. K., E. D. Zaron, and M. K. Howard (2012), Final Report for Phase I: Gulf of Mexico 3-D Operational Ocean Forecast System Pilot Prediction Project (GOMEX-PPP),.
- Nelson, J., R. He, J. C. Warner, and J. Bane (2014), Air–sea interactions during strong winter extratropical storms, *Ocean Dynamics*, 64(9), 1233–1246, doi:10.1007/s10236-014-0745-2.
- Oey, L.-Y., T. Ezer, G. Forristall, C. Cooper, S. DiMarco, and S. Fan (2005a), An exercise in forecasting loop current and eddy frontal positions in the Gulf of Mexico, *Geophysical Research Letters*, 32(12), n/a–n/a, doi:10.1029/2005GL023253.
- Oey, L.-Y., T. Ezer, and H.-C. Lee (2005b), Loop Current, Rings and Related Circulation in the Gulf of Mexico: A Review of Numerical Models and Future Challenges, in *Circulation in the Gulf of Mexico: Observations and Models*, edited by W. Sturges and A. Lugo-Fernandez, pp. 31–56, American Geophysical Union.
- Olson, D. B., O. B. Brown, and S. R. Emmerson (1983), Gulf Stream frontal statistics from Florida Straits to Cape Hatteras derived from satellite and historical data, *J. Geophys. Res.*, 88(C8), 4569–4577, doi:10.1029/JC088iC08p04569.
- Richards, W. J., M. F. McGowan, T. Leming, J. T. Lamkin, and S. Kelley (1993), Larval Fish Assemblages at the Loop Current Boundary in the Gulf of Mexico, *Bulletin of Marine Science*, 53(2), 475–537.
- Schmeits, M. J., and H. A. Dijkstra (2001), Bimodal Behavior of the Kuroshio and the Gulf Stream, *J. Phys. Oceanogr.*, 31(12), 3435–3456, doi:10.1175/1520-0485(2001)031<3435:BBOTKA>2.0.CO;2.
- Signorini, S. R., and C. R. McClain (2007), Large-scale forcing impact on biomass variability in the South Atlantic Bight, *Geophys. Res. Lett.*, 34(21), L21605, doi:10.1029/2007GL031121.
- Small, R. J., S. P. deSzoeko, S. P. Xie, L. O’Neill, H. Seo, Q. Song, P. Cornillon, M. Spall, and S. Minobe (2008), Air–sea interaction over ocean fronts and eddies, *Dynamics of Atmospheres and Oceans*, 45(3–4), 274–319, doi:10.1016/j.dynatmoce.2008.01.001.

- Stommel, H. (1948), The westward intensification of wind-driven ocean currents, *Eos Trans. AGU*, 29(2), 202–206, doi:10.1029/TR029i002p00202.
- Stommel, H. M. (1958), *The Gulf Stream : a physical and dynamical description*, Berkeley : University of California Press.
- Stommel, H. M. (1972), *Kuroshio: its physical aspects*, University of Tokyo Press.
- Webster, F. (1961), A description of gulf stream meanders off Onslow Bay, *Deep Sea Research (1953)*, 8(2), 130–143, doi:10.1016/0146-6313(61)90005-3.
- Werner, F. E., J. A. Quinlan, B. O. Blanton, and R. A. Luetlich Jr. (1997), The role of hydrodynamics in explaining variability in fish populations, *Journal of Sea Research*, 37(3–4), 195–212, doi:10.1016/S1385-1101(97)00024-5.
- Wu, L. et al. (2012), Enhanced warming over the global subtropical western boundary currents, *Nature Clim. Change*, 2(3), 161–166, doi:10.1038/nclimate1353.
- Xie, L., X. Liu, and L. J. Pietrafesa (2007), Effect of Bathymetric Curvature on Gulf Stream Instability in the Vicinity of the Charleston Bump, *J. Phys. Oceanogr.*, 37(3), 452–475, doi:10.1175/JPO2995.1.
- Xue, H., and G. Mellor (1993), Instability of the Gulf Stream Front in the South Atlantic Bight, *J. Phys. Oceanogr.*, 23(11), 2326–2350, doi:10.1175/1520-0485(1993)023<2326:IOTGSF>2.0.CO;2.
- Xue, Z., R. He, K. Fennel, W.-J. Cai, S. Lohrenz, and C. Hopkinson (2013), Modeling ocean circulation and biogeochemical variability in the Gulf of Mexico, *Biogeosciences*, 10(11), 7219–7234, doi:10.5194/bg-10-7219-2013.
- Xu, F.-H., L.-Y. Oey, Y. Miyazawa, and P. Hamilton (2013), Hindcasts and forecasts of Loop Current and eddies in the Gulf of Mexico using local ensemble transform Kalman filter and optimum-interpolation assimilation schemes, *Ocean Modelling*, 69, 22–38, doi:10.1016/j.ocemod.2013.05.002.
- Yin, X.-Q., and L.-Y. Oey (2007), Bred-ensemble ocean forecast of loop current and rings, *Ocean Modelling*, 17(4), 300–326, doi:10.1016/j.ocemod.2007.02.005.

- Zeng, X., Y. Li, R. He, and Y. Yin (2015a) Clustering of the Loop Current patterns based on satellite observed sea surface height and self-organizing map, *Remote Sensing Letters*, 6:1, 11-19, doi: 10.1080/2150704X.2014.998347.
- Zeng, X., Y. Li, and R. He (2015b), Predictability of the Loop Current variation and eddy shedding process in the Gulf of Mexico using an artificial neural network approach, *Journal Atmospheric and Oceanic Technology*, doi: 10.1175/JTECH-D-14-00176.1.
- Zeng, X., R. He, Z. Xue, H. Wang, Y. Wang, Z. Yao, W. Guan, and J. Warrillow (2015c), River-derived sediment suspension and transport in the Bohai, Yellow, and East China Seas: A preliminary modeling study, *Continental Shelf Research special issue: Coastal Seas in a Changing World: Anthropogenic Impact and Environmental Responses*, 111B:112-125, doi: 10.1016/j.csr.2015.08.015.
- Zeng, X. and R. He (to be submitted), Triggering mechanisms of large Gulf Stream meanders in the South Atlantic Bight. *Journal of Geophysical Research: Oceans*.

## Figures

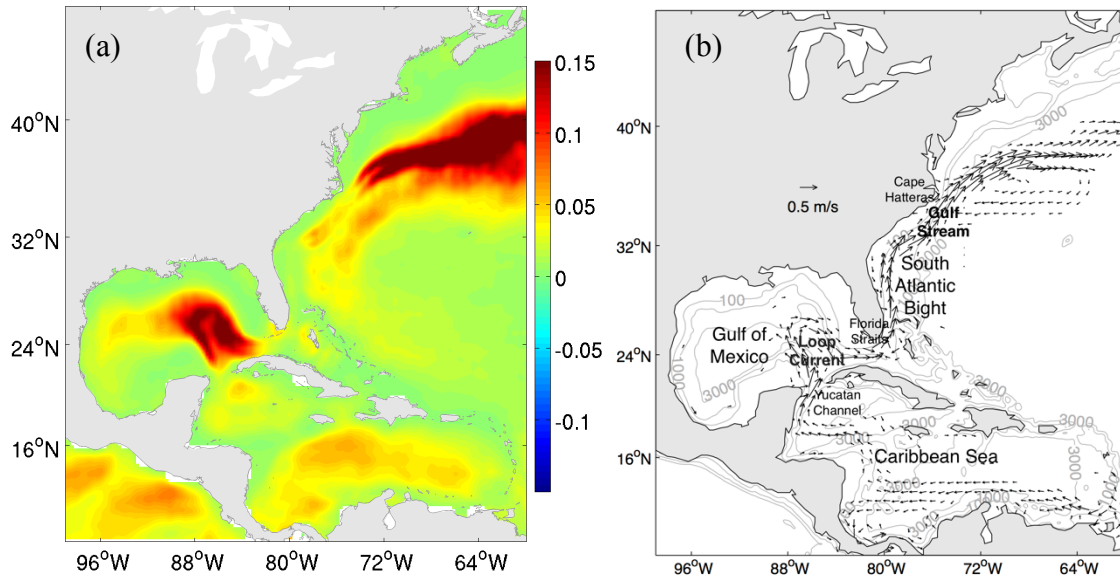


Figure 1. (a) Eddy kinetic energy (m<sup>2</sup>/s<sup>2</sup>) derived from 21 years' mean AVISO sea level anomaly satellite data. (b) Study domain. Black arrows are geostrophic currents (> 0.1 m/s) derived from 21 years' mean AVISO sea surface height data. They can be considered to be part of the Western Boundary Current system in the North Atlantic. Contours are isobaths at 100, 1000, and 3000 m.

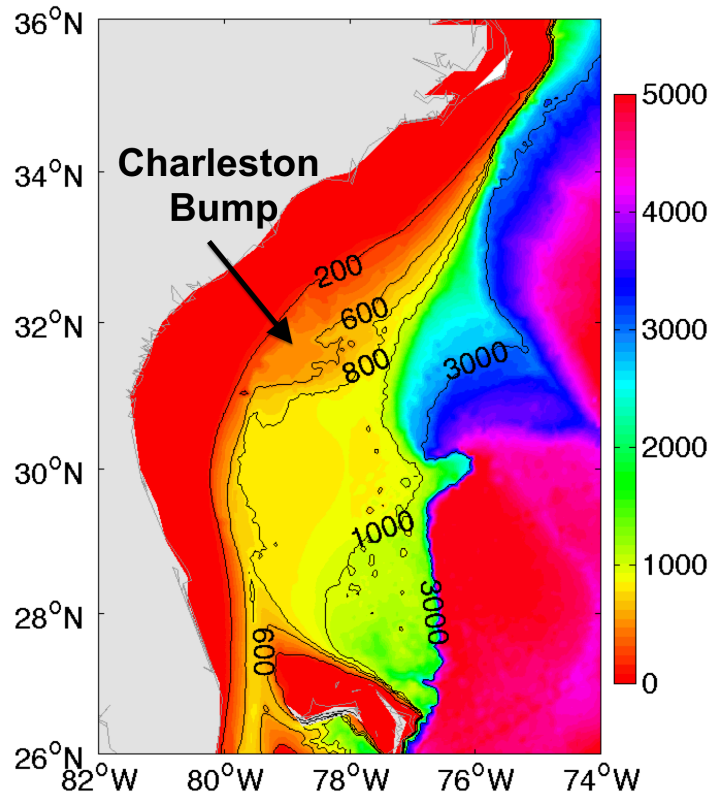


Figure 2. Topography of the South Atlantic Bight. Water depth is shown in meters. Contours are 200, 600, 700, 1000, and 3000 m isobaths. The Charleston Bump is shown by the arrow.

**Chapter II: Clustering of Loop Current patterns based on the satellite-  
observed sea surface height and self-organizing map**

Xiangming Zeng<sup>1</sup>, Yizhen Li<sup>1</sup>, Ruoying He<sup>1</sup>, and Yuqi Yin<sup>2</sup>

<sup>1</sup>Department of Marine, Earth, and Atmospheric Sciences, North Carolina State University,  
Raleigh, NC, USA

<sup>2</sup> Institute of Oceanology, Chinese Academy of Sciences, Qingdao, China

*(Published in Remote Sensing Letters, DOI: 10.1080/2150704X.2014.998347)*

## **Abstract**

The self-organizing map is used to investigate variations of the Loop Current (LC) in the Gulf of Mexico from 1992 to 2013 based on satellite-observed sea surface height data. It is found that LC variations can be characterized by three spatial patterns: normal, extension, and retraction. The corresponding temporal variations confirm that LC eddy shedding generally occurs during the transition from the extension to retraction patterns. On the weekly time scale, the wind stress curl (WSC) in the Caribbean Sea has a major influence on LC eddy shedding. The increase of Caribbean WSC from June to November favours more frequent LC eddy shedding during that period. On the interannual time scale, there is also a potential linkage between the frequency of LC eddy shedding and El Niño activities.

## **1. Introduction**

The Loop Current (LC) is the dominant ocean circulation system in the Gulf of Mexico (GoM) (e.g., Oey et al., 2005). It originates at the Yucatan Channel and exits through the Florida Straits (Figure 1). One of its most notable characteristics is that it episodically sheds large, warm-core eddies which affect various aspect of GoM hydrodynamics. LC eddy shedding consists of highly nonlinear extension and retraction processes (e.g., Oey et al., 2005). Sometimes, the LC can shed eddies without extension, and detached eddies can also re-attach to the LC. The time interval between eddy shedding events is found to be irregular, ranging from 0.5 to 18 months (Leben et al., 2005).

The causes of the complex LC shedding process are still subject to debate. Hurbult and Thompson (1980) pointed out that LC eddy shedding was controlled by the horizontal instability of the LC. Maul and Vukovich (1993) found that the ensemble correlation between monthly position of the LC and volume transport is zero based on twelve years satellite and in situ data. Pichevin and Nof (1997) concluded that eddy shedding is required to satisfy the momentum balance principle. Oey et al. (2003) suggested that Caribbean Sea (CS) eddies spun up by local winds could propagate through the Yucatan Channel into the GoM and influence the LC eddy shedding process. Lugo-Fernández, (2007) examined the LC through a dynamical system approach and found that the LC is nonlinear, but not chaotic. Nürnberg et al. (2008) explored the variability of the LC and its relation with Mississippi River discharge through a geochemistry view. Lugo-Fernandez and Leben (2010) provided the linear relationship between LC retreat latitude and eddy separation period using the satellite altimeter-derived LC metrics. Sturge et al. (2010) further proposed that the downstream Florida Strait transport variation may trigger LC eddy shedding, while Oey and Chang (2011) argued that several model solutions showed that such a downstream trigger was not necessary. Numerous other numerical modelling efforts (e.g., Lee and Mellor, 2003; Yin and Oey, 2007; Chang and Oey, 2012; Le Henaff et al., 2012; Chang and Oey 2013a; Xu et al., 2013) were also made to depict the evolution of the LC. A recent study by Liu et al. (2012) suggested that the local net heat flux and the intensity of the advective heat flux convergence can introduce instability of the LC and associated eddies, highlighting that the complex coupling between atmosphere and ocean can contribute to the LC shedding (e.g., Chang and Oey, 2013b).

In this study, we used a novel feature extraction method to characterize satellite observed sea surface height data of the LC and further analyse its variations. The frequency of occurrence for the LC retraction pattern was then correlated with wind stress curls and several climate indices at different time scales.

## **2. Data and methods**

Twenty one years (1992-2013) of gridded satellite altimeter-observed sea surface height (SSH) data around the LC area (red box in Figure 1) were analysed. Altimeter data, distributed by the Archiving, Validation and Interpretation of Satellite Oceanographic (AVISO) data service, have spatial and temporal resolutions of  $1/3^\circ$  and 7 days, respectively. For quality control, only the data located inside the areas with water depth greater than 100 m were chosen (Liu et al., 2008; Yin et al., 2014). In addition, wind data (with 3 hourly time interval and  $\sim 33$  km spatial resolution) were extracted from National Centers for Environmental Prediction North American Regional Analysis (NARR). Weekly mean wind stress was subsequently calculated based on Cushman-Roisin and Beckers's (2011) method, and then used to derive corresponding wind stress curls. Climate indices were obtained from the Physical Sciences Division of Earth System Research Laboratory, National Oceanic and Atmospheric Administration (NOAA).

Our focus here is to apply an advanced method, the self-organizing map (SOM), to re-examine the long-term satellite observations archived for the LC region in the last two decades. Actually, satellite data have been widely used in studying the Gulf circulation and LC dynamics (e.g., Leben, 2005; Leben and Honaker, 2006; Lugo-Fernandez and Leben,

2010). Based on an unsupervised artificial neural network, the SOM is an effective method for feature extraction and classification, and can map high-dimensional input data onto the elements of a regular, low-dimensional array (Kohonen, 2001). It has been demonstrated to be more powerful than the conventional empirical orthogonal function (EOF) method for feature extractions, especially when the signal is highly nonlinear (Reusch et al., 2005; Liu et al., 2006b). The SOM has been shown to be a valuable tool in oceanographic studies (Liu and Weisberg, 2011). It has been applied to identify patterns in ocean currents and sea surface temperature fields on the West Florida Shelf (Liu and Weisberg, 2005; Liu et al., 2006a; Liu et al., 2007), biogeochemical properties in the northern Adriatic Sea (Solidoro et al., 2007), and current variability in the China Seas (Liu et al., 2008; Jin et al., 2010; Tsui and Wu, 2012; Yin et al., 2014).

In this study, all weekly SSH data within the study domain were fed into the SOM as inputs. Based on the minimum Euclidean distance and pattern size given initially, different SSH patterns were extracted in a topology preserving way—each weekly SSH snapshot was then assigned to one of these patterns (e.g., Liu and Weisberg, 2005). From these assignments, the best matching unit (BMU) time series and frequency of occurrence (FO) of each pattern were obtained. The SOM parameters such as lattice, weights, training method, and neighbourhood function were chosen according to Liu et al. (2006b). Based on our sensitivity experiments and the variability of the LC, the pattern number  $1 \times 3$  with contrasting difference between each pattern was chosen prior to the training process.

### **3. Results**

### 3.1 Spatial variability

The three SOM patterns and their corresponding FOs are shown in Figure 2. The 0.45 m SSH contour line was chosen as the edge of the LC and its detached eddies in this study based on the examination of patterns and evolutions of LC and LC eddies over 21 years SSH data record. It is consistent with methods used by earlier studies (e.g., Leben, 2005) in SSH contour selection. Pattern 1 (P1) is the LC's normal condition, without extension or shedding. The north and west edges of LC in P1 reach about 26.5°N and 88°W, respectively. For P1, the LC is featured with significantly high sea level, accompanied by low sea level on the northwest edge. Pattern 2 (P2) is the LC extension pattern. The most obvious feature for P2 is that the LC extends into a relatively elongated shape, such that its north and west edges reach about 27.5°N and 90°W. In contrast, Pattern 3 (P3) represents the LC retraction pattern, which can also be considered as the eddy shed pattern. The main body of the LC and LC eddy are clearly separated from each other. After eddy shedding, the north and west edges of the LC retreat to about 25.5°N and 86°W. The shed eddy is located at about 26°N, 90°W with lower SSH and weaker geostrophic velocity than the main LC. Different from P1 and P2, P3 shows the LC further to the southeast after eddy shedding. There is also a large cyclonic eddy with low SSH present between the LC and its shed eddy.

### 3.2 Temporal evolution

Figure 2b shows the temporal changes (BMU time series) of the three LC patterns (P1, P2, and P3). A repeated cycle is generally evident in the 21-years' time series. Using P1 as an arbitrary beginning, the cycle of P1→P2→P3→P1 is fairly robust. Specifically, the LC starts in its normal pattern (P1), and then extends to the northwest to 27.5°N to reach its

extension pattern (P2). An eddy shedding event subsequently occurs, and then the LC retreats to about  $25.5^{\circ}\text{N}$  to its retraction pattern (P3). Due to the nonlinearity of LC evolution, however, not every eddy shedding process follows this cycle (e.g., Lugo-Fernández, 2007).

In order to quantify the percentage occurrence of each pattern, the FO was calculated by summing the number of occurrences of that pattern divided by the total record length (Figure 2a). Over the 21-year study period, 41.5% of the LC patterns belong to the normal pattern (P1), while the extension (P2) and retraction (P3) patterns account for 28.5% and 30.0%, respectively.

To better illustrate the seasonal variation of the LC and the dominant pattern for each month, the monthly FOs (MFO) of the three patterns were also calculated (Figure 2c). The MFO of P1 is larger than those of P2 and P3 from January to May, which suggests that generally the LC tends to remain in its normal pattern (P1) during this period. In July and August, the MFO of P2 is the largest, suggesting that LC tends to extend during this period. The MFO of P3 becomes dominant from September to December, showing that retraction of the LC is more likely to occur during this period. We note that transitions from P1 to P2 and from P2 to P3 occur in June and the end of August, respectively, indicating that statistically the LC extension (eddy shedding) tends to occur in June (in late August).

#### **4. Discussion**

To further study the LC eddy shedding process and its possible mechanisms, we compared the weekly and annual FOs of P3 with long-term mean winds stress curl (WSC) over different spatial domains, as well as with different climate indices.

Figure 3a shows the weekly FO (WFO) of P3 along with long-term weekly mean WSC of three (Caribbean Sea (CS), Bahamas, and GoM; see Figure 1) previously identified wind influence regimes (e.g., Oey et al., 2003; Sturges et al., 2010; Gopalakrishnan et al., 2013). We found that the zero time-lag correlation coefficient between CS WSCs and WFO of P3 is 0.83, much higher than the correlations with the local WSC in the GoM (correlation coefficient  $r=0.45$ ) and the downstream WSC in the Bahamas area ( $r=0.65$ ). This suggests that LC eddy shedding is likely associated more with CS WSC in the upstream Caribbean Sea. Indeed, Oey et al. (2003) showed that negative CS WSC can spin up Caribbean eddies (anticyclones), which in turn lead to a lower frequency of LC shedding. Our results further reveal the CS WSC increases from June to November. It can play a role in suppressing the formation of anti-cyclonic eddies in the CS. In other words, the increase of CS WSC during this period favours a higher frequency of LC shedding, as shown in Figure 3a.

To understand the interannual variability of LC eddy shedding, the annual FO (AFO) of P3 was examined together with various climate indices, including the Oceanic Niño Index (ONI), North Atlantic Oscillation index (NAO), Southern Oscillation Index (SOI), and Pacific Decadal Oscillation (PDO). Various time lag correlations and running averages were performed. Among them, the best correlation ( $r=0.6$  at 95% confidence interval) is found between the six-month moving-averaged ONI and the AFO of P3 with a 90-day lag (Figure 3b). Other indices show no significant correlations (not shown). The ONI is defined as the sea surface temperature anomalies in Niño Region 3.4 ( $5^{\circ}\text{N}$ - $5^{\circ}\text{S}$ ,  $120^{\circ}\text{W}$ - $170^{\circ}\text{W}$ ) and used as an index for El Niño (e.g., Koushy and Higgins, 2007). The relationship between ONI and

AFO of P3 suggests a possible connection between Pacific climate and the LC eddy shedding process.

Previous studies on the tele-connection between the Atlantic and the Pacific showed that El Niño, a Pacific event, can have a strong impact on wind and circulation in the Atlantic (Enfield and Mayer, 1997; Alexander and Scott, 2002; Kennedy et al., 2007; Smith et al., 2007). The frequent swing in the trade winds and resulting wind stress curls in the Atlantic may favour more eddy shedding in the GoM (Chang and Oey, 2013b). Detailed processes determining how the basin-scale teleconnection influences LC eddy shedding clearly need further study that combines observations and numerical model sensitivity experiments.

## **5. Summary**

Three patterns and corresponding temporal evolution of LC SSH were extracted from 21 years of weekly satellite SSH data using the SOM method. In most cases, the LC evolution follows a normal-extension-retraction cycle. Transitions from normal pattern (P1) to extension pattern (P2) and from extension pattern (P2) to retraction pattern (P3) occur in June and the end of August, respectively.

The weekly FO analysis of the LC retraction pattern (P3) indicates CS wind stress curl has a major influence on LC eddy shedding. The increase of CS WSC from June to November favours the LC eddy shedding at higher frequency during that period. On the interannual time scale, the significant relationship between ONI and AFO of P3 suggests a possible connection between Pacific climate and LC eddy shedding frequency, which needs further study. Due to the fully three-dimensional nature of the loop current and its high

nonlinearity (e.g., Lugo-Fernández, 2007), realistic dynamical modelling study is needed to better understand causes of LC shedding, vertical structure of circulation, as well as their responses to various forcing agents and climate signals.

### **Acknowledgement**

Research support provided by Gulf of Mexico Research Initiative/GISR through grant 02-S130202, NOAA grant NA11NOS0120033, NASA grants NNX12AP84G and NNX13AD80G is much appreciated. The authors would like to acknowledge the Helsinki University of Technology, Finland for providing the SOM Toolbox and Dr. Y. Liu of University of South Florida for useful guidance on the SOM application in oceanography. Constructive comments provided by from two anonymous reviewers and J. Warrillow's editorial assistance are also appreciated

## References

- Alexander, M., and J. Scott. 2002. "The Influence of ENSO on Air-sea Interaction in the Atlantic." *Geophysical Research Letters* 29 (14): 46. doi:10.1029/2001GL014347.
- Chang, Y.-L., and L.-Y. Oey. 2012. "Why Does the Loop Current Tend to Shed More Eddies in Summer and Winter?" *Geophysical Research Letters* 39 (5): L05605. doi:10.1029/2011GL050773.
- Chang, Y.-L., and L.-Y. Oey. 2013a. "Loop Current Growth and Eddy Shedding Using Models and Observations: Numerical Process Experiments and Satellite Altimetry Data." *Journal of Physical Oceanography* 43 (3): 669–689. doi:10.1175/JPO-D-12-0139.1.
- Chang, Y.-L., and L.-Y. Oey. 2013b. "Coupled Response of the Trade Wind, SST Gradient, and SST in the Caribbean Sea, and the Potential Impact on Loop Current's Interannual Variability." *Journal of Physical Oceanography* 43 (7): 1325–1344. doi:10.1175/JPO-D-12-0183.1.
- Cushman-Roisin, B., and J.-M. Beckers. 2011. *Introduction to Geophysical Fluid Dynamics: Physical and Numerical Aspects*. Academic Press.
- Enfield, D. B., and D. A. Mayer. 1997. "Tropical Atlantic Sea Surface Temperature Variability and Its Relation to El Niño-Southern Oscillation." *Journal of Geophysical Research: Oceans* 102 (C1): 929–945. doi:10.1029/96JC03296.
- Gill, A.E., 1980. Some simple solutions for heat-induced tropical circulation, *Quat.J. Roy. Metero.Soc.*, 106, 447-462.
- Gopalakrishnan, G., B. D. Cornuelle, and I. Hoteit. 2013. "Adjoint Sensitivity Studies of Loop Current and Eddy Shedding in the Gulf of Mexico." *Journal of Geophysical Research: Oceans*: 1–21. doi:10.1002/jgrc.20240.
- Hurlburt, H. E., and J. D. Thompson. 1980. "A Numerical Study of Loop Current Intrusions and Eddy Shedding." *Journal of Physical Oceanography* 10 (10): 1611–1651. doi:10.1175/1520-0485(1980)010<1611:ANSOLC>2.0.CO;2.
- Jin, B., G. Wang, Y. Liu, and R. Zhang. 2010. "Interaction Between the East China Sea Kuroshio and the Ryukyu Current as Revealed by the Self-organizing Map." *Journal of Geophysical Research: Oceans* 115, C12047. doi:10.1029/2010JC006437.

- Kennedy, A. J., M. L. Griffin, S. L. Morey, S. R. Smith, and J. J. O'Brien. 2007. "Effects of El Niño–Southern Oscillation on Sea Level Anomalies Along the Gulf of Mexico Coast." *Journal of Geophysical Research: Oceans* 112 (C5): C05047. doi:10.1029/2006JC003904.
- Kohonen, T. 2001. *Self-Organizing Maps*. Springer.
- Kousky, V. E., and R. W. Higgins, 2007. "An Alert Classification System for Monitoring and Assessing the ENSO Cycle". *Weather and Forecasting*, 22, 353–371. doi: <http://dx.doi.org/10.1175/WAF987.1>
- Leben, R. R. 2005. "Altimeter-Derived Loop Current Metrics." In *Circulation in the Gulf of Mexico: Observations and Models*, ed. Wilton Sturges and Alexis Lugo-Fernandez, 181–201. American Geophysical Union.
- Leben, R. R., and D. J. Honaker. 2006. "What Do We Know and What Can We Predict About the Timing of Loop Current Eddy Separation?" In *ESA Special Publication*, 614:19. <http://adsabs.harvard.edu/abs/2006ESASP.614E..19L>.
- Lee, H.-C., and G. L. Mellor. 2003. "Numerical Simulation of the Gulf Stream System: The Loop Current and the Deep Circulation." *Journal of Geophysical Research: Oceans* 108 (C2): 25. doi:10.1029/2001JC001074.
- Le Hénaff, M., V. H. Kourafalou, Y. Morel, and A. Srinivasan. 2012. "Simulating the Dynamics and Intensification of Cyclonic Loop Current Frontal Eddies in the Gulf of Mexico." *Journal of Geophysical Research: Oceans* 117 (C2): C02034. doi:10.1029/2011JC007279.
- Liu, Y., and R. H. Weisberg. 2005. "Patterns of Ocean Current Variability on the West Florida Shelf Using the Self-organizing Map." *Journal of Geophysical Research: Oceans* 110 (C6): C06003. doi:10.1029/2004JC002786.
- Liu, Y., R.H. Weisberg, and R. He. 2006a. "Sea surface temperature patterns on the West Florida Shelf using Growing Hierarchical Self-Organizing Maps." *Journal of Atmospheric and Oceanic Technology*, 23(2): 325-338.
- Liu, Y., R. H. Weisberg, and C. N. K. Mooers. 2006b. "Performance Evaluation of the Self-organizing Map for Feature Extraction." *Journal of Geophysical Research: Oceans* 111 (C5): C05018. doi:10.1029/2005JC003117.

- Liu, Y., R.H. Weisberg, and L.K. Shay, 2007. "Current patterns on the West Florida Shelf from joint Self-Organizing Map analyses of HF radar and ADCP data." *Journal of Atmospheric and Oceanic Technology*, 24(4), 702-712.
- Liu, Y., R.H. Weisberg, and Y. Yuan, 2008. "Patterns of upper layer circulation variability in the South China Sea from satellite altimetry using the Self-Organizing Map." *Acta Oceanologica Sinica*, 27(Supp.), 129-144.
- Liu, Y., and R.H. Weisberg. 2011. "A Review of Self-Organizing Map Applications in Meteorology and Oceanography." In *Self Organizing Maps - Applications and Novel Algorithm Design*, ed. Josphat Igadwa Mwasiagi. InTech.
- Liu, Y., S. K. Lee, B. A. Muhling, J. T. Lamkin, and D. B. Enfield, 2012. Significant reduction of the Loop Current in the 21st century and its impact on the Gulf of Mexico. *Journal of Geophysical Research: Oceans* 117(C5). doi:10.1029/2011JC007555.
- Lugo-Fernández, A., 2007. "Is the Loop Current a Chaotic Oscillator?" *Journal of physical Oceanography* 37(6): 1455–69. doi:10.1175/JPO3066.1.
- Lugo-Fernández, A., and R. R. Leben. 2010. "On the Linear Relationship Between Loop Current Retreat Latitude and Eddy Separation Period." *Journal of Physical Oceanography* 40 (12): 2778–2784. doi:10.1175/2010JPO4354.1.
- Magaña, V., J. A. Amador, and S. Medina. 1999. The midsummer drought over Mexico and Central America. *Journal of Climate*, 12(6).
- Maul, G. A., and F. M. Vukovich, 1993. "The Relationship between Variations in the Gulf of Mexico Loop Current and Straits of Florida Volume Transport." *Journal of Physical Oceanography* 23(5): 785–96. doi:10.1175/1520-0485(1993)023<0785:TRBVIT>2.0.CO;2.
- Nürnberg, D., M. Ziegler, C. Karas, R. Tiedemann, and M. W. Schmidt, 2008. "Interacting Loop Current Variability and Mississippi River Discharge over the Past 400 Kyr." *Earth and Planetary Science Letters* 272(1-2): 278–89. doi:10.1016/j.epsl.2008.04.051.
- Oey, L.-Y., and Y.-L. Chang. 2011. "Loop Current Cycle and Trigger Mechanism for Loop Current Ring Separations." *Proc. BOEMRE Info. Transfer Meeting, New Orleans, LA*.

- Oey, L.-Y., H.-C. Lee, and W. J. Schmitz. 2003. "Effects of Winds and Caribbean Eddies on the Frequency of Loop Current Eddy Shedding: A Numerical Model Study." *Journal of Geophysical Research: Oceans* 108 (C10): 22. doi:10.1029/2002JC001698.
- Oey, L.-Y., T. Ezer, and H.-C. Lee. 2005. "Loop Current, Rings and Related Circulation in the Gulf of Mexico: A Review of Numerical Models and Future Challenges" In *Circulation in the Gulf of Mexico: Observations and Models*, ed. Wilton Sturges and Alexis Lugo-Fernandez, 31–56. American Geophysical Union.
- Pichevin, T., and D. Nof. 1997. "The Momentum Imbalance Paradox." *Tellus A* 49 (2): 298–319. doi:10.1034/j.1600-0870.1997.t01-1-00009.x.
- Smith, S. R., J. Brolley, J. J. O'Brien, and C. A. Tartaglione. 2007. "ENSO's Impact on Regional U.S. Hurricane Activity." *Journal of Climate* 20 (7): 1404–1414. doi:10.1175/JCLI4063.1.
- Solidoro, C., V. Bandelj, P. Barbieri, G. Cossarini, and S. Fonda Umani. 2007. "Understanding dynamic of biogeochemical properties in the northern Adriatic Sea by using self-organizing maps and k-means clustering." *Journal of Geophysical Research: Oceans* 112, C07S90, doi:10.1029/2006JC003553.
- Sturges, W., N. G. Hoffmann, and R. R. Leben. 2010. "A Trigger Mechanism for Loop Current Ring Separations." *Journal of Physical Oceanography* 40 (5): 900–913. doi:10.1175/2009JPO4245.1.
- Tsui, I.-F., and C.-R. Wu. 2012. "Variability Analysis of Kuroshio Intrusion Through Luzon Strait Using Growing Hierarchical Self-organizing Map." *Ocean Dynamics* 62 (8): 1187–1194. doi:10.1007/s10236-012-0558-0.
- Xu, F.-H., Y.-L. Chang, L.-Y. Oey, and P. Hamilton. 2013. "Loop Current Growth and Eddy Shedding Using Models and Observations: Analyses of the July 2011 Eddy-Shedding Event." *Journal of Physical Oceanography* 43 (5): 1015–1027. doi:10.1175/JPO-D-12-0138.1.
- Yin, X.-Q., and L.-Y. Oey. 2007. "Bred-ensemble Ocean Forecast of Loop Current and Rings." *Ocean Modelling* 17 (4): 300–326. doi:10.1016/j.ocemod.2007.02.005.
- Yin, Y., X. Lin, Y. Li, and X. Zeng, 2014. "Seasonal variability of Kuroshio intrusion northeast of Taiwan as revealed by self-organizing map." *Chinese Journal of Oceanology and Limnology*, in press. doi:10.1007/s00343-015-4017-x.

## Figures

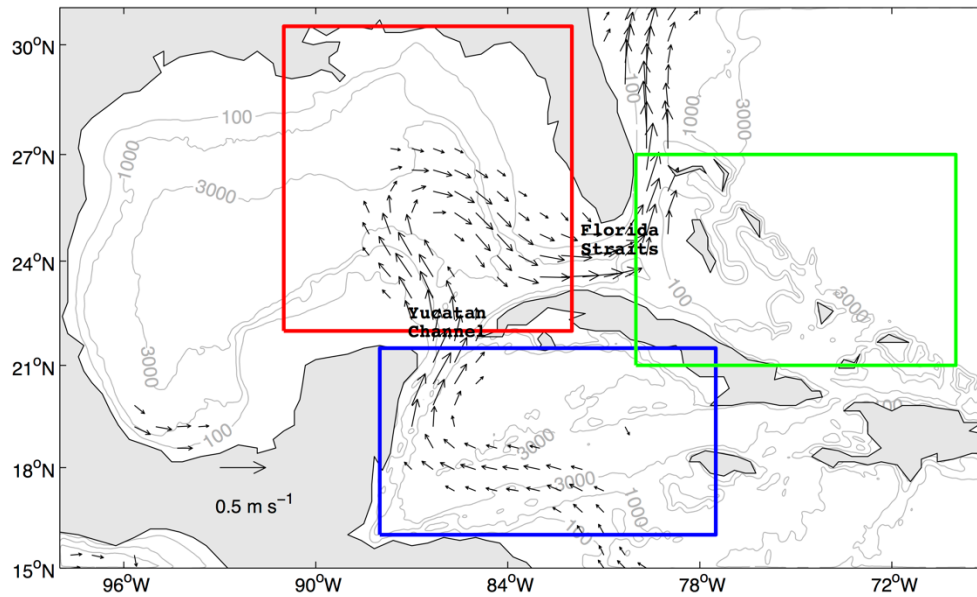
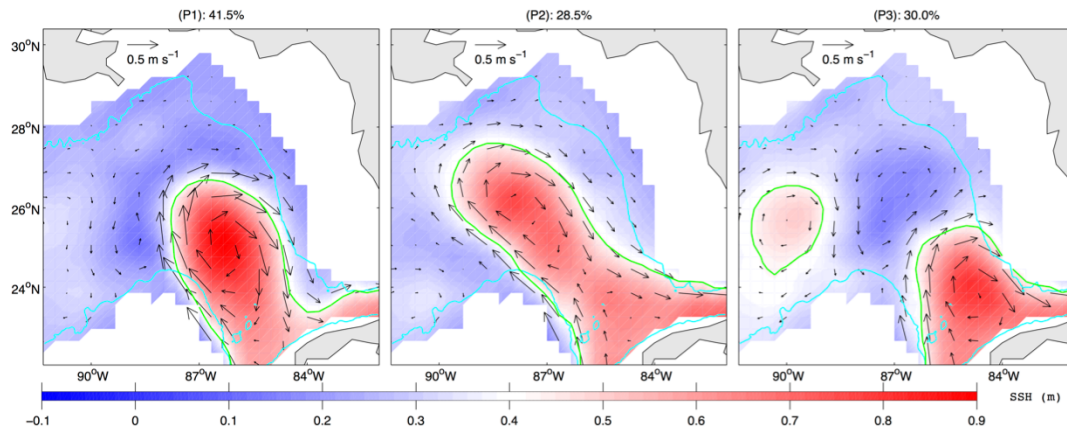
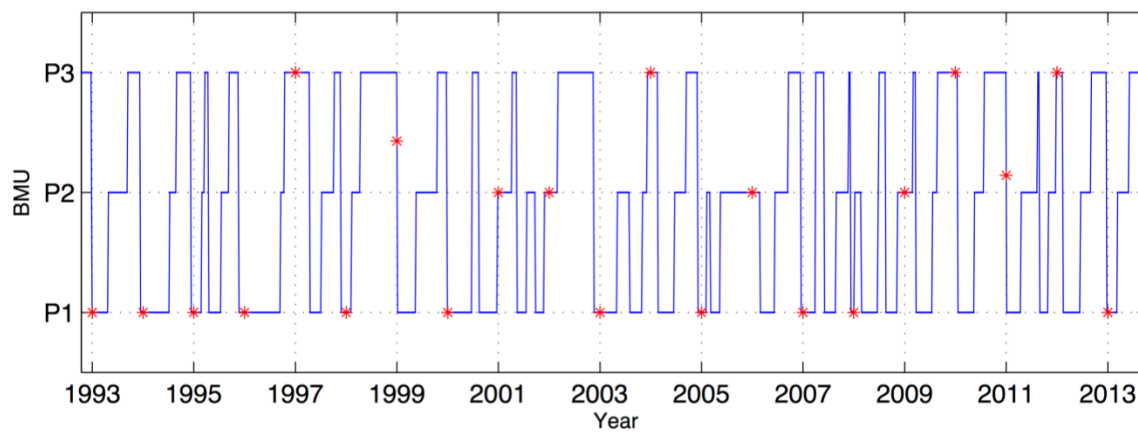


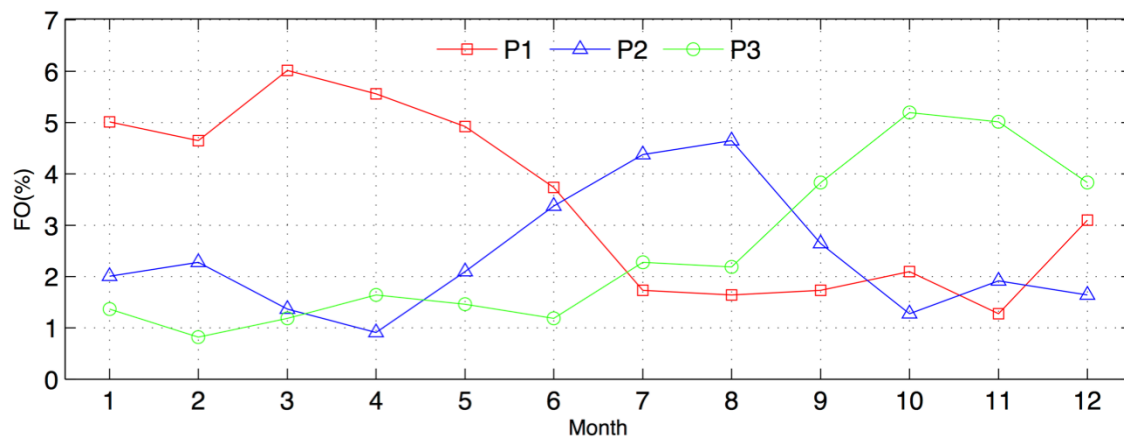
Figure 1. Study domain. Red box is the Gulf of Mexico (GoM) area; blue box is the Caribbean Sea (CS) area; green box is the Bahamas area. The box areas are used for wind stress curl calculations. Grey lines are depth contours in meters. Black arrows are geostrophic velocity calculated from long-term mean AVISO sea surface height data (only the velocities  $>0.1 \text{ m s}^{-1}$  are plotted). The Loop Current is visible via the velocity arrows in the GoM box.



(a)



(b)



(c)

Figure 2. Self-organizing map analysis results. (a) Sea surface height (SSH) patterns: (P1) normal; (P2) extension; (P3) retraction. Top numbers are corresponding frequency of occurrence (FO) percentage. Vectors are geostrophic current. Green line is 0.45 m SSH contour line. Cyan lines are 1000 m isobaths. Color scale: SSH in meters. (b) Best matching unit (BMU) time series of the three patterns in (a). Red stars are the first day of each year. (c) Monthly FOs of the three patterns in (a).

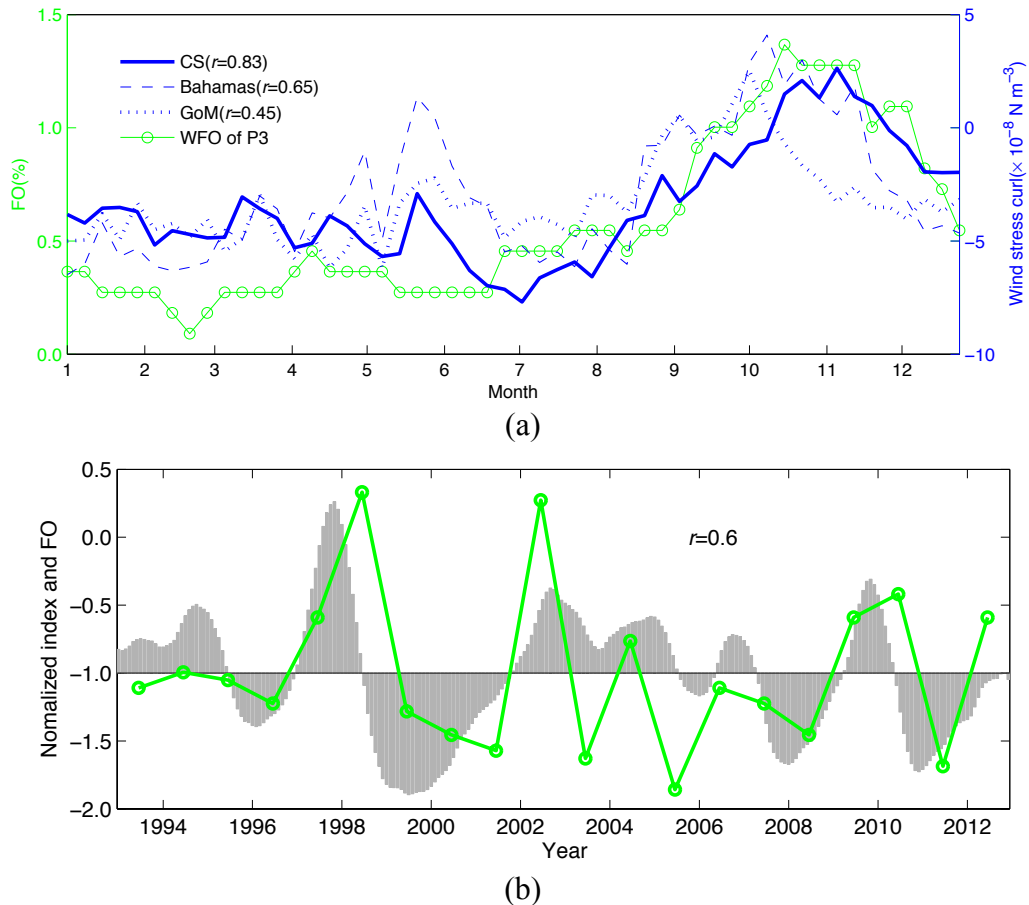


Figure 3. (a) Weekly frequency of occurrence (WFO) for Pattern 3 (P3) and wind stress curl of the areas in Figure 1. Zero-lag correlation coefficients ( $r$ ) for the relation between the WFO of P3 and the wind stress curl, at 95% confidence level for each domain, are shown in brackets after the domain. (b) Normalized Ocean Niño Index (six-month moving average; shaded area) and annual mean frequency of occurrence (FO) for P3 (green line). Correlation coefficient ( $r=0.6$ ) with Ocean Niño Index lagged 90 days is shown at 95% confidence interval.

**Chapter III: Predictability of the Loop Current variation and eddy shedding process in the Gulf of Mexico using an artificial neural network approach**

Xiangming Zeng, Yizhen Li, and Ruoying He

Department of Marine, Earth, and Atmospheric Sciences  
North Carolina State University, Raleigh, NC, USA 27695

*(Published in Journal of Atmospheric and Oceanic Technology, DOI:  
<http://dx.doi.org/10.1175/JTECH-D-14-00176.1>)*

## **Abstract**

A novel approach based on an artificial neural network was used to forecast sea surface height (SSH) in the Gulf of Mexico (GoM), in order to predict Loop Current variation and its eddy shedding process. We first applied the empirical orthogonal function analysis method to decompose long-term satellite observed SSH into spatial patterns (EOFs) and time-dependent principal components (PCs). The nonlinear autoregressive network was then developed to predict major PCs of the GoM SSH in the future. The prediction of SSH in the GoM was constructed by multiplying the EOFs and predicted PCs. Model sensitivity experiments were conducted to determine the optimal number of PCs. Validations against independent satellite observations indicate our neural network-based model can reliably predict Loop Current variations and its eddy shedding process for a four week period. In some cases, an accurate forecast for five to six weeks is possible.

## **1. Introduction**

Originating at the Yucatan Channel and exiting through the Florida Straits, the Loop Current (LC) is a dominant circulation feature in the Gulf of Mexico (GoM) (Figure 1). One of the most notable characteristics of LC is that it episodically sheds large, high-speed eddies with diameters of about 200-300 km and swirl speed of 1.8-2 m/s, which affect almost every aspect of the GoM including ocean circulation, biochemical properties, larvae transport, and air-sea interaction (Oey et al., 2005b; Xue et al., 2013; Richards et al., 1993; Small et al., 2008). Between eddy shedding, variations of LC frontal position are also significant. The

north and west edges of the LC can vary from about 25.5°N to 27.5°N and 86°W to 90°W, respectively (Leben, 2005; Gopalakrishnan et al., 2013a; Zeng et al., 2015).

Daily operations of approximately 4,000 oil and gas platforms in the northern GoM are significantly affected by the LC and its high-speed eddies, which make planning and scheduling a challenge for this expensive enterprise (Leben and Honaker, 2006; Sammarco et al., 2004). Accurate prediction of the LC and LC eddies is of critical importance for both scientific research and societal benefit. For example, in order to mitigate the adverse impacts of the *Deepwater Horizon* oil spill in 2010, intensive research on the LC and LC eddies was performed during and after the incident (e.g., Liu et al., 2013). The LC and LC eddies also play an active role in the rapid intensification of GoM hurricanes, such as devastating Hurricanes Katrina and Rita (Leben and Honaker, 2006), which caused extensive loss of life and property damage in many Gulf coastal communities.

Much effort has been expended to predict LC variation and its eddy shedding process using remote sensing observations and primitive equation numerical models. Oey et al. (2005a) performed a study to predict the LC and its eddy frontal position using the Princeton Ocean Model (POM). Yin and Oey (2007) applied the bred-ensemble forecast technique to estimate the locations and strengths of the LC and LC eddies from July to September 2005. Counillon and Bertino (2009) presented a small-ensemble forecast using the Hybrid Coordinate Ocean Model to predict LC eddy shedding. A semi-theoretical basis was provided by Lugo-Fernández and Leben (2010) on the linear relationship between LC retreat latitude and eddy separation period. Forristall et al. (2010) showed the better skill of statistical method on the LC prediction than most dynamical models. Mooers et al. (2012)

evaluated several different ocean models' performance at LC eddy shedding prediction using various prediction skill assessment methods in the report of the GoM 3-D Operational Ocean Forecast System Pilot Prediction Project. More recently, with the four-dimensional variation method, Gopalakrishnan et al. (2013) tested the predictability of the LC eddy shedding process using the Massachusetts Institute of Technology general circulation model (MITgcm). Xu et al. (2013) applied the local ensemble transform Kalman filter with the parallel POM to estimate the states of the LC and LC eddies from April to July 2010. All these studies are based on either simple empirical relations or primitive equation ocean models focusing on a single LC eddy or a small number of LC eddy shedding events. The lack of generality makes the assessment of their model predictability very difficult (e.g., Mooers et al., 2012).

In this paper, we applied a novel method based on an artificial neural network (ANN) and Empirical Orthogonal Function (EOF) analysis to the sea surface height (SSH) forecast in the GoM, in order to predict LC variation and its eddy shedding process. EOF analysis was used to decompose the SSH data into spatial and temporal components. The ANN was used to predict future temporal components variations. Future SSH was then constructed by combining the predicted temporal components with the spatial pattern. Various prediction skill assessment methods, such as prediction skill score, spatial correlation, and root mean square error, were conducted to evaluate this method's prediction skill on LC variation and eddy shedding process. The structure of this paper is as follows: the data and method are introduced in section 2; parameter experiments, prediction results, skill assessment, and predictability analysis are presented in section 3; followed by a summary in section 4.

## **2. Data and method**

### **2.1 Dataset**

Twenty-one years (1992-2013) of gridded, altimeter-based, absolute dynamic topography data were used in this study. The altimeter products were produced by Ssalto/Duacs and distributed by AVISO (Archiving, Validation and Interpretation of Satellite Oceanographic Data: <http://www.aviso.altimetry.fr/duacs/>). Specifically, we used the “Reference Series” dataset following Chelton et al. (2011) and Mason et al. (2014) for the more stable satellite sampling (Collecte Localisation Satellites, 2011). The data were constructed with two simultaneously operating altimeters, one in a 10-day exact repeat orbit (T/P, followed by Jason-1 and presently by Jason-2) and the other in a 35-day exact repeat orbit (ERS-1 followed by ERS-2 and presently by Envisat; Chelton et al., 2011). The data have spatial and temporal resolutions of  $1/3^\circ$  and 7 days, respectively (Collecte Localisation Satellites, 2011). We focus on the area of LC variation (indicated by the black box in Figure 1) to reduce the data dimension and increase the percentage of leading principal components in EOF analysis (see section 2d). For quality control, only the data located in the area with water depth greater than 100 m were chosen (Liu et al., 2008; Yin et al., 2014; Zeng et al., in revision). During the data selection process, the 2-minute gridded global relief topographic data (ETOPO2), distributed by the National Oceanic and Atmospheric Administration (NOAA) National Geophysical Data Center, was interpolated to the SSH grid to obtain a topographic dataset. Other ancillary data, including tracks of hurricanes and tropical storms,

were taken from NOAA's National Climatic Data Center and The Johns Hopkins University Applied Physics Laboratory.

## **2.2 Artificial neural network (ANN)**

The ANN is a computational model inspired by biological neural networks that is capable of solving a variety of problems in pattern recognition, time series prediction, and parameter optimization (e.g., Jain et al., 1996). It has been widely used for variable prediction and mapping in the geoscience community (e.g., Maier and Dandy, 2000; Maier et al., 2010; Krasnopolsky, 2013). Hsieh and Tang (1998), for example, proposed the use of ANN in meteorology and oceanography, then conducted a series of applications on Pacific sea surface temperature prediction (Tang et al., 2000; Hsieh, 2001), Lorenz dynamical system forecast (Tang and Hsieh, 2001), and El Niño-Southern Oscillation analysis (Hsieh, 2004). With wind and tidal information as inputs, Lee (2006) predicted storm surge events around Taiwan Island using the ANN method. Wu et al. (2006) presented the advantage of the ANN over regression in predicting tropical Pacific sea surface temperature. Many applications also appear in pyrometer measurements, wind shear alerting, and climate change (e.g., Oliveira et al., 2006; Kwong et al., 2011; Yip and Yau, 2012).

The ANN's basic elements are called neurons, which only execute summation over weighted input values, passing their results to a nonlinear transfer function to obtain neuron output values. A three-layer ANN with nonlinear transfer functions can be represented as a set of nonlinear equations used to calculate the output values from the input values (e.g., Maier and Dandy, 2000). In the first layer (input layer), each input variable has its own neurons. The second, hidden layer is represented by several neurons, whose number can vary

according to the complexity of the problem. Each neuron in the hidden layer receives inputs from all the neuron outputs of the first layer. This fully interconnected procedure is repeated again in the third, output layer. The output layer has one neuron for each output variable (Oliveira et al., 2006).

Each of the three layers has its own weighting factors, which are the ANN parameters determined during the training process. The training process is the determination of the proper interconnection of weighting factors for the ANN based on training dataset patterns, so that the output of the ANN can present the best fit with the output given by the testing dataset. In this way, the ANN learns the information given in the training dataset but still has a generalizing capability, not simply memorizing the patterns in training dataset. The generalizing capabilities of the ANN guarantee that the trained model can give reasonable results for unknown patterns that differ from the training dataset (Oliveira et al., 2006). These procedures and structures give the ANN the ability of a universal approximator (Maier and Dandy, 2000; Oliveira et al., 2006).

### **2.3 EOF analysis**

In our application, the large spatial and temporal span of the SSH dataset would bring too many input variables to the ANN, which makes direct prediction using the ANN infeasible. As a result, the ANN requires some expensive optimisation, and compression of the input dataset is necessary (Rixen et al., 2002). EOF analysis has been commonly used for decades in oceanographic and meteorological applications (e.g., Beckers and Rixen, 2003; Hannachi, 2004), and is applied in our study to provide a compressed dataset for ANN prediction. In oceanography, EOF analysis has been used for several purposes, such as

objective analysis of in situ data (e.g., Holbrook and Bindoff, 2000), statistical comparison between data and model results (e.g., Beckers et al., 2002), data reconstruction (e.g., Becker and Rixen, 2003; He et al., 2003; Miles and He, 2010; Zhao and He, 2012; Li and He, 2014), variability analysis (e.g., Hendricks et al., 1996), filtering (e.g., Vautard et al., 1992), and data compression (e.g., Pedder and Gomis, 1998; Rixen et al., 2002). EOF analysis can be done by applying the singular value decomposition (SVD) technique (e.g., Beckers and Rixen, 2003). Let  $\mathbf{X}$  be a  $n \times m$  matrix such that the rows indicate temporal development and the columns are variables or spatial data points. The SVD technique can break up the matrix  $\mathbf{X}$  into three matrices:

$$\mathbf{X} = \mathbf{U} * \mathbf{D} * \mathbf{V}^T \quad (1)$$

where  $\mathbf{U}$  and  $\mathbf{V}$  are orthonormal and  $\mathbf{D}$  is diagonal.  $\mathbf{V}^T$  is the spatial patterns (EOFs), and  $\mathbf{U} * \mathbf{D}$  is the time-dependent principal components (PCs). Let  $\lambda_i$  be the diagonal part of  $\mathbf{D}$  with  $i=1, \dots, m$ . Then, the ratio  $f_i = \lambda_i^2 / \sum_{i=1}^m \lambda_i^2$  is a measure of the variance contained in spatial pattern  $i$  compared to the total variance. It is often said that PC  $i$  explains  $(100 f_i)\%$  of the variance. The ratio is often the basis for deciding the number of PCs to retain for data compression, and the ones with small ratios are usually discarded (e.g., Beckers and Rixen 2003). Usually, the ratios have been sorted in decreasing order, so that the first several PCs explain the major variance of the dataset.

## 2.4 Prediction Procedure

The existing SSH of the GoM was chosen as a predictor of future SSH of the GoM using the ANN and EOF analysis. As we mentioned before, because the spatial area of this

study leads to too large data dimension, direct SSH prediction is infeasible. To avoid the curse of dimension, EOF analysis was used to split the data into spatial EOFs and time-dependent PCs. From Eq. (1), we have

$$\mathbf{X}=\mathbf{P}*\mathbf{E} \quad (2)$$

where  $\mathbf{X}$  is our dataset,  $\mathbf{P}$  is time-dependent PCs, and  $\mathbf{E}$  is spatial EOFs. Eq. (2) can be written in another form:

$$\begin{pmatrix} x_{1,1} & \cdots & x_{1,m} \\ \vdots & \ddots & \vdots \\ x_{n,1} & \cdots & x_{n,m} \end{pmatrix} = \begin{pmatrix} p_{1,1} & \cdots & p_{1,m} \\ \vdots & \ddots & \vdots \\ p_{n,1} & \cdots & p_{n,m} \end{pmatrix} \begin{pmatrix} e_{1,1} & \cdots & e_{1,m} \\ \vdots & \ddots & \vdots \\ e_{m,1} & \cdots & e_{m,m} \end{pmatrix} \quad (3)$$

where  $x_{i,j}$  is the  $j$ th spatial SSH point at time  $i$ ,  $n$  is the time index, and  $m$  is the number of spatial points.

Because the first several leading PCs represent the majority of the dataset's variation (Table 1), we can just use the first  $k$  PCs to reconstruct the original dataset without losing much information (e.g., Beckers and Rixen, 2003). That is,

$$\begin{pmatrix} x_{1,1} & \cdots & x_{1,m} \\ \vdots & \ddots & \vdots \\ x_{n,1} & \cdots & x_{n,m} \end{pmatrix} \approx \begin{pmatrix} p_{1,1} & \cdots & p_{1,k} \\ \vdots & \ddots & \vdots \\ p_{n,1} & \cdots & p_{n,k} \end{pmatrix} \begin{pmatrix} e_{1,1} & \cdots & e_{1,m} \\ \vdots & \ddots & \vdots \\ e_{k,1} & \cdots & e_{k,m} \end{pmatrix} \quad (4)$$

Similar as Alvarez et al. (2000), Rixen et al. (2001), and Alvarez (2003), we can get the approximation of SSH at time  $n+1$  by

$$\begin{pmatrix} x_{n+1,1} & \cdots & x_{n+1,m} \end{pmatrix} \approx \begin{pmatrix} p_{n+1,1} & \cdots & p_{n+1,k} \end{pmatrix} \begin{pmatrix} e_{1,1} & \cdots & e_{1,m} \\ \vdots & \ddots & \vdots \\ e_{k,1} & \cdots & e_{k,m} \end{pmatrix} \quad (5)$$

if we can predict  $\left( p_{n+1,1} \cdots p_{n+1,k} \right)$ .

The nonlinear autoregressive network with one hidden layer was chosen to do the PC prediction by following Maier and Dandy (2000). For a certain dataset, the PCs are independent of each other due to the property of EOF analysis (Hannachi, 2004). As a result, training and forecasting were applied to the PCs independently. That is,

$$p_{n+1, j} = f(p_{n, j}, p_{n-1, j}, \cdots, p_{n-i, j}) \quad (6)$$

where  $p_{n+1, j}$  is the value of  $j$ th PC of GoM SSH at the  $(n+1)$ th record, and  $i$  is time delay. Because the time interval of SSH data is weekly, this prediction is one week ahead. Once we get  $p_{n+1, j}$ , we can put it into Eq. (6) and use it to predict  $p_{n+2, j}$ . The loop can continue until the accuracy decreases to the lowest acceptable level. The larger the time delay is, the longer the required training time is. Starting from  $i=1$ , we tried different time delays. Take the correlation coefficient and root mean square error (RMSE) as the performance criterion of our prediction. We found that the prediction performance improved as the increase of time delay  $i$  until  $i=5$ . Therefore, the time delay for the ANN is set to be  $i=5$ , which gives the largest correlation coefficient and least RMSE. The optimal neuron number for each PC prediction was obtained in an iterative fashion based on Kaastra and Boyd (1996)'s criteria on neuron number selection.

Here a six-week leading prediction window was used to demonstrate the model prediction skill. We applied SSH data from October 14, 1994 to June 23, 2010 for the first six-week prediction. Then a weekly sliding window was applied from June 30, 2010 to June

19, 2013. During the ANN training procedure, 85% of the data were used for training and 15% were reserved for testing (Wu et al., 2006). In order to avoid over-fitting, the Bayesian regulation method, which is coded as the program ‘trainbr’ in the MATLAB Neural Network toolbox, was chosen for ANN training following Wu et al. (2006).

### **3. Results and discussion**

#### **3.1 Sensitivity of PC number selection**

Figure 2 shows the correlation coefficients of predicted and observation-derived first leading PCs of GoM SSH (which accounted for 30% of the variance) for different prediction weeks over three years (2010-2013). From Week 1 to 6, the correlation coefficients decrease from 1.00 to 0.82. For a one-week prediction, the ANN can predict the PC values almost exactly. While remaining highly correlated, the accuracy decreases as the prediction time grows. As shown in the prediction method Eq. (6), small errors in each prediction step can propagate into the next, and grow as the prediction time increases. For example, we can see obvious error increasing and propagating from Week 1 to 6 near May 11, 2012 (Figure 2). Other PCs’ predictions have similar results (not shown).

The future SSH of the GoM can be constructed using Eq. (5) with the predicted PCs from Eq. (6). According to the percentage variance accounted for by different PCs in EOF analysis, we chose three sets of PCs, corresponding to three percentage levels: 75%, 85%, and 95%, for the sensitivity tests (Table 1). In order to quantify the accuracy of prediction, spatial correlation coefficients and RMSE between predicted and observed GoM SSH were calculated for each experiment as the criteria of prediction performance. Large correlation

coefficients and small RMSE represent good prediction skill. According to Table 1, the experiment with 18 PCs has the largest mean spatial correlation coefficients and the least mean RMSE for the six-week prediction window. Generally, the more PCs that are used, the better the performance that can be achieved. However, this performance difference decreases from Week 1 to 6. Part of the reason is that the PCs that account for very small variance percentage are more noisy and difficult to predict. For example, the performance at Week 6 is the same for 9 and 18 PCs. As expected, the prediction performance degrades from Week 1 to 6, and it is because the time series prediction gets worse as the prediction time window extends (e.g., Figure 2).

### **3.2 SSH prediction skill assessment**

The following discussion is based on the experiment using 18 PCs, which gives us the best results among the three experiments (Table 1). From June 2010 to June 2013, the spatial correlation coefficients and RMSE between predicted and observed GoM SSH (Figure 3) show obvious variation of prediction performance: the correlation coefficients are larger than 0.8 from Week 1 to 3; starting from Week 4, the correlation coefficients gradually decrease and oscillate. RMSEs show an opposite pattern, with small errors in Weeks 1, 2 and 3 (generally less than 0.1 m), and larger oscillation from Week 4 to 6. Although the prediction performance decreases from Week 1 to 6, all the correlation coefficients of Week 4 and some of Week 5 and 6 are still larger than 0.7 (Figure 3), which means the general pattern of LC variation is well captured at least 4 weeks ahead, sometimes even 5 or 6 weeks ahead.

The oscillation of prediction performance may be due to the highly nonlinear variation of the LC, error propagation, and transitory sea level variability due to hurricane or

tropical storm influence. In particular, the sudden change of atmospheric conditions may cause unusual variation of LC and LC eddies (Oey et al., 2006; Shay and Uhlhorn, 2008). For example, at Week 6, the least correlation coefficients in October 2011, August 2012, and June 2013 occur during the passage of Hurricane Rina, Hurricane Ernesto, and Tropical Storm Andrea, respectively. We can also see obvious error propagation and amplification from Week 4 to 6 during these periods (Figure 3). Figure 1 shows the tracks of hurricanes and tropical storms passing through our study area during prediction period.

To better quantify the prediction skill of our method, we followed methods used by Oey et al. (2005a) and Mooers et al. (2012). First, we compared the SSH RMSE and skill score for prediction and persistence. The prediction RMSE of SSH at Week  $n$  is defined to

be  $\sqrt{\sum_{i=1}^k (SSHm_{i,n} - SSHo_{i,n})^2 / k}$ , where  $k$  is the total number of SSH data points in study

domain,  $SSHm_{i,n}$  is the  $i$ th data point of model SSH at Week  $n$ ,  $SSHo_{i,n}$  is the  $i$ th data point of observed SSH at Week  $n$ , and  $n=1,2,\dots,6$ . Similarly, the persistence RMSE of SSH at

Week  $n$  is defined to be  $\sqrt{\sum_{i=1}^k (SSHm_{i,0} - SSHo_{i,n})^2 / k}$ , where  $SSHo_{i,0}$  is the  $i$ th data point of

observed SSH at Week 0 for each prediction window. Figure 4 shows the SSH RMSE of prediction and persistence. The RMSE differences between prediction and persistence vary for each case. Generally, the RMSE grows with the increase of prediction time (from Week 1 to 6) for both prediction and persistence. However, the RMSE of prediction increases at a much slower rate than that of persistence, indicating our prediction has much better skill and outperforms the persistence. One case when prediction's RMSE is larger than persistence's

occurs around August 19, 2012, the period that Hurricanes Isaac and Ernesto passed through the LC area and northern Caribbean Sea, respectively (Figure 1). The sudden change in atmospheric conditions may have caused the unusual variation of LC and LC eddies, which decrease the predictability of our model. The averaged RMSE also shows the better skill of prediction than that of persistence (Figure 5).

Although the RMSE varies for each month, the monthly and three-year long-term mean RMSEs of prediction are generally smaller than their persistence counterparts. For example, for the first week, the three-year mean RMSE is almost the same for prediction and persistence. However, the three-year mean RMSE for persistence increases to about 0.18 m at Week 6, whereas the predicted one is only about 0.13 m.

An alternative view of the model's prediction skill is shown in Figure 6, which presents the same data as Figure 4 in terms of the skill score. The prediction skill score of SSH at Week  $n$  is defined to be:

$$SS = 1 - \left( \sum_{i=1}^k (SSHm_{i,n} - SSHo_{i,n})^2 / k \right) / \left( \sum_{i=1}^k (SSHo_{i,n} - \overline{SSHo_{i,n}})^2 / k \right) \quad (7)$$

where the bar represents the arithmetic mean (Murphy 1988; Mooers et al., 2012). The persistence skill score of SSH at Week  $n$  can be derived by simply replacing  $SSHm_{i,n}$  with  $SSHo_{i,0}$ . The skill score is based on mean square, including both bias and variance, in order to facilitate the intercomparison with respect to a constant mean sea surface throughout the prediction time period (Mooers et al., 2012).

The skill scores of both prediction and persistence decrease with the increase of prediction time, while the amplitude and rate of decrease are different for each prediction

case. Generally, the prediction skill score is greater than that of persistence and decays at a much slower rate. Similar to the RMSE case, the scenario when prediction skill was less than persistence skill occurred around August 19, 2012 when the variation of LC and LC eddies may be unusual due to the influences of hurricanes in or near study domain (Figure 1).

The averaged skill scores also show better skill of prediction than persistence (Figure 7). Although the skill score varies for each month and decreases from Week 1 to 6 for both prediction and persistence, the monthly and three-year mean skill scores of prediction are generally greater than their persistence counterparts. For example, the three-year mean skill score starts off the same for both prediction and persistence at Week 1. As the prediction time increases to 6 weeks, it decreases to about 0.1 for persistence, whereas our model still has 0.5 prediction skill.

### 3.3 Frontal position prediction skill assessment

The frontal position of the LC and LC eddies is another metric to measure the prediction skill of our method. Here, frontal position predictability is evaluated using the methodology of Oey et al. (2005a). Due to the properties of the EOF method, the prediction tends to smooth the SSH contours at reduced values of SSH, especially near the study boundary area. As a result, it's difficult to find an optimal reference SSH contour line for frontal position comparison between prediction and observation. After a series of experiments, we chose 0.45 m SSH contour lines as the representation of the LC and LC fronts to better facilitate our skill assessment (Zeng et al. 2015). Using seven stations as reference positions (stars in Figure 1), we define prediction error at Week  $n$  as  $E_{j,n} = dm_{j,n} - do_{j,n}$ , where  $dm_{j,n}$  is the shortest distance from predicted LC and LC eddies

fronts to the station  $j$  at week  $n$ ,  $do_{j,n}$  is the corresponding observed distance, and  $n=1,2,..6$ . We similarly define the persistence error at Week  $n$  to be  $P_{j,n} = do_{j,0} - do_{j,n}$ , where  $do_{j,0}$  is the shortest distance from observed LC and LC eddies fronts to the station  $j$  at Week 0. Considering the smoothing effect of EOF technique, we exclude the small eddies (perimeter < 300 km) and data points within  $\pm 0.5^\circ$  of the domain boundary for this comparison. Again, as prediction time increases, the RMSE of frontal position grows for both prediction and persistence (Figure 8). Although the values change for each prediction case, the RMSE of predicted frontal position is generally smaller than that of persistence. The large jumps of persistence RMSE (Figure 8) are the scenarios when the LC eddies move out of study domain.

Due the smoothing effect of EOF analysis, the model's prediction of frontal position is not as good as that of SSH. However, generally, the frontal position prediction is much better than that of persistence. The monthly and three-year mean RMSE of frontal position shows the model's advantage clearly (Figure 9). In order to avoid the bias associated with the large jumps in Figure 8, we excluded the large jump scenarios (>200 km) when calculating the means. Again, the RMSE of frontal position is different each month for both prediction and persistence. The mean RMSE over three years of predicted frontal position reaches about 60 km at Week 6, while it grows to about 85 km for persistence. The three-year mean RMSE of frontal position for prediction is less than that of persistence even for Week 1.

### 3.4 One LC eddy shedding example

Figure 10 shows the comparison of predicted and observed GoM SSH for one LC eddy shedding event that occurred during the study time period. Again, due to the smoothing property of the EOF method, the SSH between LC and LC eddies tends to be larger than observation, which makes it difficult to find an optimal contour line to represent the edges of LC and LC eddies for both prediction and observation. After several experiments, we choose 0.45 m and 0.51 m SSH contours as the required edges for observation and prediction, respectively, to demonstrate the eddy shedding process. Here, eddy detachment is defined as the separation of two SSH contour lines from one entire LC SSH contour line (Week 4 in Figure 10), which occurred simultaneously in the prediction and observation. We note that the choices of different SSH contour lines for prediction and observation are only for clear demonstration of the LC eddy shedding process.

The variation of LC and LC eddies occurs at the same time in both prediction and observation: at Week 1 and 2, LC extends to the 1000 m isobaths near 28°N, and the SSH on both sides of the extended LC is low; from Week 3, the LC eddy starts to shed from the LC; at Week 4, the SSH contour lines clearly show that the LC eddy is separated from the LC; from Week 5 to 6, the distance between the LC and shed eddy is further separated. Due to the statistical property of EOF analysis, there are some lower predicted SSH areas as compared to the observation, and the shed eddy tends to be smaller than the observed one. The influence of Tropical Storm (TS) Don during July 27-30, 2011 on GoM SSH may also have reduced the accuracy of our prediction (Figure 10). Although the track of TS Don doesn't lie directly on the LC, its influence on LC frontal eddies may still play an important role on LC

variation and the eddy shedding process (e.g., Le Hénaff et al., 2012; Androulidakis et al., 2014). In this case, LC eddy shedding can still be predicted four weeks ahead (Figure 10). Overall, although there were some differences between predicted and observed SSH values, the general evolution of the LC and LC eddies was well captured.

#### **4. Summary**

Twenty-one years of satellite data were used to build and test a nonlinear statistical model for predicting the GoM SSH, from which LC variation and the eddy shedding process can be predicted. To reduce the data dimension, we first applied the EOF analysis to decompose existing SSH into spatial patterns (EOFs) and time-dependent principal components (PCs). The nonlinear, autoregressive neural network was then used to predict leading PCs of the GoM SSH six weeks ahead. Finally, the future SSH of the GoM was constructed by multiplying the spatial EOFs of GoM SSH and the predicted PCs. Having tested the sensitivity of prediction results to different variance percentage levels, the 95% level (with 18 PCs) was selected for skill assessment and analysis.

To evaluate the prediction skill of this method, a six-week weekly sliding prediction window was performed over three years. We calculated the spatial correlation coefficients and RMSEs between predicted and observed SSH during the three years, then compared the skill assessment metrics between prediction and persistence, such as the SSH skill score and RMSE, and frontal position RMSE of the LC and LC eddies. For SSH prediction, the three year mean RMSE of prediction is about 30% less than that of persistence at Week 6. The three-year mean skill score of SSH prediction is about 0.5 compared to 0.1 for persistence at

Week 6. The RMSE of frontal position also shows better skill of prediction (60 km) over persistence (80 km).

Although there are some performance oscillations in the later weeks of prediction window, the generally high correlation coefficients and low RMSEs indicate the high accuracy of our method for LC variation and eddy shedding prediction. The skill comparison between prediction and persistence also validates the prediction skill of our methods. Generally, the model can capture the LC variation and eddy shedding process four weeks ahead, and in some cases, five and six weeks ahead is possible.

The prediction errors mainly come from the ANN PC prediction and EOF SSH construction. Due to the complexity of LC variation, the influence of atmospheric conditions, and the limit of available datasets, the input information may not be enough for the ANN to capture the underlying relation of PC variation. For example, the accuracy of prediction decreases when hurricanes or tropical storms happen in or near the study area. Part of the reason is that air-sea interaction was not built into our model, and these extreme events cannot be well predicted as this time. Because only the leading PCs were used for prediction and SSH construction, some information was omitted. However, due to the high dimensionality of the datasets and computational efficiency, EOF decomposition and construction techniques are necessary for our prediction.

Several advantages of the neural network method over primitive equation dynamical ocean models for LC prediction are: 1) the nonlinear temporal variation can be better captured; 2) the prediction accuracy has more generality; 3) the computation is usually faster than primitive ocean models; and 4) no boundary and forcing conditions or partial

differential equation discretization are needed. For phenomena such as the GoM LC and the LC eddy shedding process that cannot be well predicted by modern dynamical ocean models, this method provides an alternative means for accurate forecast.

### **Acknowledgement**

Research support provided by Gulf of Mexico Research Initiative/GISR through grant 02-S130202, NOAA grant NA11NOS0120033, NASA grants NNX12AP84G and NNX13AD80G is much appreciated. We also thank Dr. F. Semazzi for helpful discussion and J. Warrillow for editorial assistance. Constructive comments from two anonymous reviewers are also appreciated.

### **References**

- Alvarez, A., 2003: Performance of satellite-based ocean forecasting (SOFT) systems: a study in the Adriatic Sea. *J. Atmos. Oceanic Technol.*, **20**, 717–729. doi: [http://dx.doi.org/10.1175/1520-0426\(2003\)20<717:POSBOF>2.0.CO;2](http://dx.doi.org/10.1175/1520-0426(2003)20<717:POSBOF>2.0.CO;2)
- Alvarez, A., C. Lopez, M. Riera, E. Hernandez-Garcia, and J. Tintore., 2000: Forecasting the SST space-time variability of the Alboran Sea with genetic algorithms, *Geophys. Res. Lett.*, **27**, 2709–2712, 2000.
- Androulidakis, Y. S., V. H., Kourafalou, and M. Le Hénaff, M., 2014: Influence of frontal cyclones evolution on the 2009 (Ekman) and 2010 (Franklin) Loop Current Eddy detachment events, *Ocean Sci. Discuss.*, **11**, 1949-1994, doi:10.5194/osd-11-1949-2014.
- Beckers, J.-M., and Coauthors, 2002: Model intercomparison in the Mediterranean: MEDMEX simulations of the seasonal cycle. *J. Marine Syst.*, **33–34**, 215–251, doi:10.1016/S0924-7963(02)00060-X.
- Beckers, J. M., and M. Rixen, 2003: EOF Calculations and Data Filling from Incomplete Oceanographic Datasets. *J. Atmos. Oceanic Technol.*, **20**, 1839–1856, doi:10.1175/1520-0426(2003)20<1839:ECADFF>2.0.CO;2.

- Chang, Y.-L., and L.-Y. Oey, 2010: Why Can Wind Delay the Shedding of Loop Current Eddies? *J. Phys. Oceanogr.*, **40**, 2481–2495, doi:10.1175/2010JPO4460.1.
- Chelton, D. B., M. G. Schlax, and R. M. Samelson, 2011: Global observations of nonlinear mesoscale eddies. *Prog. Oceanogr.*, **91**, 167–216, doi:10.1016/j.pocean.2011.01.002.
- Collecte Localisation Satellites, 2011: *SSALTO/DUACS user handbook: (M)SLA and (M)ADT near-real time and delayed time products, version 2rev4, Rep. SALP-MU-P-EA-21065-CLS*, 49 pp., Ramonville St-Agne, France.
- Counillon, F., and L. Bertino, 2009: High-resolution ensemble forecasting for the Gulf of Mexico eddies and fronts. *Ocean Dynam.*, **59**, 83–95, doi: 10.1007/s10236-008-0167-0.
- Cushman-Roisin, B., and J.-M. Beckers, 2011: *Introduction to Geophysical Fluid Dynamics: Physical and Numerical Aspects*. Academic Press, 851pp.
- Forristall, G.Z., R.R. Leben, C.A. Hall, 2010: A Statistical Hindcast and Forecast Model for the Loop Current. Offshore Technology Conference, 3-6 May 2010, Houston, Texas, USA, Paper OTC-20602-MS, 12 pp., doi:10.4043/20602-MS.
- Gopalakrishnan, G., B. D. Cornuelle, and I. Hoteit, 2013a. Adjoint sensitivity studies of loop current and eddy shedding in the Gulf of Mexico. *J. Geophys. Res-Oceans*, **118**, 3315–3335, doi:10.1002/jgrc.20240.
- Gopalakrishnan, G., B. D. Cornuelle, I. Hoteit, D. L. Rudnick, and W. B. Owens, 2013b: State estimates and forecasts of the loop current in the Gulf of Mexico using the MITgcm and its adjoint. *J. Geophys. Res-Oceans*, **118**, 3292-3314, doi:10.1002/jgrc.20239.
- Hannachi A., 2004. A primer for EOF analysis of climate data. <http://www.met.rdg.ac.uk/~han/Monitor/eofprimer.pdf>
- He, R., R. H. Weisberg, H. Zhang, F. E. Muller-Karger, and R. W. Helber, 2003: A cloud-free, satellite-derived, sea surface temperature analysis for the West Florida Shelf. *Geophys. Res. Lett.*, **30**, doi:10.1029/2003GL017673.
- Hendricks, J. R., R. R. Leben, G. H. Born, and C. J. Koblinsky, 1996: Empirical orthogonal function analysis of global TOPEX/POSEIDON altimeter data and implications for

- detection of global sea level rise. *J. Geophys. Res.*, **101**, 14131–14145, doi:10.1029/96JC00922.
- Holbrook, N. J., and N. L. Bindoff, 2000: A Statistically Efficient Mapping Technique for Four-Dimensional Ocean Temperature Data. *J. Atmos. Oceanic Technol.*, **17**, 831–846, doi:10.1175/1520-0426(2000)017<0831:ASEMTF>2.0.CO;2.
- Hsieh, W. W., 2001: Nonlinear principal component analysis by neural networks. *Tellus A*, **53**, 599–615, doi:10.1034/j.1600-0870.2001.00251.x.
- \_\_\_, 2004: Nonlinear multivariate and time series analysis by neural network methods. *Rev. Geophys.*, **42**, RG1003, doi:10.1029/2002RG000112.
- \_\_\_, and B. Tang, 1998: Applying Neural Network Models to Prediction and Data Analysis in Meteorology and Oceanography. *B. Am. Meteorol. Soc.*, **79**, 1855–1870, doi:10.1175/1520-0477(1998)079<1855:ANNMTP>2.0.CO;2.
- Jain, A. K., J. Mao, and K. M. Mohiuddin, 1996: Artificial neural networks: a tutorial. *Computer*, **29**, 31–44, doi:10.1109/2.485891.
- Kaastra, I., and M. Boyd, 1996: Designing a neural network for forecasting financial and economic time series. *Neurocomputing*, **10**, 215–236, doi:10.1016/0925-2312(95)00039-9.
- Krasnopolsky, V., 2013: *The Application of Neural Networks in the Earth System Sciences: Neural Networks Emulations for Complex Multidimensional Mappings*. Springer Science & Business, 205 pp.
- Kwong, K. M., M. H. Y. Wong, J. N. K. Liu, and P. W. Chan, 2011: An Artificial Neural Network with Chaotic Oscillator for Wind Shear Alerting. *J. Atmos. Oceanic Technol.*, **29**, 1518–1531, doi:10.1175/2011JTECHA1501.1.
- Le Hénaff, M., V. H. Kourafalou, Y. Morel, and A. Srinivasan, 2012: Simulating the dynamics and intensification of cyclonic Loop Current Frontal Eddies in the Gulf of Mexico. *J. Geophys. Res-Oceans*, **117**, C02034, doi:10.1029/2011JC007279.
- Leben, R. R., 2005: Altimeter-Derived Loop Current Metrics. *Circulation in the Gulf of Mexico: Observations and Models*, W. Sturges and A. Lugo-Fernandez, Eds., American Geophysical Union, 181–201.

- \_\_\_, and D. J. Honaker, 2006: What Do We Know and What Can We Predict About the Timing of Loop Current Eddy Separation? ESA Special Publication, Vol. 614 of, ESA Special Publication, 19.
- Lee, T.-L., 2006: Neural network prediction of a storm surge. *Ocean Eng.*, 33, 483–494, doi:10.1016/j.oceaneng.2005.04.012.
- Li, Y., and R. He, 2014: Spatial and temporal variability of SST and ocean color in the Gulf of Maine based on cloud-free SST and chlorophyll reconstructions in 2003–2012. *Remote Sens. Environ.*, 144, 98–108, doi:10.1016/j.rse.2014.01.019.
- Liu, Y., Weisberg, R.H., and Yuan, Y., 2008: Patterns of upper layer circulation variability in the South China Sea from satellite altimetry using the Self-Organizing Map. *Acta Oceanol. Sin.*, 27(Supp.), 129–144.
- Liu, Y., A. MacFadyen, Z.-G. Ji, and R. H. Weisberg, 2013: Monitoring and Modeling the Deepwater Horizon Oil Spill: A Record Breaking Enterprise. John Wiley & Sons, 280 pp.
- Lugo-Fernández, A., 2007: Is the Loop Current a Chaotic Oscillator? *J. Phys. Oceanogr.*, 37, 1455–1469, doi:10.1175/JPO3066.1.
- \_\_\_, and R. R. Leben, 2010: On the Linear Relationship between Loop Current Retreat Latitude and Eddy Separation Period. *J. Phys. Oceanogr.*, 40, 2778–2784, doi:10.1175/2010JPO4354.1.
- Maier, H. R., and G. C. Dandy, 2000: Neural networks for the prediction and forecasting of water resources variables: a review of modelling issues and applications. *Environ. Modell. Softw.*, 15, 101–124, doi:10.1016/S1364-8152(99)00007-9.
- \_\_\_, A. Jain, G. C. Dandy, and K. P. Sudheer, 2010: Methods used for the development of neural networks for the prediction of water resource variables in river systems: Current status and future directions. *Environ. Modell. Softw.*, 25, 891–909, doi:10.1016/j.envsoft.2010.02.003.
- Makarynsky, O., D. Makarynska, M. Kuhn, and W. E. Featherstone, 2004: Predicting sea level variations with artificial neural networks at Hillarys Boat Harbour, Western Australia. *Estua. Coast Shelf S.*, 61, 351–360, doi:10.1016/j.ecss.2004.06.004.

- Mason, E., A. Pascual, and J. C. McWilliams, 2014: A New Sea Surface Height Based Code for Oceanic Mesoscale Eddy Tracking. *J. Atmos. Oceanic Technol.*, 140312141126001, doi:10.1175/JTECH-D-14-00019.1.
- Miles, T. N., and R. He, 2010: Temporal and spatial variability of Chl-a and SST on the South Atlantic Bight: Revisiting with cloud-free reconstructions of MODIS satellite imagery. *Cont. Shelf Res.*, 30, 1951–1962, doi:10.1016/j.csr.2010.08.016.
- Mooers, C. N. K., Zaron, E. D., and Howard, M. K., 2012: Final Report for Phase I: Gulf of Mexico 3-D Operational Ocean Forecast System Pilot Prediction Project (GOMEX-PPP).
- Murphy, A. H., 1988: Skill Scores Based on the Mean Square Error and Their Relationships to the Correlation Coefficient. *Mon. Wea. Rev.*, 116, no. 12: 2417–24. doi:10.1175/1520-0493(1988)116<2417:SSBOTM>2.0.CO;2.
- Oey, L.-Y., H.-C. Lee, and W. J. Schmitz, 2003: Effects of winds and Caribbean eddies on the frequency of Loop Current eddy shedding: A numerical model study. *J. Geophys. Res.-Oceans*, 108, 3324, doi:10.1029/2002JC001698.
- \_\_\_, T. Ezer, G. Forristall, C. Cooper, S. DiMarco, and S. Fan, 2005a: An exercise in forecasting loop current and eddy frontal positions in the Gulf of Mexico. *Geophys. Res. Lett.*, 32, L12611, doi:10.1029/2005GL023253.
- \_\_\_, \_\_\_, and H.-C. Lee, 2005b: Loop Current, Rings and Related Circulation in the Gulf of Mexico: A Review of Numerical Models and Future Challenges. *Circulation in the Gulf of Mexico: Observations and Models*, W. Sturges and A. Lugo-Fernandez, Eds., American Geophysical Union, 31–56.
- \_\_\_, 2008: Loop Current and Deep Eddies. *J. Phys. Oceanogr.*, 38, 1426–1449, doi:10.1175/2007JPO3818.1.
- \_\_\_, T. Ezer, D.-P. Wang, S.-J. Fan, and X.-Q. Yin, 2006: Loop Current warming by Hurricane Wilma. *Geophys. Res. Lett.*, 33, L08613, doi:10.1029/2006GL025873.
- Oliveira, A. P., J. Soares, M. Z. Božnar, P. Mlakar, and J. F. Escobedo, 2006: An Application of Neural Network Technique to Correct the Dome Temperature Effects on Pyrgeometer Measurements. *J. Atmos. Oceanic Technol.*, 23, 80–89, doi:10.1175/JTECH1829.1.

- Pedder, M., and D. Gomis, 1998: Applications of EOF Analysis to the Spatial Estimation of Circulation Features in the Ocean Sampled by High-Resolution CTD Soundings. *J. Atmos. Oceanic Technol.*, 15, 959–978, doi:10.1175/1520-0426(1998)015<0959:AOEATT>2.0.CO;2.
- Richards, W. J., M. F. McGowan, T. Leming, J. T. Lamkin, and S. Kelley, 1993: Larval Fish Assemblages at the Loop Current Boundary in the Gulf of Mexico. *B. Mar. Sci.*, 53: 475–537.
- Rixen, M., J.-M. Beckers, A. Alvarez, and J. Tintore, 2002: Results on SSH neural network forecasting in the Mediterranean Sea. *Proc. SPIE 4544, Remote Sensing of the Ocean and Sea Ice 2001*, doi:10.1117/12.452757.
- Sammarco, P. W., A. D. Atchison, and G. S. Boland, 2004: Expansion of coral communities within the Northern Gulf of Mexico via offshore oil and gas platforms. *Mar. Ecol. Prog. Ser.*, 280, 129–143, doi:10.3354/meps280129.
- Shay, L. K., and E. W. Uhlhorn, 2008: Loop Current Response to Hurricanes Isidore and Lili. *Mon. Wea. Rev.*, 136, 3248–3274, doi:10.1175/2007MWR2169.1.
- Small, R. J., S. P. deSzoek, S. P. Xie, L. O’Neill, H. Seo, Q. Song, P. Cornillon, M. Spall, and S. Minobe, 2008: Air–sea Interaction over Ocean Fronts and Eddies. *Dynam. Atmos. Oceans, OCEANIC FRONTS*, 45: 274–319. doi:10.1016/j.dynatmoce.2008.01.001.
- Tang, B., W. W. Hsieh, A. H. Monahan, and F. T. Tangang, 2000: Skill Comparisons between Neural Networks and Canonical Correlation Analysis in Predicting the Equatorial Pacific Sea Surface Temperatures. *J. Climate*, 13, 287, doi: 10.1175/1520-0442(2000)013<0287:SCBNNA>2.0.CO;2
- Tang, Y., and W. W. Hsieh, 2001: Coupling Neural Networks to Incomplete Dynamical Systems via Variational Data Assimilation. *Mon. Wea. Rev.*, 129, 818–834, doi: 10.1175/1520-0493(2001)129<0818:CNNTID>2.0.CO;2.
- Vautard, R., P. Yiou, and M. Ghil, 1992: Singular-spectrum analysis: A toolkit for short, noisy chaotic signals. *Physica D*, 58, 95–126, doi:10.1016/0167-2789(92)90103-T.
- Wu, A., W. W. Hsieh, and B. Tang, 2006: Neural network forecasts of the tropical Pacific sea surface temperatures. *Neural Networks*, 19, 145–154, doi:10.1016/j.neunet.2006.01.004.

- Xu, F.-H., L.-Y. Oey, Y. Miyazawa, and P. Hamilton, 2013: Hindcasts and forecasts of Loop Current and eddies in the Gulf of Mexico using local ensemble transform Kalman filter and optimum-interpolation assimilation schemes. *Ocean Model.*, 69, 22–38, doi:10.1016/j.ocemod.2013.05.002.
- Xue, Z., R. He, K. Fennel, W.-J. Cai, S. Lohrenz, and C. Hopkinson, 2013: Modeling Ocean Circulation and Biogeochemical Variability in the Gulf of Mexico. *Biogeosciences*, 10: 7219–34. doi:10.5194/bg-10-7219-2013.
- Yin, X.-Q., and L.-Y. Oey, 2007: Bred-ensemble ocean forecast of loop current and rings. *Ocean Model.*, 17, 300–326, doi:10.1016/j.ocemod.2007.02.005.
- Yin, Y., X. Lin, Y. Li, and X. Zeng, 2014: Seasonal variability of Kuroshio intrusion northeast of Taiwan as revealed by self-organizing map. *Chin. J. Oceanol. Limn.*, in press. doi:10.1007/s00343-015-4017-x.
- Yip, Z. K., and M. K. Yau, 2012: Application of Artificial Neural Networks on North Atlantic Tropical Cyclogenesis Potential Index in Climate Change. *J. Atmos. Oceanic Technol.*, 29, 1202–1220, doi:10.1175/JTECH-D-11-00178.1.
- Zeng, X., Y. Li, R. He, and Y. Yin, 2015: Clustering of Loop Current patterns based on the satellite-observed sea surface height and self-organizing map. *Remote Sens. Lett.*
- Zhao, Y., and R. He, 2012: Cloud-free sea surface temperature and colour reconstruction for the Gulf of Mexico: 2003–2009. *Remote Sens. Lett.* 3, 697–706, doi:10.1080/01431161.2012.666638.

## Tables

Table 1. Principal Component (PC) number settings for Gulf of Mexico (GoM) sea surface height and corresponding time-averaged (2010-2013) spatial correlation coefficients (bold numbers) and root mean square errors (unit: m) between prediction and observation. PC percentage is the percentage variance accounted for by different PCs.

PC number	PC percent	Week 1	Week 2	Week 3	Week 4	Week 5	Week 6
5	75%	<b>0.889</b>	<b>0.884</b>	<b>0.867</b>	<b>0.838</b>	<b>0.800</b>	<b>0.758</b>
		0.101	0.106	0.112	0.130	0.145	0.157
9	85%	<b>0.939</b>	<b>0.930</b>	<b>0.905</b>	<b>0.865</b>	<b>0.815</b>	<b>0.765</b>
		0.074	0.083	0.100	0.121	0.140	0.155
18	95%	<b>0.974</b>	<b>0.960</b>	<b>0.925</b>	<b>0.874</b>	<b>0.817</b>	<b>0.765</b>
		0.049	0.065	0.092	0.119	0.140	0.155

## Figures

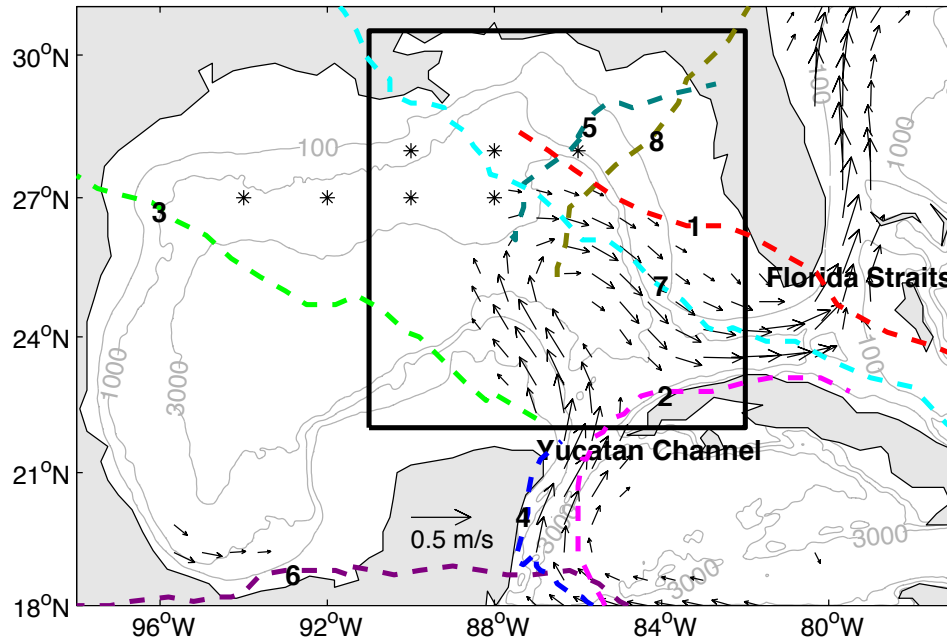


Figure 1. Study domain. Black box is study area in the Gulf of Mexico (GoM). Stars are the seven reference stations for frontal position comparison. Grey lines are depth contours in meters. Black arrows are geostrophic velocity calculated from long-term mean AVISO sea surface height data (only the velocities  $>0.1$  m/s are plotted). The Loop Current is visible via the velocity arrows in the GoM box. Dash lines are tracks of hurricanes or tropical storms (TS) from July 2010 to July 2013. 1: TS Bonnie, July 22-25, 2010; 2: Hurricane Paula during October 11-15, 2010; 3: TS Don, July 27-30, 2011; 4: Hurricane Rina, October 22-29, 2011; 5: TS Debby, June 23-27, 2012; 6: Hurricane Ernesto, August 1-10, 2012; 7: Hurricane Isaac, August 20-30, 2012; 8: TS Andrea, June 5-10, 2013. The tracks of hurricanes and tropical storms are from NOAA National Climatic Data Center and The Johns Hopkins University Applied Physics Laboratory.

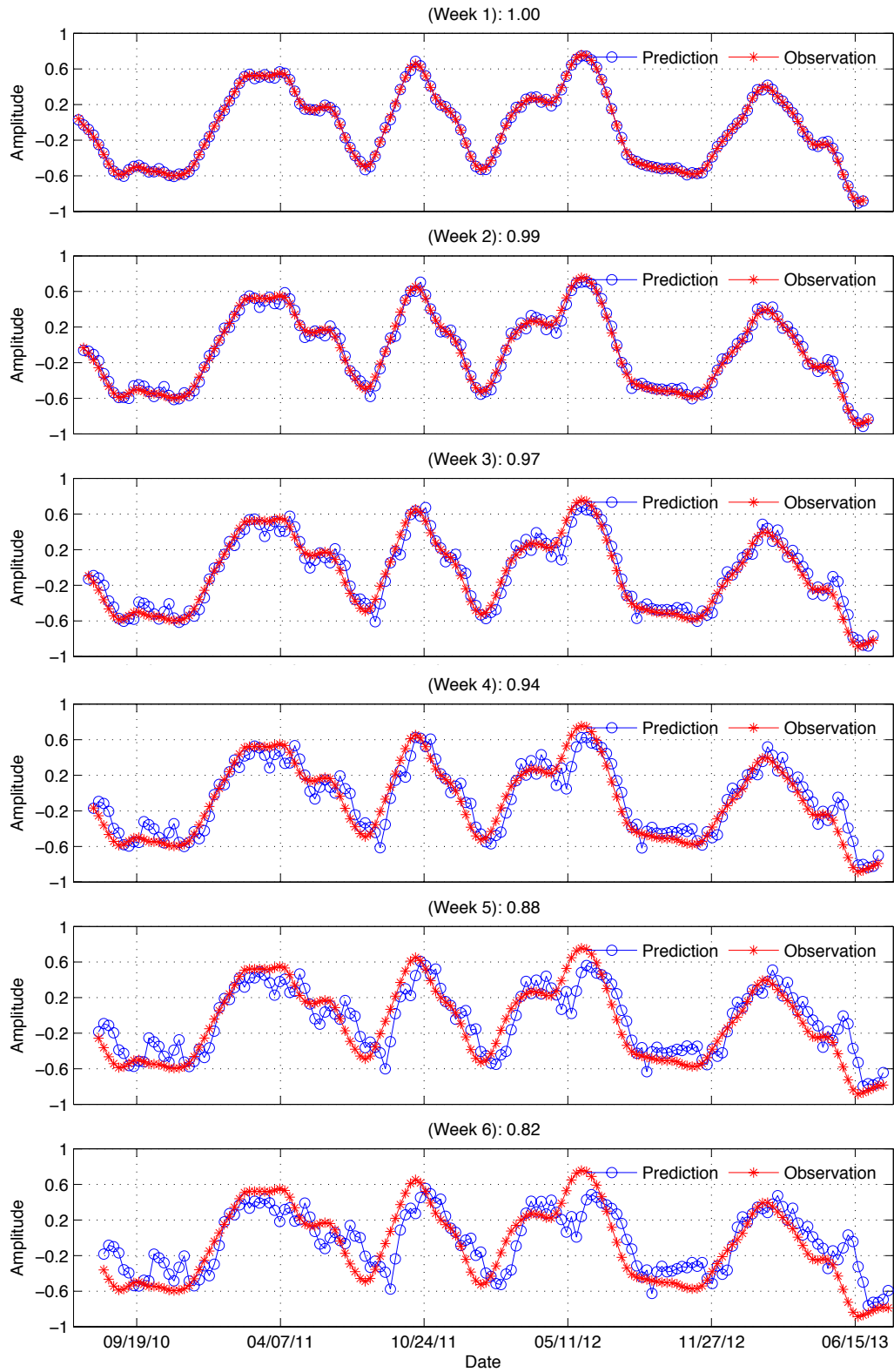


Figure 2. Comparison between predicted (circles) and observation-derived (stars) first leading principal component of GoM SSH from 2010 to 2013. Correlation coefficients are presented at the top of each figure.

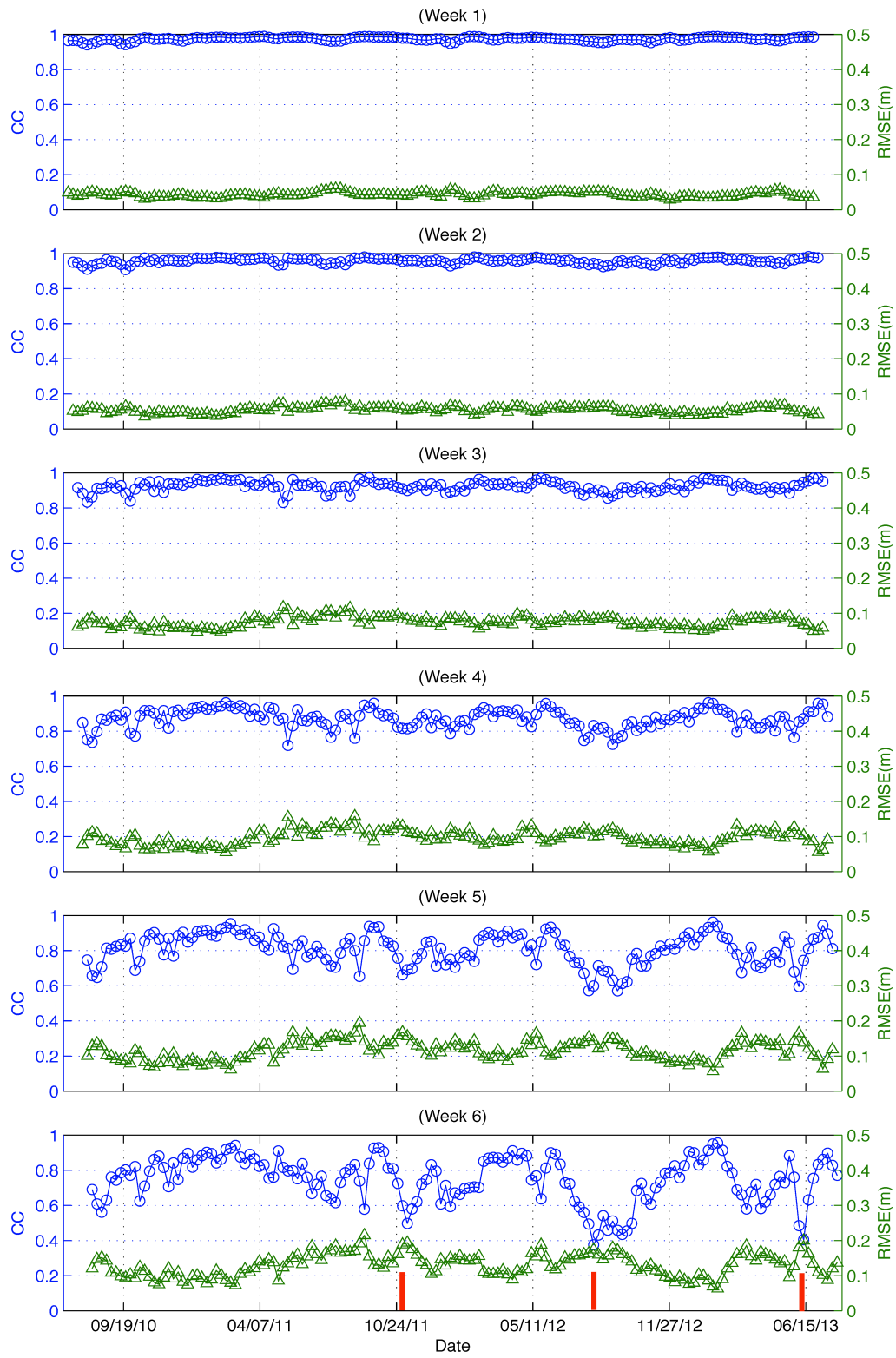


Figure 3. Spatial correlation coefficients (CC) and root mean square errors (RMSE) of predicted and observed sea surface height in the study area from 2010 to 2013 with a six-week ahead weekly sliding prediction window, using 18 PCs. Circles are CC points, and triangles are RMSE points. Red lines in week 6 indicate the approximate passing time of Hurricane Rina in 2011, Hurricane Ernesto in 2012, and Tropical Storm Andrea in 2013.

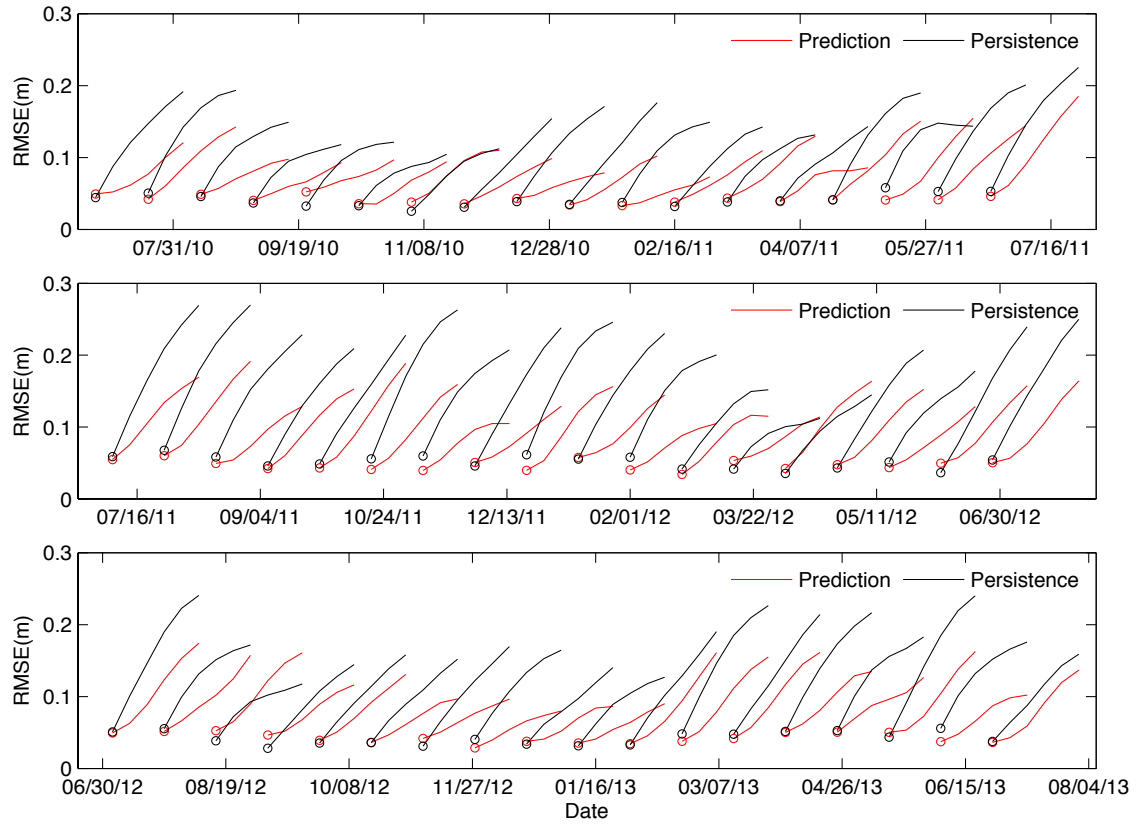


Figure 4. Root Mean Square Error (RMSE) comparison of sea surface height between prediction (red) and persistence (black). Circles represent the location of week 1. The values are plotted every four weeks.

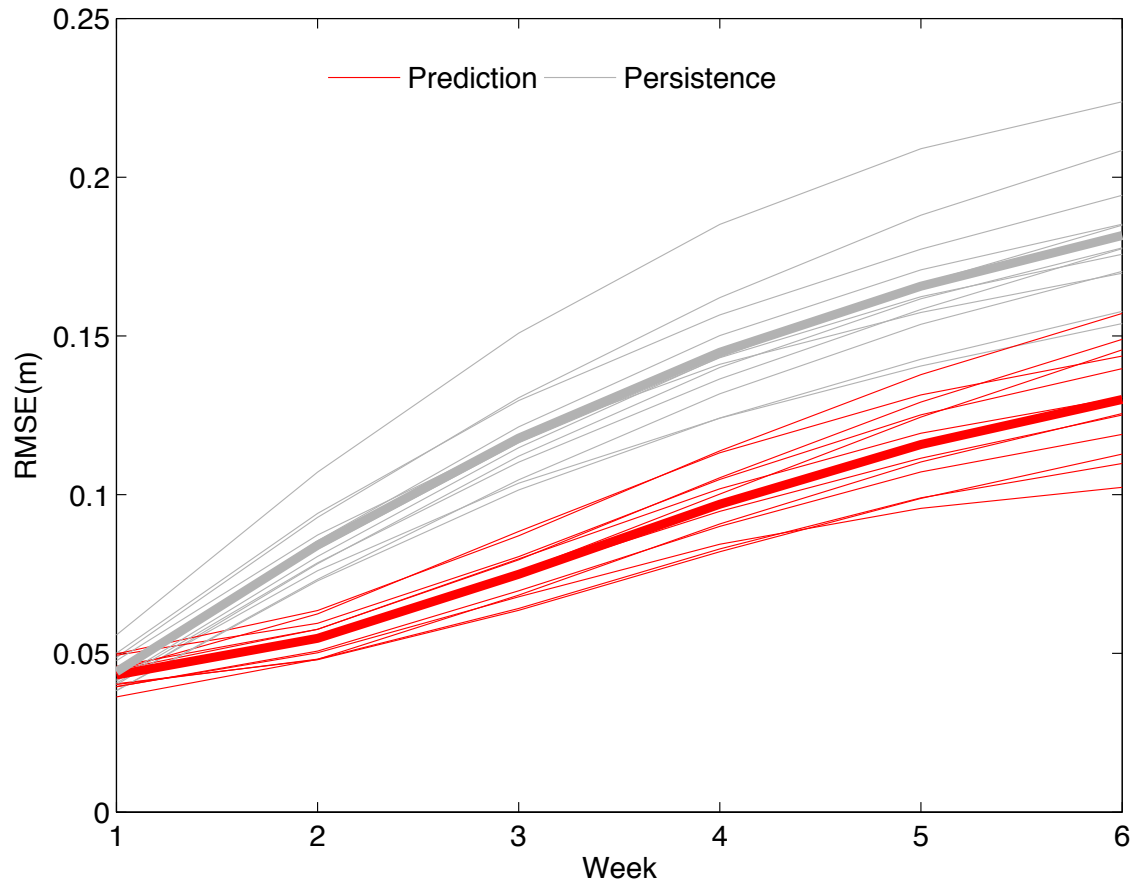


Figure 5. Averaged Root Mean Square Error (RMSE) of sea surface height for prediction (red) and persistence (grey). Thin lines are monthly means, and thick lines are means over the three-year prediction period.

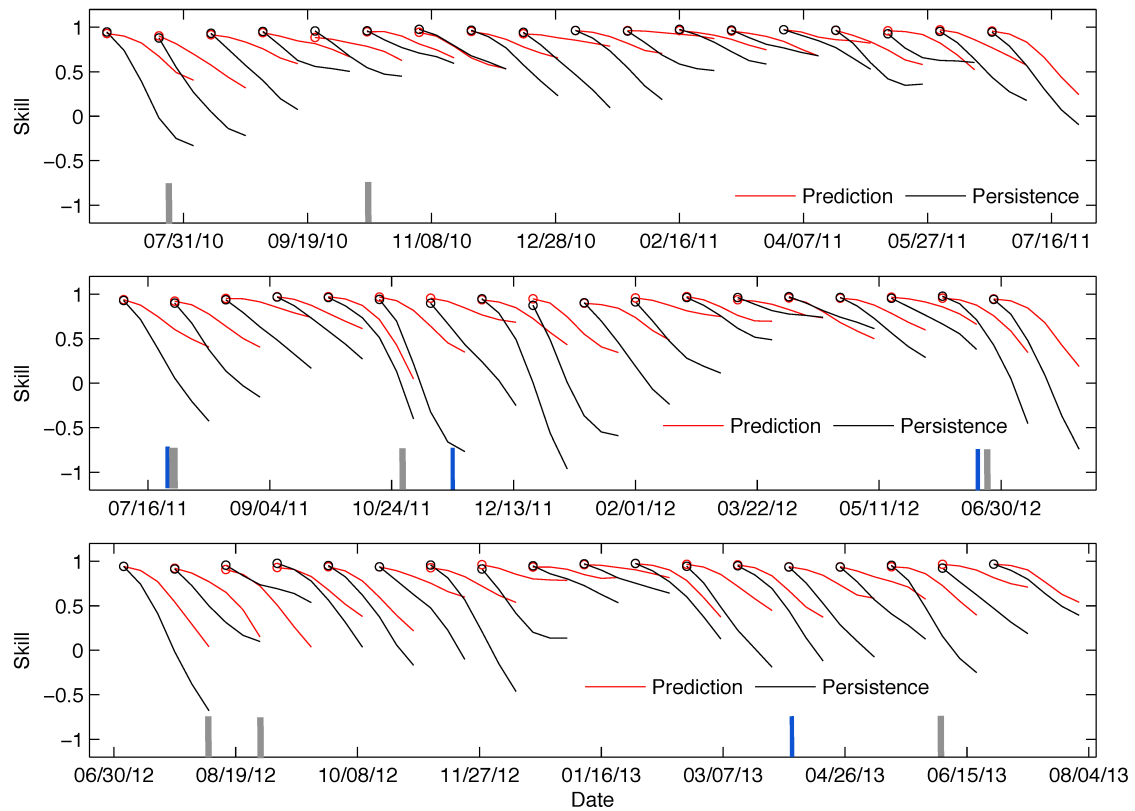


Figure 6. Skill score comparison of sea surface height between prediction (red) and persistence (black). Circles represent the location of Week 1. The values are plotted every four weeks. Grey short lines represent the approximate passing time of hurricanes or tropical storms in Figure 1. Blue short lines indicate the time of Loop Current eddy shedding.

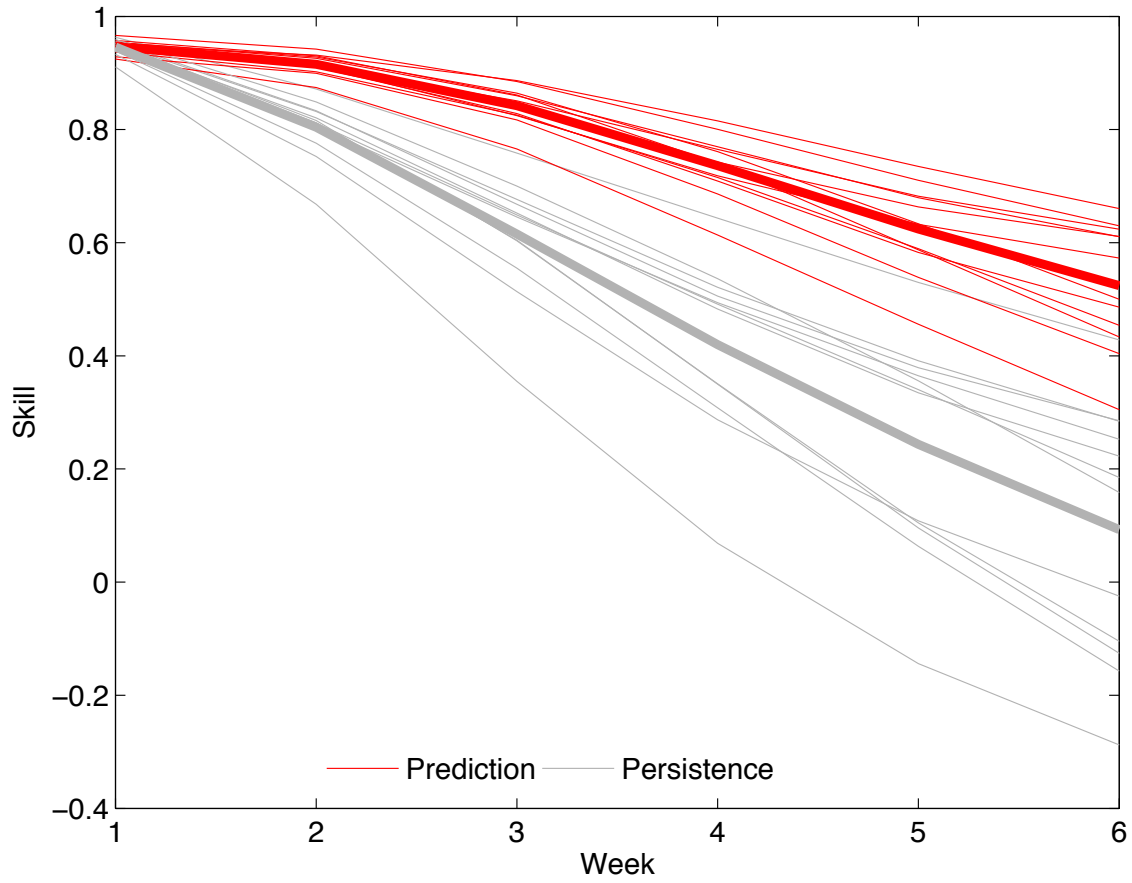


Figure 7. Averaged skill score of sea surface height for prediction (red) and persistence (grey). Thin lines are monthly mean, and thick lines are means over the three-year prediction period.

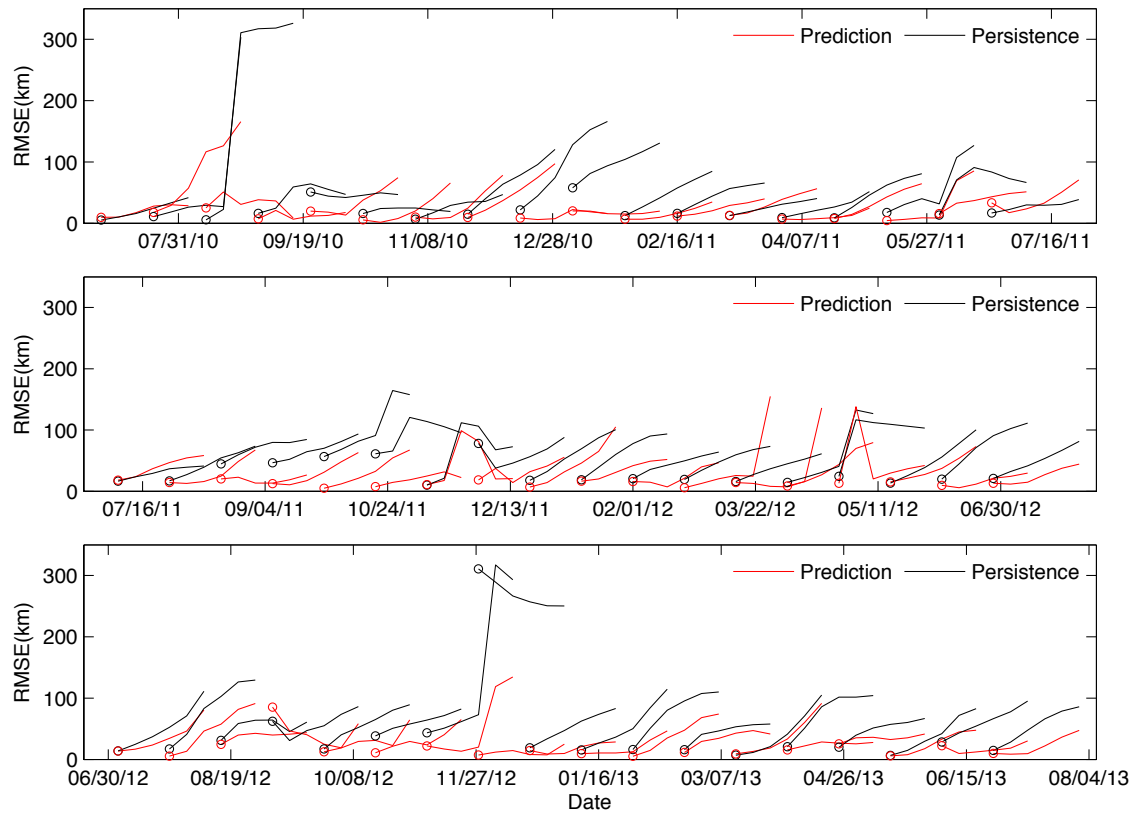


Figure 8. Frontal position Root Mean Square Error (RMSE) comparison of Loop Current and Loop Current eddies between prediction (red) and persistence (black). Circles represent the location of Week 1. The values are plotted every four weeks.

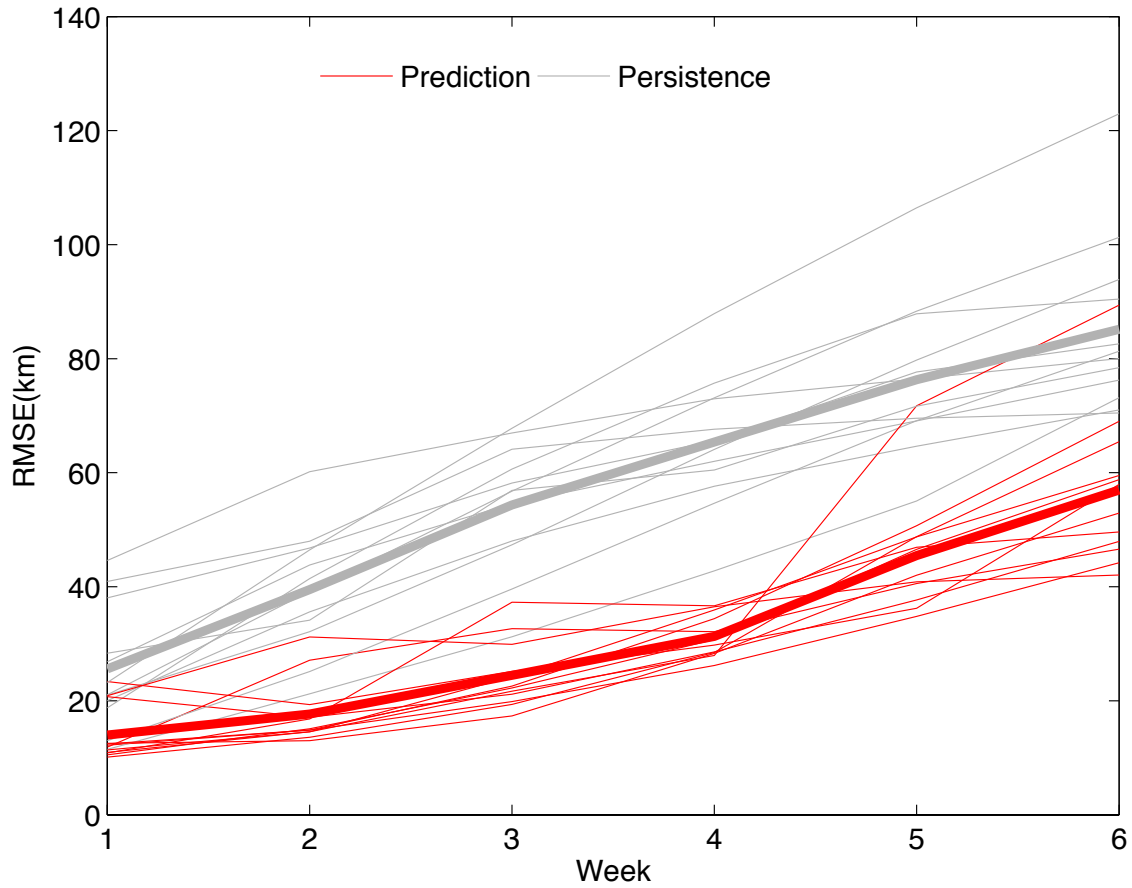
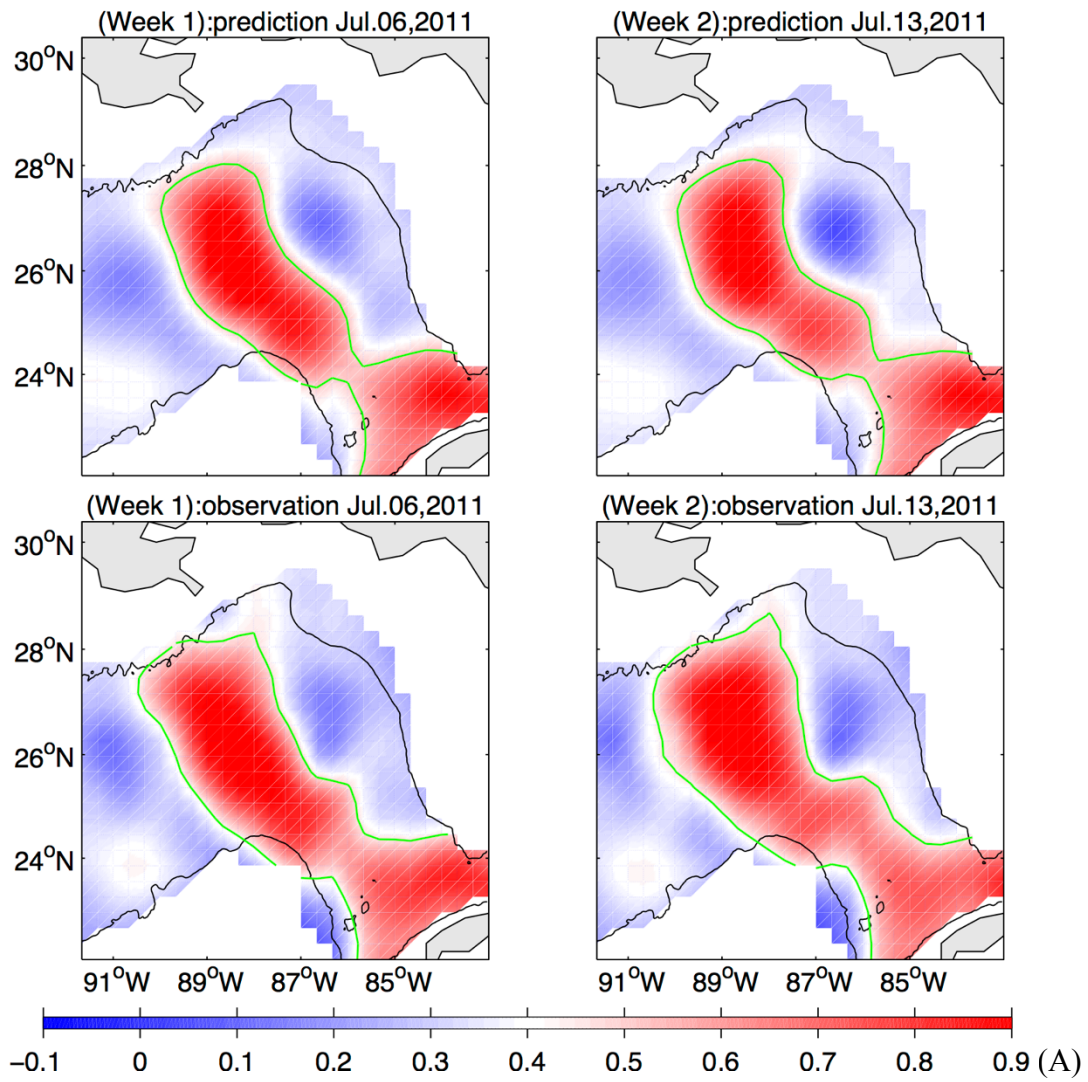
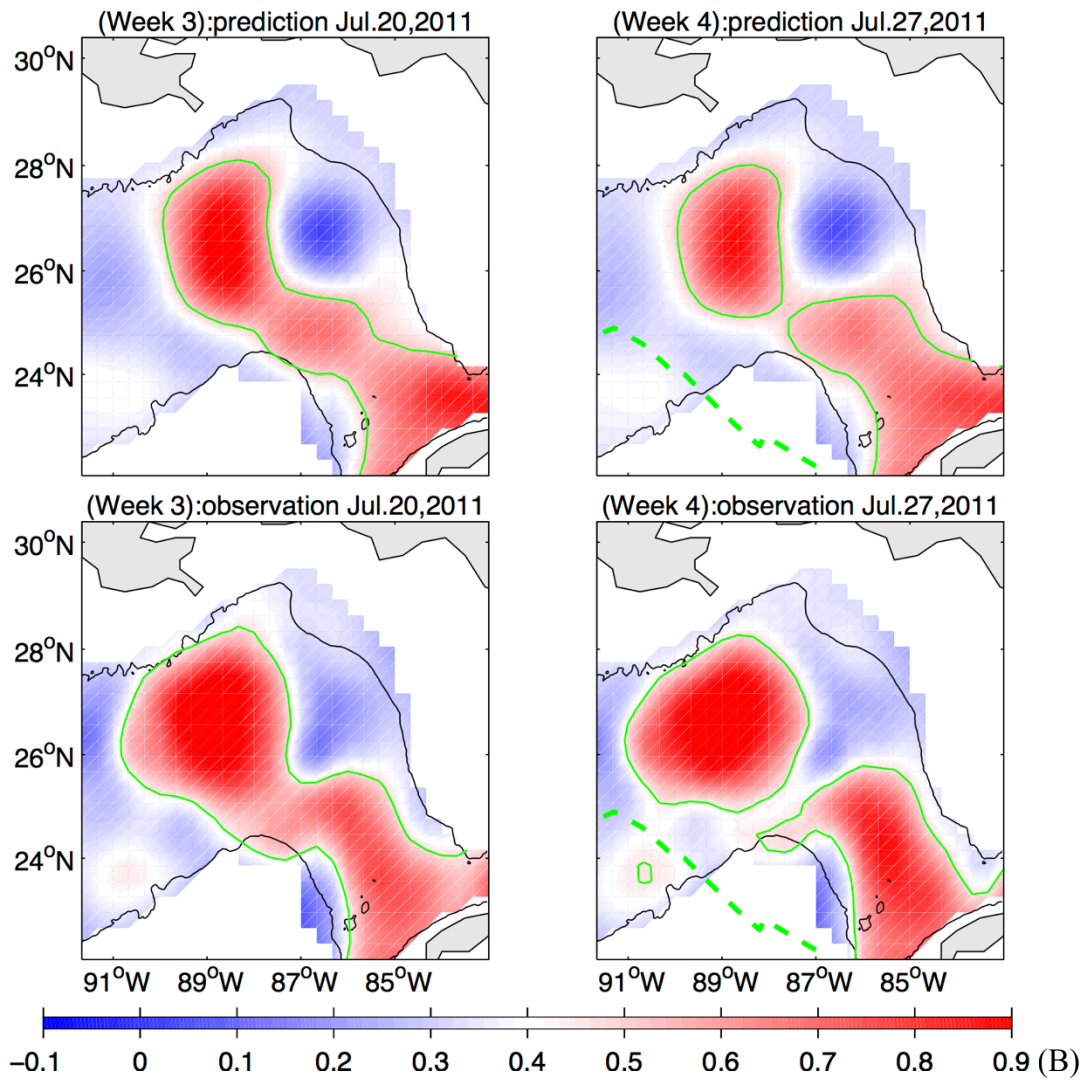


Figure 9. Averaged frontal position Root Mean Square Error (RMSE) for prediction (red) and persistence (grey). The sudden jumps in Figure 8 were excluded when the average was calculated. Thin lines are monthly means, and thick lines are means over the three-year period.





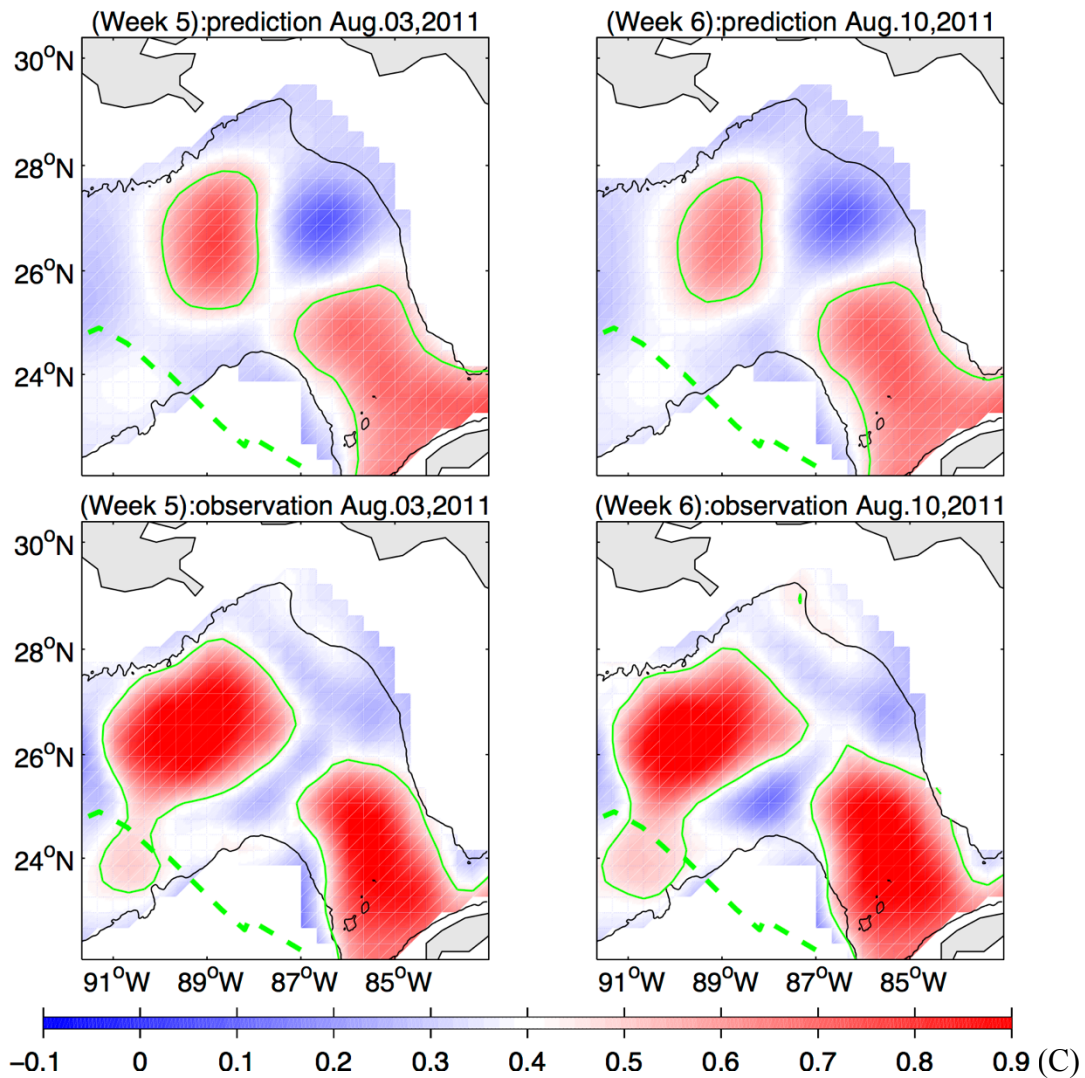


Figure 10. Comparison between forecasted and observed sea surface height in week 1-2 (panel A), week 3-4 (panel B), week 5-6 (panel C), representing a complete cycle of one Loop Current (LC) eddy shedding event. Black lines are 1000 m isobaths. Red areas are the LC and LC eddies. Green solid lines are 0.45 m contours for observation, and 0.51 m contours for prediction. Green dashed lines are the track of Tropical Storm Don during July 27-30, 2011.

**Chapter IV: Gulf Stream variability and a triggering mechanism of its  
large meander in the South Atlantic Bight**

Xiangming Zeng and Ruoying He

Department of Marine, Earth, and Atmospheric Sciences  
North Carolina State University, Raleigh, NC, USA 27695

*(Submitted to Journal of Geophysical Research: Oceans)*

## **Abstract**

The Gulf Stream (GS) variability has an important impact on coastal circulation, shelf ecosystem, and regional weather and climate systems. Here we focus on the variability of the GS south of Cape Hatteras in the South Atlantic Bight (SAB). Statistical analysis on the 21-year satellite altimetry data reveals that the GS path in the SAB has two patterns: weakly and strongly deflected. The strongly deflected pattern is more likely to occur in winter. Over the last two decades, the largest GS offshore meander occurred in November 2009-April 2010. Realistic ocean hindcast simulation and adjoint sensitivity analysis are used to investigate the triggering mechanisms for this extreme event. Our analyses show that a net increase of relative vorticity near the Charleston Bump was generated by strong interaction between increased GS velocity and local bathymetry, pushing the GS further offshore by virtue of conserving the potential vorticity. Quantitative vorticity analysis confirms this finding.

## **1. Introduction**

Originating near the equator, the North Atlantic Ocean's Western Boundary Current (WBC) flows into the Caribbean Sea, forms the Caribbean Current, which subsequently becomes the Loop Current once it enters the Gulf of Mexico. Further downstream the flow passes through the Florida Straits, becomes the Gulf Stream (GS), which moves through the South Atlantic Bight (SAB) and veers east into the open ocean off Cape Hatteras (Figure 1). Through this pathway, this WBC carries an enormous amount of volume and heat poleward, and plays a vital role in affecting both regional and global climate systems (Schmeits and Dijkstra, 2001; Frankignoul et al., 2001; Kwon et al., 2010).

While compared to other surface current systems, the WBC has a relatively stable main path, transport and speed, significant variability and instabilities do exist. Joyce and Zhang (2010) and Sanchez-Franks and Zhang (2015) found that the variability of the GS path is linked to the strength of the Atlantic Meridional Overturning Circulation (AMOC). Focusing on a region downstream of the GS separation point (Cape Hatteras), they suggested that a more southerly (northerly) GS path occurs when the AMOC is relatively strong (weak). Pérez-Hernández and Joyce (2014) performed an analysis of two decades of satellite altimetry data in the similar deep ocean region. The results revealed the bimodality of GS path variation and found that the GS shifts between 2010 and 2012 are the largest of last decade. More recently, several studies reported an extreme (~30%) decline of the AMOC strength in 2009-2010 based on ten years' (2004-2013) RAPID mooring observation (Ezer, 2015; Goddard et al., 2015; Srokosz and Bryden, 2015). Because of the linkage between AMOC strength and GS position, the large shifts of GS path in 2010-2012 may be related to the extreme decline of AMOC strength in 2009-2010.

It is known that the cross-shelf position of the GS also has a large impact on coastal circulation, shelf ecosystem, and regional weather systems. For instance, earlier studies (e.g., Bane and Dewar, 1988; Pérez-Hernández and Joyce, 2014; Gula et al., 2015) have shown that strong meanders and eddies are common features of the GS in the SAB and the variability of the GS position grows with the increasing water transport from the Florida Straits to open ocean (Schmitz and McCartney, 1993). Because the GS consists of high temperature water, variations in GS position can affect sea surface temperature distribution, which moderates air-sea heat and moisture fluxes (Minobe et al., 2010), especially in winter

(Bane and Osgood, 1989; Li et al., 2002; Joyce et al., 2009; Nelson and He, 2012; Nelson et al., 2014). Frontal eddies and water intrusion resulted from variations in the GS position can enhance water exchange, shelf break upwelling and deep-ocean nutrient delivery onto the shelf (Miller and Lee, 1995; Castelao, 2011), thereby influencing shelf-wide productivity and biomass (Lee et al., 1991; Signorini and McClain, 2007) as well as larval dispersal and distribution of fish populations (Werner et al., 1997; Epifanio and Garvine, 2001).

GS meanders along the continental margin in the SAB have been a long-standing research topic studied for decades. The first detailed observation was reported by Webster (1961), using measurements of surface salinity and velocity and water temperature in the top 200 m. Based on current meters and satellite imagery, Bane and Dewar (1988) suggested the seaward deflection of the GS near the Charleston Bump (Figure 2), a topographic feature located on the continental slope at 31.5°N offshore of Charleston, South Carolina, has a bimodal character of weakly and strongly deflected, and the transition between the two patterns occurs on an intermonthly timescale. Miller (1994) further supported this idea by analyzing twelve years of weekly GS position estimates and found a strong phase relationship between upstream water transport through the Florida Straits and the first principal component of GS position fluctuations. Furthermore, Schmeits and Dijkstra (2001) reasoned that the bimodal behavior of the GS is dynamically possible based on the dynamical system theory. By analyzing the energetics of numerical simulations, Miller and Lee (1995) concluded that the development of GS meanders and frontal eddies is controlled by a mixture of both baroclinic and barotropic instabilities of the mean flow. Xie et al. (2007) by using numerical sensitivity simulations with idealized topography showed that GS meanders are

the results of combined effect of isobathic curvature of SAB bathymetry and the Charleston Bump. More recently, Gula et al. (2015) quantified the role played by interactions of the GS with topographic features and the subsequent impact of nonlinear eddy-mean flow interactions through a high-resolution model.

In this study, we exam the variability of the GS in the SAB and its dynamics using long-term satellite observations, new analysis and numerical modeling methods. In section 2 we quantify the variation of the GS path in the SAB using two decades of satellite altimetry data and describe the large GS deflection identified in November 2009-April 2010. In section 3 we explore the triggering mechanism for this event using realistic numerical models and adjoint sensitivity analysis. Detailed flow field vorticity budget analysis is provided in section 4, followed with a conclusion and summary in section 5.

## **2. Gulf Stream path variation over the last two decades**

### **2.1 Gulf Stream path detection**

Different methods have been used in the past to track the GS path including the use of 15 °C isotherm at 200 m (Ganogadhyay et al., 1992; Joyce et al., 2000) and maximum sea surface height (SSH) gradient (Frankignoul et al., 2001; Peña-Molino and Joyce, 2008; Lillibridge III and Mariano, 2013). In this study, we applied the Canny edge detection method (Canny, 1986) on the 21-year AVISO gridded Absolute Dynamic Topography (ADT) to identify the location of the maximum gradient of the GS. The altimeter ADT products were produced by Ssalto/Duacs and distributed by Aviso, with support from Cnes (<http://www.aviso.altimeter.fr/duacs/>). The data are constructed with two simultaneously

operating altimeters, one in a 10-day exact repeat orbit (Topex/Poseidon, followed by Jason-1 and presently by Jason-2) and the other in a 35-day exact repeat orbit (ERS-1 followed by ERS-2 and presently by Envisat; Chelton et al., 2001). The data have  $1/4^\circ$  spatial and daily temporal resolutions (SSALTO/DUACS User Handbook, 2015). For quality control, only data from areas with water depth greater than 100 m were chosen for path detection (e.g., Yin et al., 2014; Zeng et al., 2015a, b)

The Canny edge detection method finds edges by looking for local maxima of the field gradient. The gradient is calculated using the derivative of a Gaussian filter. The method can automatically find two thresholds of gradient, to detect strong and weak edges, and includes the weak edges in the output only if they are connected to strong edges. This method is therefore more robust than other edge detection methods in detecting true edges (Mujumadr and Kumar, 2012). In the SAB, a strong ADT frontal gradient usually exists along the GS boundary. The resulting 21-year ADT edge locations are interpreted as the GS paths in the study region.

Figure 3 shows mean ADT (color shading), the detected GS mean path (solid black curve), corresponding envelope (dashed cyan curves), and one standard deviation lines (dashed black curves) from 1993 to 2013. The envelope represents the farthest (closest) location that the GS reached the open ocean (shelf) over the study duration. The mean path generally follows the 0.4 m contours of the mean ADT, with low ADT shoreward of the GS and high ADT seaward. From the topographic point of view, the mean path generally follows the 600 m isobaths from  $28^\circ\text{N}$  to  $34^\circ\text{N}$ , where the continental shelf is wide. From  $34^\circ\text{N}$  to Cape Hatteras, the shelf width decreases gradually, and the GS mean path moves to about the

2000 m isobaths, then separates from the continental shelf and veers east into the open ocean. The standard deviation is smaller compared to the envelope, meaning that large shifts of GS path occur infrequently. Both the standard deviation and the envelope increase from the Florida Straits to downstream of Cape Hatteras, especially around and downstream of the Charleston Bump.

To further quantify the variation of the Gulf Stream path, we calculated the GS offshore distance along five transects perpendicular to the mean path (Figure 3). Figure 4 show the GS position anomalies relative to the mean from 1993 to 2013. It is of interest to note that over the two decades, the largest Gulf Stream meander occurred in November 2009-April 2010. The offshore distance relative to its mean position increased from about 30 km at transect 1 to 90 km at transect 5.

## **2.2 Self-Organizing Map analysis**

With the derived GS location information, we also used the Self-Organizing Map (SOM) to cluster the GS paths in the SAB over the last 21 years.

The SOM is an effective method for feature extraction and classification. It is based on an unsupervised neural network and can map high-dimensional input data onto the elements of a regular, low-dimensional array (Kohonen, 2001). It has been demonstrated to be more powerful than the conventional empirical orthogonal function method for feature extractions, especially when the signal is highly nonlinear (Reusch et al., 2007; Liu et al., 2006a). The SOM is a mature method, and has been applied to identify patterns in ocean currents and sea surface temperature fields on the West Florida Shelf (Liu and Weisberg,

2005; Liu et al., 2006b & 2007), biogeochemical properties in the northern Adriatic Sea (Solidoro et al., 2007), current variability in the China Seas (Liu et al., 2008; Jin et al., 2010; Tsui and Wu, 2012; Yin et al., 2014), and SSH fields in the Gulf of Mexico (Zeng et al., 2015a).

The SOM analysis identified two patterns of the GS paths in the SAB (Fig 5a). Pattern 1 is located very close to the GS mean position, whereas Pattern 2 is further offshore between 31.5°N and 34°N. This result is consistent with earlier finding about the GS bimodal behavior in the SAB (Bane and Dewar, 1988; Miller, 1994; Schmeits and Dijkstra, 2001). Following the nomenclature used in Bane and Dewar (1988), we name Pattern 1 as the “weakly deflected” (red) pattern (P1), and Pattern 2 the “strongly deflected” (blue) pattern (P2).

To quantify the occurrence percentage of each pattern, the frequency of occurrence (FO) was calculated by summing the number of occurrences of each pattern divided by the total record length. Over two decades, the FO of the weakly deflected pattern was 74.1%, and the FO of the strongly deflected pattern was 25.9%. The latter smaller FO suggests the strong deflection (P2) is less frequent. Figure 5b shows the long-term monthly mean FO for each of the two patterns. As expected, the monthly FO of the strongly deflected pattern (P2) was about 1/3 of the FO of the weakly deflected pattern (P1) in all months. Both patterns show weak seasonality. The strongly deflected pattern (P2) has a higher monthly FO in winter and lower monthly FO in summer, opposite that of the weakly deflected pattern (P1). In other words, the GS offshore meanders are more likely to occur in winter than in summer.

To explore possible relationship between Florida Current (FC) transport and the GS offshore meanders, we obtained the daily transport time series ([www.aoml.noaa.gov/phod/floridacurrent/](http://www.aoml.noaa.gov/phod/floridacurrent/)) measured at the Florida Strait at about 26.5°N. Daily values of FC transport are available from 1982 to 1998 and 2000 to present, so we chose the same time periods when both FC transport measurements and ADT data were available to make the correlation calculation. At the monthly scale, the FO of P2 is generally negatively correlated ( $r=-0.81$ ) to FC transport (Figure 6a), and positively correlated with the monthly standard deviation (STD) of FC transport (Figure 6b). This interesting statistical result suggests that in winter (summer) months, the FC transport is lower (higher) with larger (smaller) STD, the corresponding FO of P2 is larger (smaller), thus the strongly deflected pattern is more (less) likely to occur. Influence of local wind forcing was also analyzed (not shown), but no significant relationship was found.

### **3. Triggering mechanism analysis**

Having discussed the long-term mean GS deflection patterns and their potential relationship with the Florida Current transport, we now switch the focus to the triggering mechanism for the extreme GS offshore deflection event that started in November 2009. The synoptic ocean state is the focus here, and we developed a realistic regional ocean hindcast model and its adjoint sensitivity tool for this analysis.

#### **3.1 Ocean model configuration and validation**

We applied the Regional Ocean Modeling System (ROMS), specifically, its nonlinear forward model and its tangent-linear adjoint module for this analysis. ROMS is terrain-

following coordinate, primitive equation model developed specifically for regional applications (Haidvogel et al., 2008). Its computational kernel uses high-order time stepping and advection schemes, and a carefully designed temporal averaging filter to guarantee exact conservation for tracers and momentum (Shchepetkin and McWilliams, 2005; Zhang et al., 2009).

The model domain shown in Figure 1 spans the whole northwest Atlantic with ~7 km horizontal grid spacing and 36 vertical layers. The bathymetry is generated using 1-minute gridded GEBCO data and smoothed with a linear programming procedure (Sikirić et al., 2009) to remove overly large gradients that may lead to unwanted numerical pressure gradient errors for the model. The model uses fourth-order centered advection with the generic length scale vertical mixing scheme (Warner et al., 2005) using k-kl mixing coefficients (corresponding to Mellor-Yamada Level 2.5).

At its only open boundary on the east, the model is configured to conserve volume with a free-surface Chapman condition, a Flather condition for the 2D momentum, and clamped conditions for the 3D momentum and tracers (Marchesiello et al., 2001; Powell et al., 2008; Broquet et al., 2009; Moore et al., 2009). Boundary values of ocean states are derived from the daily global HYCOM/NCODA product (<https://hycom.org>).

Surface forcing used in the ROMS simulation is derived from the European Center for Medium Range Weather Forecast (ECMWF) reanalysis product (<http://apps.ecmwf.int/datasets/data/interim-full-daily>) with 0.125 degree grid spacing every 3 hours. Air temperature, surface pressure, humidity, wind speed and direction, short- and

long-wave radiation, and precipitation from ECMWF are used to compute the ROMS surface momentum and buoyance forcing with the bulk flux formulation of Fairall et al. (1996).

The model is initialized with daily HYCOM data and ran from November 1 to 30, 2009, when the largest Gulf Stream offshore meander in the last two decades began to initiate. The first nine days are the model spin-up time. Model results starting on November 10 onward are used for model-data comparison and analysis.

To assess the model skill, numerous model-data comparisons were performed. Figure 7 for example shows the observed (blue) and simulated (red) daily sea level (normalized) at three stations along the SAB and water transport through the Florida Strait. The correlation coefficients between observations and simulations are all greater than 0.86 and the magnitude of simulated water transport also generally matches with the observed. These suggest the model realistically reproduces SAB circulation during this study period.

### **3.2 Adjoint sensitivity model**

A unique tool we used in this study is the adjoint sensitivity analysis. Given the simulated ocean state, the adjoint model allows one to go backward in time to track factors that were important for triggering the large GS offshore meanders in November 2009. The adjoint model has been widely studied in meteorological and oceanographic communities (Errico, 1997; Bennet, 1992 and 2002; Wunsch, 1996 and 2006). Recently, it has been developed and implemented into ocean models either for sensitivity studies or data assimilation purposes. Marotzke et al. (1999) described the construction of the adjoint MIT general circulation model with the automatic differentiation method. Chua and Bennett

(2001) developed a system for variational assimilation of data into ocean models based on the adjoint method. Along with the tangent linear and adjoint components, the data assimilation system of the Regional Ocean Modeling System (ROMS) has been described in a series of papers (Moore et al., 2004; Moore et al., 20011a, 2011b, and 2011c). Several studies have applied adjoint sensitivity to study ocean processes, such as the sensitivity studies of the Kuroshio Current (Ishikawa et al., 2004), meridional overturning circulation (Bugnion et al., 2006), the California Current (Moore et al., 2009; Veneziani et al., 2009), New York Bight circulation (Zhang et al., 2009), and the Loop Current in the Gulf of Mexico (Gopalakrishnan et al., 2013).

The basic ideas of the adjoint model are the first order Taylor approximation and Lagrange multiplier method. Following Moore et al. (2004) and Zhang et al. (2009), we consider the nonlinear ocean model (NLM), also known as the forward model:

$$\begin{cases} \frac{\partial \Phi(t)}{\partial t} = M(\Phi(t)) + \mathbf{F}(t) \\ \Phi(0) = \Phi_0 \\ \Phi(t)|_{\Omega} = \Phi_{\Omega}(t) \end{cases} \quad (1)$$

where  $\Phi(t)$  is a state vector of  $(u, v, T, S, \eta)$  representing the west-east velocity, south-north velocity, temperature, salinity, and sea level of all model grids at time  $t$ ;  $M$  is the nonlinear operator of the model;  $\mathbf{F}(t)$  is the external forcing at time  $t$ ;  $\Phi_0$  are the initial conditions;  $\Phi_{\Omega}(t)$  are the boundary conditions along boundary  $\Omega$ . Suppose  $\Phi_c$  is a certain solution of Eq. (1), and we introduce small perturbations  $\phi_0 = \delta\Phi_0$ ,  $\phi_{\Omega}(t) = \delta\Phi_{\Omega}(t)$ , and  $\mathbf{f}(t) = \delta\mathbf{F}(t)$  to the initial conditions, boundary conditions, and external forcing, respectively. The corresponding perturbations of the solution  $\Phi_c$  can be expressed as  $\phi = \Phi - \Phi_c$ . Then we

can get the perturbation by considering the difference between original and perturbed equations:

$$\begin{cases} \frac{\partial \boldsymbol{\phi}(t)}{\partial t} = M(\boldsymbol{\Phi}(t)) - M(\boldsymbol{\Phi}_c(t)) + \mathbf{f}(t) \\ \boldsymbol{\phi}(0) = \boldsymbol{\phi}_0 \\ \boldsymbol{\phi}(t)|_{\Omega} = \boldsymbol{\phi}_{\Omega}(t) \end{cases} \quad (2)$$

Using the first order Taylor approximation, we have

$$M(\boldsymbol{\Phi}(t)) = M(\boldsymbol{\Phi}_c(t)) + \left. \frac{\partial M}{\partial \boldsymbol{\Phi}} \right|_{\boldsymbol{\Phi}_c} (\boldsymbol{\Phi} - \boldsymbol{\Phi}_c) \quad (3)$$

Plug Eq. (3) into Eq. (2) and considering  $\boldsymbol{\phi} = \boldsymbol{\Phi} - \boldsymbol{\Phi}_c$ , we have the tangent linear model (TLM):

$$\begin{cases} \frac{\partial \boldsymbol{\phi}(t)}{\partial t} = \left. \frac{\partial M}{\partial \boldsymbol{\Phi}} \right|_{\boldsymbol{\Phi}_c} (\boldsymbol{\Phi} - \boldsymbol{\Phi}_c) + \mathbf{f}(t) = \mathbf{C}\boldsymbol{\phi} + \mathbf{f}(t) \\ \boldsymbol{\phi}(0) = \boldsymbol{\phi}_0 \\ \boldsymbol{\phi}(t)|_{\Omega} = \boldsymbol{\phi}_{\Omega}(t) \end{cases} \quad (4)$$

where  $\mathbf{C}$  is the Jacobian matrix. After it is discretized in space and time, the TLM yields a system of linear equations (Zhang et al., 2009):

$$\mathbf{A}\boldsymbol{\phi} = \mathbf{b} \quad (5)$$

where  $\mathbf{A}$  is the corresponding coefficient matrix, and  $\mathbf{b}$  is a vector consisting of the perturbations of boundary conditions, initial conditions, and external forcing terms. That is, if we let vectors  $\mathbf{r}$  and  $\mathbf{r}_c$  be the boundary conditions, initial conditions, and external forcing terms corresponding to the solution  $\boldsymbol{\Phi}$  and  $\boldsymbol{\Phi}_c$ , respectively, then  $\mathbf{b} = \mathbf{r} - \mathbf{r}_c$ .

We can define an index scalar function  $J(\boldsymbol{\Phi})$  to represent the model state we want to explore the sensitivity. Because  $\boldsymbol{\phi} = \boldsymbol{\Phi} - \boldsymbol{\Phi}_c$ , we have  $J(\boldsymbol{\Phi}) = J(\boldsymbol{\phi} + \boldsymbol{\Phi}_c) = G(\boldsymbol{\phi})$ .

Applying the Lagrange multiplier method (Bertsekas, 1982) to the function  $G(\boldsymbol{\phi})$ , we get a cost function:

$$L = G(\boldsymbol{\phi}) + \boldsymbol{\lambda}^T (\mathbf{A}\boldsymbol{\phi} - \mathbf{b}) \quad (6)$$

where  $\boldsymbol{\lambda}$  is the Lagrange multiplier vector, and  $T$  represents transpose. Note that  $L$  has the same minimum as  $G(\boldsymbol{\phi})$  subject to Eq. (5). Let  $\mathbf{g}(\boldsymbol{\phi}) = \mathbf{A}\boldsymbol{\phi} - \mathbf{b}$ . According to Ito and Kunisch (2008), we have

$$\frac{\partial G}{\partial \boldsymbol{\phi}} + \boldsymbol{\lambda}^T \frac{\partial \mathbf{g}}{\partial \boldsymbol{\phi}} = 0 \quad (7)$$

which can also be derived by setting  $\frac{\partial L}{\partial \boldsymbol{\phi}} = 0$  (Bennett, 2002; Zhang et al., 2009). After taking the transpose of both sides of (7), and considering  $\frac{\partial G}{\partial \boldsymbol{\phi}} = \frac{\partial J}{\partial(\boldsymbol{\Phi} - \boldsymbol{\Phi}_c)} = \frac{\partial J}{\partial \boldsymbol{\Phi}}$ , we can get the adjoint model (ADM):

$$-\mathbf{A}^T \boldsymbol{\lambda} = \left(\frac{\partial J}{\partial \boldsymbol{\Phi}}\right)^T \quad (8)$$

$\boldsymbol{\lambda}$  can be considered a sensitivity measure of a certain ocean state  $J$  to initial conditions, boundary conditions, and external forcing fields  $\mathbf{r}$ . Considering  $\mathbf{g}(\boldsymbol{\phi}) = \mathbf{A}\boldsymbol{\phi} - \mathbf{b}$ ,  $\mathbf{b} = \mathbf{r} - \mathbf{r}_c$ ,  $\boldsymbol{\phi} = \boldsymbol{\Phi} - \boldsymbol{\Phi}_c$ , and the chain rule, we have

$$\left(\frac{\partial J}{\partial \mathbf{r}}\right)^T = \left(\frac{\partial J}{\partial \boldsymbol{\Phi}} \frac{\partial \boldsymbol{\Phi}}{\partial \mathbf{r}}\right)^T = \left(\frac{\partial G}{\partial \boldsymbol{\phi}} \frac{\partial \boldsymbol{\phi}}{\partial \mathbf{r}}\right)^T = \left(-\boldsymbol{\lambda}^T \frac{\partial \mathbf{g}}{\partial \boldsymbol{\phi}} \frac{\partial \boldsymbol{\phi}}{\partial \mathbf{r}}\right)^T = -\left(\boldsymbol{\lambda}^T \frac{\partial \mathbf{g}}{\partial \mathbf{b}}\right)^T = -(-\mathbf{I}\boldsymbol{\lambda}^T)^T = \boldsymbol{\lambda} \quad (9)$$

where  $\mathbf{I}$  is the identity matrix. The adjoint sensitivity can measure the real changes of certain ocean states due to the perturbation of certain factors such as velocity. However, the units of  $\frac{\partial J}{\partial \mathbf{r}}$  vary across components, complicating the direct comparison of the sensitivities. Following

Moore et al. (2009), we can consider the changes  $\Delta J_i = \Delta \mathbf{r}_i \frac{\partial J}{\partial \mathbf{r}_i}$  that would result from

perturbations  $\Delta \mathbf{r}$  at each grid point  $i$  within the target region and time. Standard deviation of each element at grid point  $i$  is typically chosen as  $\Delta \mathbf{r}_i$ . Therefore, the direct comparison of  $\Delta J_i$  arising from perturbations in each component of  $\mathbf{r}$  provides an immediate quantitative appreciation of the sensitivity of  $J$  to perturbations with amplitudes typical of those encountered in the real ocean. If  $J$  represents the mismatch between the NLM state and observations, minimizing  $J$  is one method of doing data assimilation. If  $J$  is a measure of some model state of NLM, the adjoint sensitivity identifies locations and variables that are important to this feature (Zhang et al., 2009).

### 3.3 Forward model results

Figure 8 shows the simulated surface velocity and relative vorticity (normalized by the Coriolis parameter) from November 17 to 26, 2009, in three-day intervals. As shown by simulation, the GS speed is at a maximum along the continental shelf in this region. Due to the strong velocity shear along edges of the GS, positive relative vorticity occurs shoreward, and negative relative vorticity exists seaward. From the Florida Straits to the Charleston Bump, the GS path generally follows the 600 m isobaths. As the width of the continental shelf decreases, the GS moves further offshore to the 2000 m isobaths. From November 17 to 26, a large meander developed downstream of the Charleston Bump, which moved the GS position (near the black box in Figure 8) further offshore. Numerous eddies (both anticyclones and cyclones) were present seaward of the GS, visible in both the velocity and relative vorticity fields.

As shown by the simulation (Figure 8), both the Florida Current (FC), which flows through the Florida Straits, and the Antilles Current (AC), which passes northeast of Abaco Island, Bahamas contribute to the formation of the GS. The validity of the AC remains questionable due to its discontinuous nature and weak dynamic signal (Rowe et al., 2013). The hydrographic study of Gnu and Watts (1982) found that the AC acts more as an eddy field rather than as a continuous jet. Lee et al. (1996) concluded that the AC serves to balance the interior Sverdrup circulation not accounted for by the FC and that it is not a continuous flow along the Bahamas and Antilles island chain. In our study duration, however, we can see a clear flow path of the AC from Abaco Island to the SAB in the simulated surface velocity fields (Figure 8 a, b and c). Even though the surface path of the AC into the GS has less distinct surface structure on November 26 (Figure 8d), the AC beneath the surface consistently contributes to the GS (not shown). The estimates of AC transport vary from different studies. Lee et al. (1996) presented a range from 2 to 7 Sv (net transport) with a mean northward flow of  $5\pm 2$  Sv at  $27^\circ\text{N}$ . In contrast, Schmitz and McCartney (1993) reported a much higher value of 12 Sv. Our simulated AC transport (Figure 9) shows a similar estimation to that of Schmitz and McCartney (1993). Although we note that our transect for AC transport calculation is different from Lee et al. (1996)'s, but similar to that of Schmitz and McCartney (1993).

The GS water transport calculated immediately upstream of the Charleston Bump (Figure 9) is  $\sim 40$  Sv. Due to the adjustment of the AC on the continental shelf before joining the GS, not all AC water through the Abaco transect goes into the GS. The transport magnitude indicates that the FC is the major contributor of the GS in the SAB, which

accounts for  $\sim 75\%$  ( $\sim 30$  Sv) of water transport. That leaves  $\sim 25\%$  ( $\sim 10$  Sv) coming from the AC. We calculated that  $\sim 67\%$  of AC water goes into the GS, while  $\sim 23\%$  recirculates to the deep ocean. These estimates are based on a one-month simulation. Over a longer time scale, the results may differ.

Another interesting pattern as shown in Figure 9 is the sudden drop of water transport within four days at all three transects. For the GS, water transport drops  $\sim 5$  Sv from November 13<sup>th</sup>, and reaches the lowest value in the study period on the 16<sup>th</sup>. For the FC, the drop ( $\sim 8$  Sv) happens from November 12<sup>th</sup> to 15<sup>th</sup>. For the AC, the drop ( $\sim 4$  Sv) also occurs from November 12<sup>th</sup> to 15<sup>th</sup>. Because the FC speed ( $\sim 1.5$  m/s) is much greater than that of the AC ( $\sim 0.3$  m/s), the water transport signals at the Florida Straits and Abaco transects should propagate to the transect upstream of Charleston Bump at different times. Therefore, the  $\sim 5$  Sv drop of GS water transport from November 13<sup>th</sup> to 16<sup>th</sup> approximately corresponds to the drop of FC transport ( $\sim 8$  Sv) from November 12<sup>th</sup> to 15<sup>th</sup> and the slight increase of AC transport before November 12<sup>th</sup>. In this way, the water transport values can generally be consistent. In the following section, we will show the influence of the sudden transport recovery following the sudden transport drop on the formation of large Gulf Stream offshore meanders.

### **3.4 Validity of tangent linear assumption and index function definition**

As noted in 3.1, adjoint sensitivity analysis is based on the validity of the tangent linear assumption. Before performing adjoint sensitivity analysis, the validity of the tangent linearization should be verified. This is done by comparing fifty random perturbation runs with the corresponding TLM solutions.

From a five-year forward simulation, we randomly select an ocean state perturbation ( $dx$ ) relative to its mean, and set  $dx$  as the initial value for the TLM ( $g$ ). Assuming  $x_0$  is the initial field for the original forward model ( $f$ ), we can then compare the difference of forward model ( $f(x_0 + dx, t) - f(x_0, t)$ ) with the TLM solutions ( $g(dx, t)$ ), and choose the proper time scale indicated by the correlation coefficients. Fifty perturbation (i.e., SSH~0.2 m, velocity~0.4 m/s) runs are implemented with dynamically relevant amplitudes. As shown in Figure 10, correlation coefficients gradually decrease as the time window increases. The time scale of linearization for SSH is longer than that of velocity. We chose the time scale for valid tangent linear assumption to be 10 days, when the mean correlation coefficient of the velocity comparisons is around 0.6.

To use the adjoint model, an index function  $J$  (also called cost function or penalty function in other references) must be defined as a function of model output variables. Similar to Gopalakrishnan et al. (2013), we define the index function as the negative daily mean SSH in the black box of Figure 3 to represent the variation of GS position adjacent to transect 2 (Figure 3). That is,

$$J = -\frac{1}{(t_2 - t_1)A} \int_{t_1}^{t_2} \int_A \eta dA dt \quad (10)$$

where  $\eta$  is SSH,  $A$  is the area, and the time range is  $t_1$  to  $t_2$  (one day for this case).

The model simulation shows that the mean SSH within the black control box is very well inversely correlated with the GS position along transect 2 (Figure 11). That is, when the GS moves seaward, the SSH inside the control box decreases, and vice versa. The correlation

coefficient of the two variables is highly significant ( $r=-0.9$ ) during the study period, indicating the validity of choosing this index function to represent GS path variation.

Because the tangent linear assumption is valid for ten days (shown above), a ten-day window from November 17<sup>th</sup> to 26<sup>th</sup> was selected for the adjoint sensitivity analysis (shown by the dashed rectangle in Figure 11). During this time period, the GS moved seaward, while mean SSH within the control area decreased. Using the adjoint model, we can go backward in time and diagnose what processes triggered the GS offshore motion on November 26<sup>th</sup>.

### 3.5 Adjoint sensitivity analysis

Figure 12 shows the adjoint sensitivity of index function  $J$  to the depth-averaged velocity field  $(\frac{\partial J}{\partial u}, \frac{\partial J}{\partial v})$  going backward in time from November 26<sup>th</sup> to 17<sup>th</sup>, every three days. Following Moore et al. (2009), the sensitivity is plotted as a velocity vector field. Physically, such an adjoint sensitivity can be considered as a scaled barotropic velocity perturbation (Moore et al., 2009), which caused the large GS seaward motion on November 26<sup>th</sup>, 2009. On November 26<sup>th</sup>, the sensitivity area was around the index-defining black box (Figure 12a) in a form of a cyclonic velocity perturbation. This cyclonic perturbation is positive, indicating a positive relative vorticity perturbation is present at that time point. Going backward in time, the sensitivity region gradually extends to the north and south largely along the isobaths (Figure 12d). The cyclonic feature on November 26<sup>th</sup> can be further traced back to the cyclonic perturbation around the Charleston Bump on November 17<sup>th</sup>, which can be subsequently traced back to the Florida Strait. This is most evident in the northward sensitivity vector fields along the GS main path, indicating a positive velocity

perturbation (i.e., increase of GS velocity) that started from November 15<sup>th</sup> can lead to an increase of index function  $J$  (Figure 9) over the study period. Because the GS flows northward through the Florida Straits, the increase of water transport through the Florida Straits caused the GS velocity enhancement, thus a positive velocity perturbation reflected in the sensitivity field. This increased GS velocity interacts with the topographic feature near the Charleston Bump, producing a cyclonic vorticity perturbation in the area.

The sensitivity seaward of the 1000 m isobaths from 32°N to 36°N is also noticeable, suggesting a possible interaction of the GS with deep boundary currents or eddies may also contribute to the perturbation of  $J$ . Seaward of the 600 m isobaths from 27°N to 30°N, the decreasing velocity perturbation (indicated by the southward vector field) corresponds to the transport decline of the Antilles Current (AC) starting from November 12<sup>th</sup>, 2009 (Figure 9). The sensitivity of index function  $J$  to the depth-averaged velocity field is relatively small in other regions (Figure 12d).

Figure 13 provides a conceptual schematic to illustrate how the increased velocity field interacts with the topography to cause the GS move seaward. Assume the normal state of the stream velocity field is largely symmetric due to velocity shear and balance (Figure 13a). Positive relative vorticity exists shoreward, and negative relative vorticity occurs seaward of the stream. An increased water transport would increase stream velocity while maintaining the shear balance (Figure 13b). However, the symmetric balance breaks down with the presence of the topographic Bump, (Figure 13c). The blocking effect of the Bump leads to an enhancement of shoreward velocity shear and therefore an increase of the positive

relative vorticity compared to those in the seaward. Therefore, a stream has an overall net increase of positive relative vorticity.

Now consider the the first order principle of potential vorticity conservation:  $PV = \frac{f+\zeta}{h} = \text{constant}$ , where  $f$  is the Coriolis parameter,  $\zeta$  is relative vorticity, and  $h$  is water depth. Over the small geographic region being considered,  $f$  changes little. If net relative vorticity  $\zeta$  associated with the flow increases, water depth  $h$  must increase in order to conserve potential vorticity. That implies that the stream must move further offshore to the deep water region.

#### 4. Barotropic vorticity budget

To further verify the previous analysis, we calculated the barotropic vorticity budget in the SAB following Marchesiello et al. (2003) and Gula et al. (2015). The full barotropic vorticity balance equation can be obtained by integrating the momentum equations in the vertical and cross-differentiating them (Gula et al., 2015):

$$\underbrace{\frac{\partial \Omega}{\partial t}}_{\text{Tendency}} = \underbrace{-\nabla \cdot (f\bar{\mathbf{u}})}_{\text{BETA}} + \underbrace{\frac{\mathbf{J}(P_b, h)}{\rho_0}}_{\text{BPT}} + \underbrace{\mathbf{k} \cdot \nabla \times \frac{\boldsymbol{\tau}^{\text{wind}}}{\rho_0}}_{\text{WSC}} - \underbrace{\mathbf{k} \cdot \nabla \times \frac{\boldsymbol{\tau}^{\text{bottom}}}{\rho_0}}_{\text{BDC}} + \underbrace{D_\Sigma}_{\text{DIFF}} - \underbrace{A_\Sigma}_{\text{ADV}} \quad (11)$$

where the barotropic vorticity is defined as vorticity of the vertically integrated velocities  $\Omega = \frac{\partial \bar{v}}{\partial x} - \frac{\partial \bar{u}}{\partial y}$  with  $(u, v)$  as the  $(x, y)$  components of the horizontal flow, the overbar denotes a vertically integrated quantity,  $\mathbf{J}(P_b, h)$  is the Jacobian matrix of bottom pressure  $P_b$  and water depth  $h$ ,  $\boldsymbol{\tau}$  is wind or bottom stress, and  $\rho_0$  is the reference density. The terms on the r.h.s of Eq. (11) are planetary vorticity advection (BETA), bottom pressure torque (BPT), wind stress curl (WSC), bottom drag curl (BDC), horizontal diffusion (DIFF), and nonlinear

advection (ADV). As a sanity check, the sum of BETA, BPT, and ADV nearly equals to the vorticity tendency term, within small numerical residual range (not shown).

Temporal mean values of dominant terms (tendency, BETA, BPT, and ADV) in Eq. (11) were calculated from November 17 to 26, 2009 (Figure 14). Along the path of the GS, large positive vorticity tendency occurred shoreward of the Charleston Bump and at the right bottom corner of the black box in Figure 14, which indicates an increase in barotropic vorticity. This is consistent with the previous analysis that increased relative vorticity forces the GS move seaward due to conserving potential vorticity. The BETA term is noisy and shows no particular pattern. The BPT term shows a positive contribution to the vorticity variation downstream of the Charleston Bump, indicating that the topography interacts with the velocity fields to provide positive vorticity. The ADV term, being another important term in the vorticity budget, showing a negative contribution to barotropic vorticity downstream of the Charleston Bump over the ten-day period.

To further explore the variation of different terms in Eq. (11), we calculated the spatial mean of each term in the area around the Charleston Bump (green box in Figure 14) from November 17<sup>th</sup> to 26<sup>th</sup>, 2009 (Figure 15). The green box indicates the area that is important for the large GS offshore meander in this study. Similar to previous analyses, the dominant terms are the tendency, BETA, BPT, and ADV. Over the ten days, the tendency term is mostly positive, which means the vorticity overall increases. Because the region is small, the BETA term changes little. The BPT term makes a positive contribution to the change of barotropic vorticity. But it is the ADV term that dominates the variation of the vorticity tendency term. The variation of the vorticity near the Charleston Bump during this

time period generally corresponds to the increased water transport through the Florida Straits from November 14<sup>th</sup> to 23<sup>rd</sup> (Figure 9).

## **5. Summary**

In this study, both the long-term and synoptic variability of the Gulf Stream path in the South Atlantic Bight and corresponding mechanisms are analyzed based on satellite altimetry observations, advanced numerical simulations, and vorticity budget analysis.

The Gulf Stream path was quantified using two decades of satellite altimeter data and the Self-Organizing Map (SOM). The variability of the Gulf Stream path generally increases from the Florida Straits to open ocean, supporting previous study by Schmitz and McCartney (1993). Consistent with earlier study by Bane and Dewar (1988), the weakly and strongly deflected patterns of the Gulf Stream were also confirmed in our analysis. Overall, the weakly deflected pattern occurs more frequently than the strongly deflected pattern. As revealed by the SOM analysis, the strongly deflected pattern is more likely to occur in winter when the water transport through the Florida Straits is relatively low but with larger variability. This finding is consistent with Miller (1994)'s analysis about the Florida Current transport and the Gulf Stream path variation.

Over the last two decades, the largest Gulf Stream offshore meanders occurred in November 2009-April 2010. We focused on the beginning stage (November 2009) of the extreme meander event. Triggering mechanisms of this Gulf Stream offshore meanders were explored using a regional implementation of ROMS forward model and its adjoint sensitivity analysis. The forward ocean model was skillful in reproducing the regional circulation in

November 2009. By comparing water transport through three different transects (Figure 9), we found that the Gulf Stream transport upstream of the Charleston Bump was  $\sim 40$  Sv in November 2009, among that  $\sim 75\%$  ( $\sim 30$  Sv) originated from Florida Straits and  $\sim 25\%$  ( $\sim 10$  Sv) came from the Antilles Current. A ten-day window (November 17<sup>th</sup>-26<sup>th</sup>, 2009) was chosen for the backward in time adjoint sensitivity analysis based on the validity of tangent linear assumption. The sensitivity of Gulf Stream offshore meanders to the depth-averaged velocity field showed an increase of velocity in the Gulf Stream, which interacted with the local topography near the Charleston Bump to generate an asymmetric velocity shear. As a result, there was a net increase of positive relative vorticity, indicated by the cyclonic velocity perturbation around the Bump (Figure 11). The increased relative vorticity forced the Gulf Stream to move further offshore to conserve potential vorticity. The adjoint sensitivity analysis showed this process corresponded to a Florida current transport increase starting from November 15<sup>th</sup>, 2009.

Barotropic vorticity budget analysis further confirmed these findings. The dominant terms in the barotropic vorticity budget are the planetary vorticity advection, bottom pressure torque, and the nonlinear advection. During the study time period, the vorticity tendency near the Charleston Bump, mostly remains positive, indicating an overall increase in relative vorticity. Its variation is mostly dominated by the nonlinear advection.

## **Acknowledgement**

The authors thank Dr. A. M. Moore from University of California, Santa Cruz, Dr. J. Bane and Dr. H. Seim of University of North Carolina, Chapel Hill, and Dr. W. G. Zhang and Dr. Y. Li from Woods Hole Oceanographic Institution for their helpful discussions of this study. Research supported provided by NSF grants: OCE 1029841, OCE1559178; NOAA grants: NA11NOS0120033, NA14NMF4540061; NASA grants: NNX12AP84G, NNX13AD80G, NNX14AO73G are greatly appreciated.

## References

- Bane, J. M., and W. K. Dewar (1988), Gulf Stream bimodality and variability downstream of the Charleston bump, *J. Geophys. Res.*, *93*(C6), 6695–6710, doi:10.1029/JC093iC06p06695.
- Bane, J. M., and K. E. Osgood (1989), Wintertime air-sea interaction processes across the Gulf Stream, *J. Geophys. Res.*, *94*(C8), 10755–10772, doi:10.1029/JC094iC08p10755.
- Bennett, A. F. (1992), *Inverse Methods in Physical Oceanography*, Cambridge University Press, Cambridge.
- Bennett, A. F. (2002), *Inverse Modeling of the Ocean and Atmosphere*, Cambridge University Press.
- Broquet, G., C. A. Edwards, A. M. Moore, B. S. Powell, M. Veneziani, and J. D. Doyle (2009), Application of 4D-Variational data assimilation to the California Current System, *Dynamics of Atmospheres and Oceans*, *48*(1–3), 69–92, doi:10.1016/j.dynatmoce.2009.03.001.
- Bugnion, V., C. Hill, and P. H. Stone (2006), An Adjoint Analysis of the Meridional Overturning Circulation in an Ocean Model, *J. Climate*, *19*(15), 3732–3750, doi:10.1175/JCLI3787.1.
- Canny, J. (1986), A Computational Approach to Edge Detection, *IEEE Transactions on Pattern Analysis and Machine Intelligence*, *PAMI-8*(6), 679–698, doi:10.1109/TPAMI.1986.4767851.
- Castelao, R. (2011), Intrusions of Gulf Stream waters onto the South Atlantic Bight shelf, *J. Geophys. Res.*, *116*(C10), C10011, doi:10.1029/2011JC007178.
- Chelton, D. B., M. G. Schlax, and R. M. Samelson (2011), Global observations of nonlinear mesoscale eddies, *Progress in Oceanography*, *91*(2), 167–216, doi:10.1016/j.pocean.2011.01.002.
- Chua, B. S., and A. F. Bennett (2001), An inverse ocean modeling system, *Ocean Modelling*, *3*(3–4), 137–165, doi:10.1016/S1463-5003(01)00006-3.

- Epifanio, C. E., and R. W. Garvine (2001), Larval Transport on the Atlantic Continental Shelf of North America: a Review, *Estuarine, Coastal and Shelf Science*, 52(1), 51–77, doi:10.1006/ecss.2000.0727.
- Errico, R. M. (1997), What Is an Adjoint Model?, *Bull. Amer. Meteor. Soc.*, 78(11), 2577–2591, doi:10.1175/1520-0477(1997)078<2577:WIAAM>2.0.CO;2.
- Ezer, T. (2015), Detecting changes in the transport of the Gulf Stream and the Atlantic overturning circulation from coastal sea level data: The extreme decline in 2009–2010 and estimated variations for 1935–2012, *Global and Planetary Change*, 129, 23–36, doi:10.1016/j.gloplacha.2015.03.002.
- Fairall, C. W., E. F. Bradley, D. P. Rogers, J. B. Edson, and G. S. Young (1996), Bulk parameterization of air-sea fluxes for Tropical Ocean-Global Atmosphere Coupled-Ocean Atmosphere Response Experiment, *J. Geophys. Res.*, 101(C2), 3747–3764, doi:10.1029/95JC03205.
- Frankignoul, C., G. de Coëtlogon, T. M. Joyce, and S. Dong (2001), Gulf Stream Variability and Ocean–Atmosphere Interactions, *Journal of Physical Oceanography*, 31(12), 3516.
- Goddard, P. B., J. Yin, S. M. Griffies, and S. Zhang (2015), An extreme event of sea-level rise along the Northeast coast of North America in 2009–2010, *Nat Commun*, 6, doi:10.1038/ncomms7346.
- Gopalakrishnan, G., B. D. Cornuelle, and I. Hoteit (2013), Adjoint sensitivity studies of loop current and eddy shedding in the Gulf of Mexico, *Journal of Geophysical Research: Oceans*, n/a–n/a, doi:10.1002/jgrc.20240.
- Gula, J., M. J. Molemaker, and J. C. McWilliams (2015), Gulf Stream Dynamics along the Southeastern U.S. Seaboard, *J. Phys. Oceanogr.*, 45(3), 690–715, doi:10.1175/JPO-D-14-0154.1.
- Haidvogel, D. B. et al. (2008), Ocean forecasting in terrain-following coordinates: Formulation and skill assessment of the Regional Ocean Modeling System, *Journal of Computational Physics*, 227(7), 3595–3624, doi:10.1016/j.jcp.2007.06.016.
- Ishikawa, Y., T. Awaji, N. Komori, and T. Toyoda (2004), Application of Sensitivity Analysis Using an Adjoint Model for Short-Range Forecasts of the Kuroshio Path South of Japan, *Journal of Oceanography*, 60(2), 293–301, doi:10.1023/B:JOCE.0000038335.50080.ff.

- Jin, B., G. Wang, Y. Liu, and R. Zhang (2010), Interaction between the East China Sea Kuroshio and the Ryukyu Current as revealed by the self-organizing map, *Journal of Geophysical Research: Oceans*, 115(C12), n/a–n/a, doi:10.1029/2010JC006437.
- Joyce, T. M., and R. Zhang (2010), On the Path of the Gulf Stream and the Atlantic Meridional Overturning Circulation, *J. Climate*, 23(11), 3146–3154, doi:10.1175/2010JCLI3310.1.
- Joyce, T. M., C. Deser, and M. A. Spall (2000), The Relation between Decadal Variability of Subtropical Mode Water and the North Atlantic Oscillation\*, *J. Climate*, 13(14), 2550–2569, doi:10.1175/1520-0442(2000)013<2550:TRBDVO>2.0.CO;2.
- Joyce, T. M., Y.-O. Kwon, and L. Yu (2009), On the Relationship between Synoptic Wintertime Atmospheric Variability and Path Shifts in the Gulf Stream and the Kuroshio Extension, *J. Climate*, 22(12), 3177–3192, doi:10.1175/2008JCLI2690.1.
- Gunn, J.T. and Watts D.R. (1982), On the currents and water masses north of the Antilles/Bahamas Arc, *Journal of Marine Research*, 40, 1-48.
- Kohonen, T. (2001), *Self-Organizing Maps*, Springer Series in Information Sciences, Springer Berlin Heidelberg, Berlin, Heidelberg.
- Kwon, Y.-O., M. A. Alexander, N. A. Bond, C. Frankignoul, H. Nakamura, B. Qiu, and L. A. Thompson (2010), Role of the Gulf Stream and Kuroshio–Oyashio Systems in Large-Scale Atmosphere–Ocean Interaction: A Review, *J. Climate*, 23(12), 3249–3281, doi:10.1175/2010JCLI3343.1.
- Lee, T. N., J. A. Yoder, and L. P. Atkinson (1991), Gulf Stream frontal eddy influence on productivity of the southeast U.S. continental shelf, *J. Geophys. Res.*, 96(C12), 22191–22205, doi:10.1029/91JC02450.
- Lee, T. N., W. E. Johns, R. J. Zantopp, and E. R. Fillenbaum (1996), Moored Observations of Western Boundary Current Variability and Thermohaline Circulation at 26.5° in the Subtropical North Atlantic, *J. Phys. Oceanogr.*, 26(6), 962–983, doi:10.1175/1520-0485(1996)026<0962:MOOWBC>2.0.CO;2.
- Lillibridge III, J. L., and A. J. Mariano (2013), A statistical analysis of Gulf Stream variability from 18+ years of altimeter data, *Deep Sea Research Part II: Topical Studies in Oceanography*, 85, 127–146, doi:10.1016/j.dsr2.2012.07.034.

- Liu, Y., and R. H. Weisberg (2005), Patterns of ocean current variability on the West Florida Shelf using the self-organizing map, *Journal of Geophysical Research: Oceans*, 110(C6), n/a–n/a, doi:10.1029/2004JC002786.
- Liu, Y., R. H. Weisberg, and C. N. K. Mooers (2006a), Performance evaluation of the self-organizing map for feature extraction, *Journal of Geophysical Research: Oceans*, 111(C5), n/a–n/a, doi:10.1029/2005JC003117.
- Liu, Y., R. H. Weisberg, and R. He (2006b), Sea Surface Temperature Patterns on the West Florida Shelf Using Growing Hierarchical Self-Organizing Maps, *Journal of Atmospheric and Oceanic Technology*, 23(2), 325–338, doi:10.1175/JTECH1848.1.
- Liu, Y., R. H. Weisberg, and L. K. Shay (2007), Current Patterns on the West Florida Shelf from Joint Self-Organizing Map Analyses of HF Radar and ADCP Data, *Journal of Atmospheric and Oceanic Technology*, 24(4), 702–712, doi:10.1175/JTECH1999.1.
- Liu, Y., R. H. Weisberg, and Y. Yuan (2008), Patterns of upper layer circulation variability in the South China Sea from satellite altimeter using the Self-Organizing Map, *Acta Oceanologica Sinica*, 27, 129–144.
- Liu, Z., and J. Gan (2012), Variability of the Kuroshio in the East China Sea derived from satellite altimeter data, *Deep Sea Research Part I: Oceanographic Research Papers*, 59, 25–36, doi:10.1016/j.dsr.2011.10.008.
- Li, Y., H. Xue, and J. M. Bane (2002), Air-sea interactions during the passage of a winter storm over the Gulf Stream: A three-dimensional coupled atmosphere-ocean model study, *J. Geophys. Res.*, 107(C11), 3200, doi:10.1029/2001JC001161.
- Marchesiello, P., J. C. McWilliams, and A. Shchepetkin (2001), Open boundary conditions for long-term integration of regional oceanic models, *Ocean Modelling*, 3(1–2), 1–20, doi:10.1016/S1463-5003(00)00013-5.
- Marchesiello, P., J. C. McWilliams, and A. Shchepetkin (2003), Equilibrium Structure and Dynamics of the California Current System, *J. Phys. Oceanogr.*, 33(4), 753–783, doi:10.1175/1520-0485(2003)33<753:ESADOT>2.0.CO;2.
- Marotzke, J., R. Giering, K. Q. Zhang, D. Stammer, C. Hill, and T. Lee (1999), Construction of the adjoint MIT ocean general circulation model and application to Atlantic heat transport sensitivity, *J. Geophys. Res.*, 104(C12), 29529–29547, doi:10.1029/1999JC900236.

- Miller, J. L. (1994), Fluctuations of Gulf Stream frontal position between Cape Hatteras and the Straits of Florida, *J. Geophys. Res.*, *99*(C3), 5057–5064, doi:10.1029/93JC03484.
- Miller, J. L., and T. N. Lee (1995), Gulf Stream meanders in the South Atlantic Bight: 1. Scaling and energetics, *J. Geophys. Res.*, *100*(C4), 6687–6704, doi:10.1029/94JC02542.
- Minobe, S., M. Miyashita, A. Kuwano-Yoshida, H. Tokinaga, and S.-P. Xie (2010), Atmospheric Response to the Gulf Stream: Seasonal Variations, *Journal of Climate*, *23*(13), 3699–3719, doi:10.1175/2010JCLI3359.1.
- Moore, A. M., H. G. Arango, E. Di Lorenzo, B. D. Cornuelle, A. J. Miller, and D. J. Neilson (2004), A comprehensive ocean prediction and analysis system based on the tangent linear and adjoint of a regional ocean model, *Ocean Modelling*, *7*(1–2), 227–258, doi:10.1016/j.ocemod.2003.11.001.
- Moore, A. M., H. G. Arango, E. Di Lorenzo, A. J. Miller, and B. D. Cornuelle (2009), An Adjoint Sensitivity Analysis of the Southern California Current Circulation and Ecosystem, *J. Phys. Oceanogr.*, *39*(3), 702–720, doi:10.1175/2008JPO3740.1.
- Moore, A. M., H. G. Arango, G. Broquet, C. Edwards, M. Veneziani, B. Powell, D. Foley, J. D. Doyle, D. Costa, and P. Robinson (2011a), The Regional Ocean Modeling System (ROMS) 4-dimensional variational data assimilation systems: Part III – Observation impact and observation sensitivity in the California Current System, *Progress in Oceanography*, *91*(1), 74–94, doi:10.1016/j.pocean.2011.05.005.
- Moore, A. M., H. G. Arango, G. Broquet, C. Edwards, M. Veneziani, B. Powell, D. Foley, J. D. Doyle, D. Costa, and P. Robinson (2011b), The Regional Ocean Modeling System (ROMS) 4-dimensional variational data assimilation systems: Part II – Performance and application to the California Current System, *Progress in Oceanography*, *91*(1), 50–73, doi:10.1016/j.pocean.2011.05.003.
- Moore, A. M., H. G. Arango, G. Broquet, B. S. Powell, A. T. Weaver, and J. Zavala-Garay (2011c), The Regional Ocean Modeling System (ROMS) 4-dimensional variational data assimilation systems: Part I – System overview and formulation, *Progress in Oceanography*, *91*(1), 34–49, doi:10.1016/j.pocean.2011.05.004.
- Mujumdar, P. P., and D. N. Kumar (2012), *Floods in a Changing Climate: Hydrologic Modeling*, Cambridge University Press.

- Nelson, J., and R. He (2012), Effect of the Gulf Stream on winter extratropical cyclone outbreaks, *Atmosph. Sci. Lett.*, 13(4), 311–316, doi:10.1002/asl.400.
- Nelson, J., R. He, J. C. Warner, and J. Bane (2014), Air–sea interactions during strong winter extratropical storms, *Ocean Dynamics*, 64(9), 1233–1246, doi:10.1007/s10236-014-0745-2.
- Peña-Molino, B., and T. M. Joyce (2008), Variability in the Slope Water and its relation to the Gulf Stream path, *Geophys. Res. Lett.*, 35(3), L03606, doi:10.1029/2007GL032183.
- Pérez-Hernández, M. D., and T. M. Joyce (2014), Two Modes of Gulf Stream Variability Revealed in the Last Two Decades of Satellite Altimeter Data, *J. Phys. Oceanogr.*, 44(1), 149–163, doi:10.1175/JPO-D-13-0136.1.
- Powell, B. S., H. G. Arango, A. M. Moore, E. Di Lorenzo, R. F. Milliff, and D. Foley (2008), 4DVAR data assimilation in the Intra-Americas Sea with the Regional Ocean Modeling System (ROMS), *Ocean Modelling*, 23(3–4), 130–145, doi:10.1016/j.ocemod.2008.04.008.
- Reusch, D. B., R. B. Alley, and B. C. Hewitson (2007), North Atlantic climate variability from a self-organizing map perspective, *Journal of Geophysical Research: Atmospheres*, 112, D02104, doi:10.1029/2006JD007460.
- Rowe, E., A. J. Mariano, and E. H. Ryan (2013), The Antilles Current. <http://oceancurrents.rsmas.miami.edu/atlantic/antilles.html>.
- Sanchez-Franks, A., and R. Zhang (2015), Impact of the Atlantic meridional overturning circulation on the decadal variability of the Gulf Stream path and regional chlorophyll and nutrient concentrations, *Geophys. Res. Lett.*, 42(22), 2015GL066262, doi:10.1002/2015GL066262.
- Schmeits, M. J., and H. A. Dijkstra (2001), Bimodal Behavior of the Kuroshio and the Gulf Stream, *J. Phys. Oceanogr.*, 31(12), 3435–3456, doi:10.1175/1520-0485(2001)031<3435:BBOTKA>2.0.CO;2.
- Schmitz, W. J., and M. S. McCartney (1993), On the North Atlantic Circulation, *Rev. Geophys.*, 31(1), 29–49, doi:10.1029/92RG02583.

- Shchepetkin, A. F., and J. C. McWilliams (2005), The regional oceanic modeling system (ROMS): a split-explicit, free-surface, topography-following-coordinate oceanic model, *Ocean Modelling*, 9(4), 347–404, doi:10.1016/j.ocemod.2004.08.002.
- Signorini, S. R., and C. R. McClain (2007), Large-scale forcing impact on biomass variability in the South Atlantic Bight, *Geophys. Res. Lett.*, 34(21), L21605, doi:10.1029/2007GL031121.
- Sikirić, M. D., I. Janeković, and M. Kuzmić (2009), A new approach to bathymetry smoothing in sigma-coordinate ocean models, *Ocean Modelling*, 29(2), 128–136, doi:10.1016/j.ocemod.2009.03.009.
- Solidoro, C., V. Bandelj, P. Barbieri, G. Cossarini, and S. Fonda Umani (2007), Understanding dynamic of biogeochemical properties in the northern Adriatic Sea by using self-organizing maps and k-means clustering, *J. Geophys. Res.*, 112(C7), C07S90, doi:10.1029/2006JC003553.
- Srokosz, M. A., and H. L. Bryden (2015), Observing the Atlantic Meridional Overturning Circulation yields a decade of inevitable surprises, *Science*, 348(6241), 1255575, doi:10.1126/science.1255575.
- SSALTO/DUACS User Handbook (2015), SSALTO/DUACS User Handbook: (M)SLA and (M)ADT Near-Real Time and Delayed Time Products,
- Tsui, I.-F., and C.-R. Wu (2012), Variability analysis of Kuroshio intrusion through Luzon Strait using growing hierarchical self-organizing map, *Ocean Dynamics*, 62(8), 1187–1194, doi:10.1007/s10236-012-0558-0.
- Warner, J. C., C. R. Sherwood, H. G. Arango, and R. P. Signell (2005), Performance of four turbulence closure models implemented using a generic length scale method, *Ocean Modelling*, 8(1–2), 81–113, doi:10.1016/j.ocemod.2003.12.003.
- Webster, F. (1961), A description of gulf stream meanders off Onslow Bay, *Deep Sea Research (1953)*, 8(2), 130–143, doi:10.1016/0146-6313(61)90005-3.
- Werner, F. E., J. A. Quinlan, B. O. Blanton, and R. A. Luetich Jr. (1997), The role of hydrodynamics in explaining variability in fish populations, *Journal of Sea Research*, 37(3–4), 195–212, doi:10.1016/S1385-1101(97)00024-5.

- Wunsch, C. (1996), *The Ocean Circulation Inverse Problem*, Cambridge University Press, Cambridge ; New York.
- Wunsch, C. (2006), *Discrete Inverse and State Estimation Problems: With Geophysical Fluid Applications*, Cambridge University Press, Cambridge ; New York.
- Xie, L., X. Liu, and L. J. Pietrafesa (2007), Effect of Bathymetric Curvature on Gulf Stream Instability in the Vicinity of the Charleston Bump, *J. Phys. Oceanogr.*, 37(3), 452–475, doi:10.1175/JPO2995.1.
- Yin, Y., X. Lin, Y. Li, and X. Zeng (2014), Seasonal variability of Kuroshio intrusion northeast of Taiwan Island as revealed by self-organizing map, *Chin. J. Ocean. Limnol.*, 32(6), 1435–1442, doi:10.1007/s00343-015-4017-x.
- Zeng, X., Y. Li, R. He, and Y. Yin (2015a), Clustering of Loop Current patterns based on the satellite-observed sea surface height and self-organizing map, *Remote Sensing Letters*, 6(1), 11–19, doi:10.1080/2150704X.2014.998347.
- Zeng, X., Y. Li, and R. He (2015b), Predictability of the Loop Current Variation and Eddy Shedding Process in the Gulf of Mexico Using an Artificial Neural Network Approach, *J. Atmos. Oceanic Technol.*, 32(5), 1098–1111, doi:10.1175/JTECH-D-14-00176.1.

## Figures

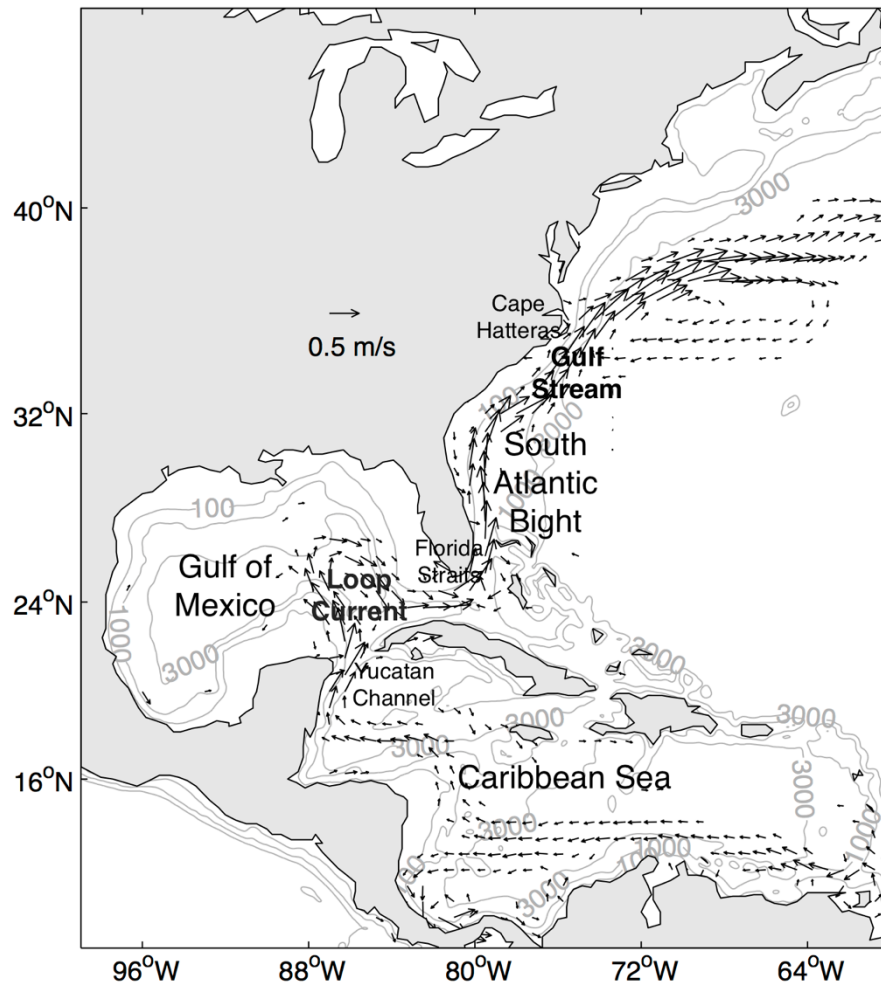


Figure 1. Model domain. Black arrows are geostrophic currents ( $> 0.1$  m/s) derived from 21 years of mean AVISO Absolute Dynamic Topography data. They can be considered as the western boundary current system in the North Atlantic. Contours are 100, 1000, and 3000 m isobaths.

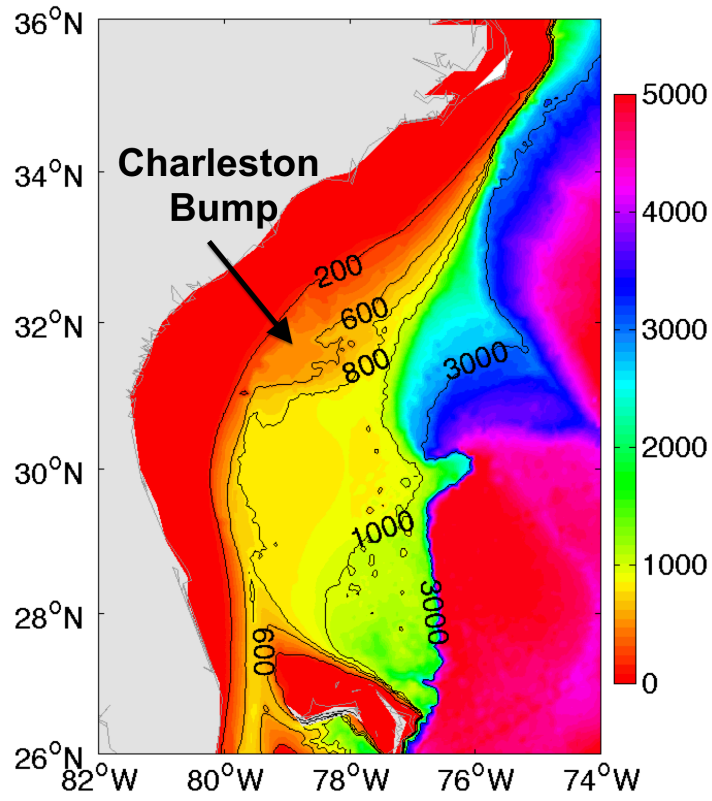


Figure 2. Topography of the South Atlantic Bight. Water depth is shown in meters and extracted from the 1-minute GEBCO dataset. The Charleston Bump is indicated.

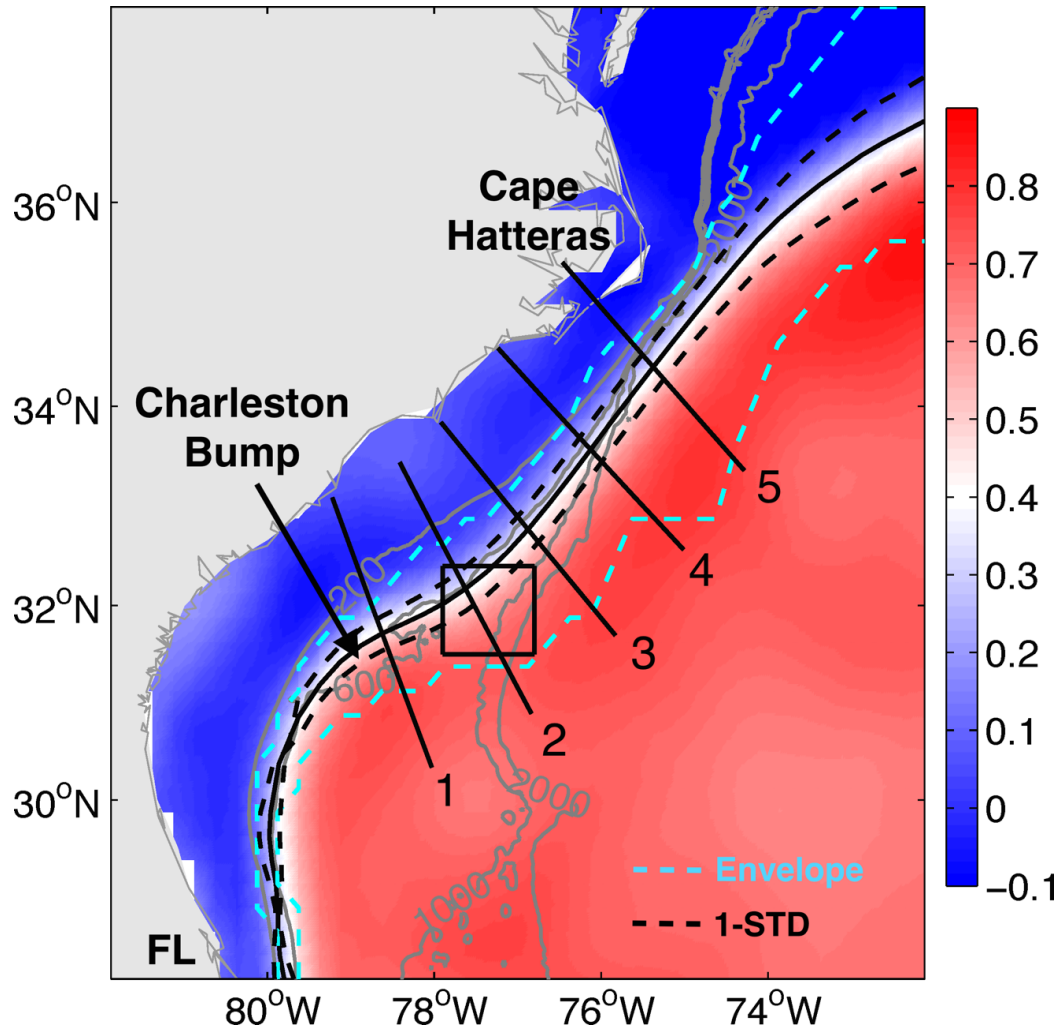


Figure 3. Long-term (1993-2013) mean Absolute Dynamic Topography (ADT, color shading, unit: m) overlaid with Gulf Stream mean path (solid black curve) and corresponding envelope (dashed cyan curves) and one standard deviation (STD, dashed black curves). Transects 1 to 5 (solid lines perpendicular to the Gulf Stream mean path) were used to measure the position variation of the Gulf Stream. Gray contours are 200, 600, 1000, and 2000 m isobaths. Black box is for the index function definition in section 3. Florida (FL) and the Charleston Bump are indicated.

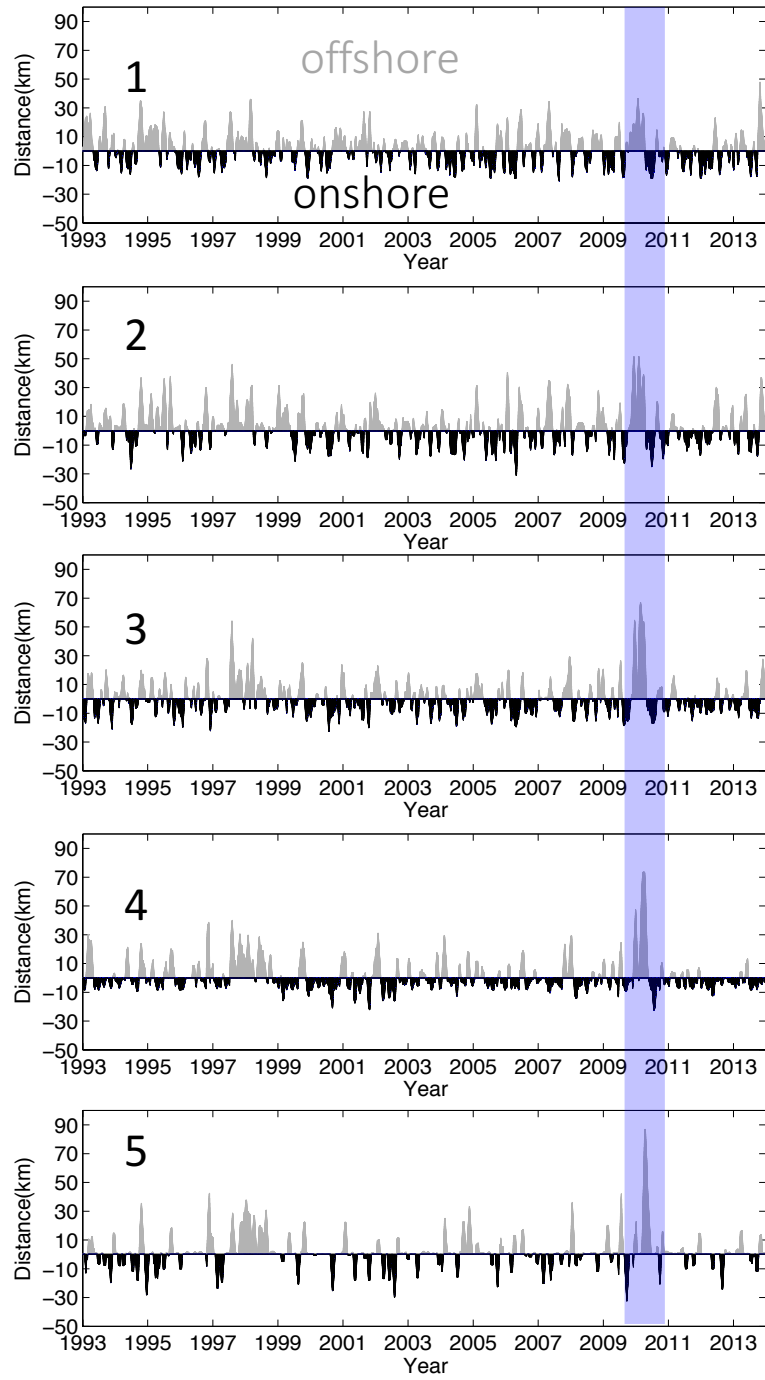


Figure 4. Gulf Stream position relative to its mean path along each transect in Figure 3 (unit: km). Offshore direction is positive (gray), while onshore is negative (black). Blue shaded region indicates the largest offshore event in 2009-2010. A 30-day low-pass filter was applied to the original data for visualization purpose.

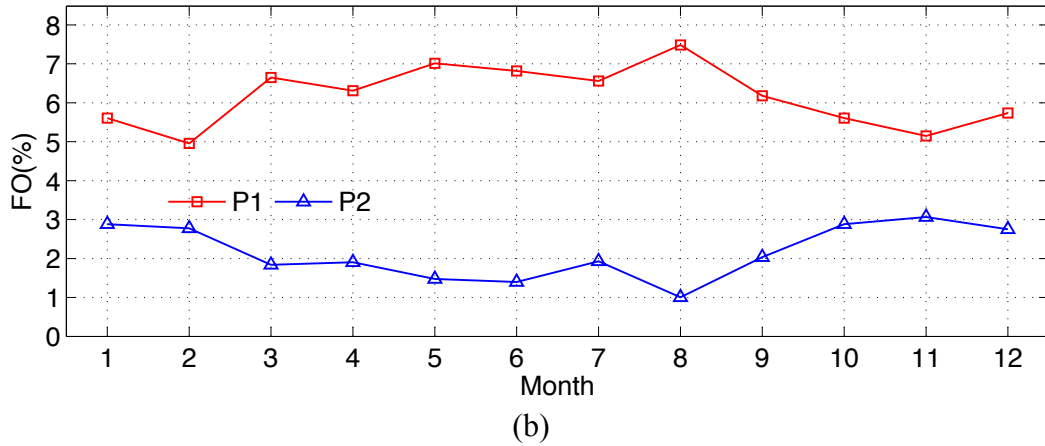
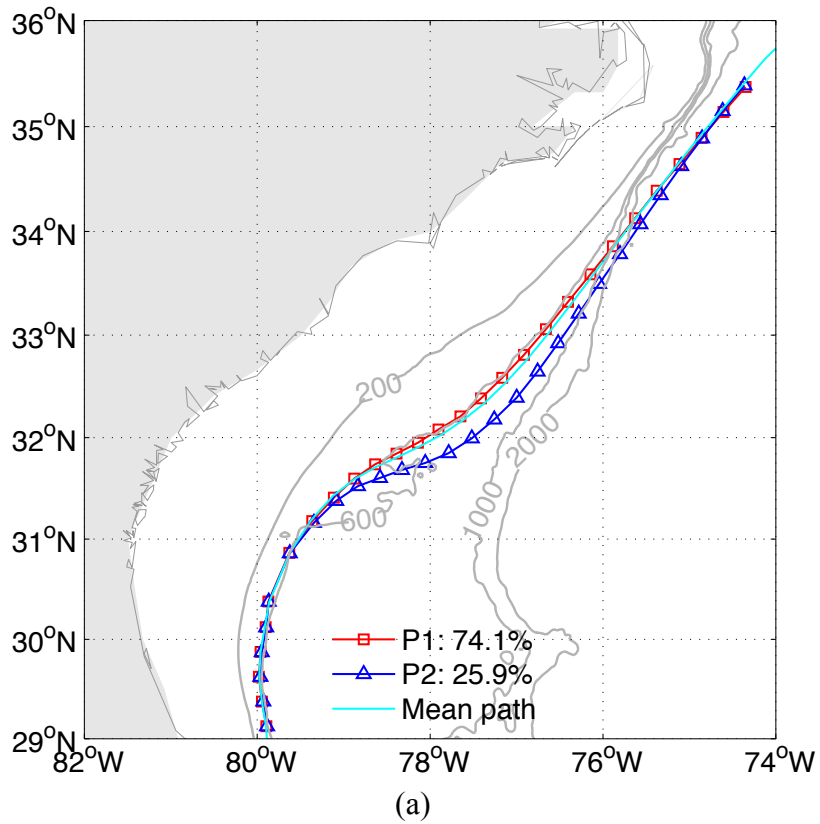
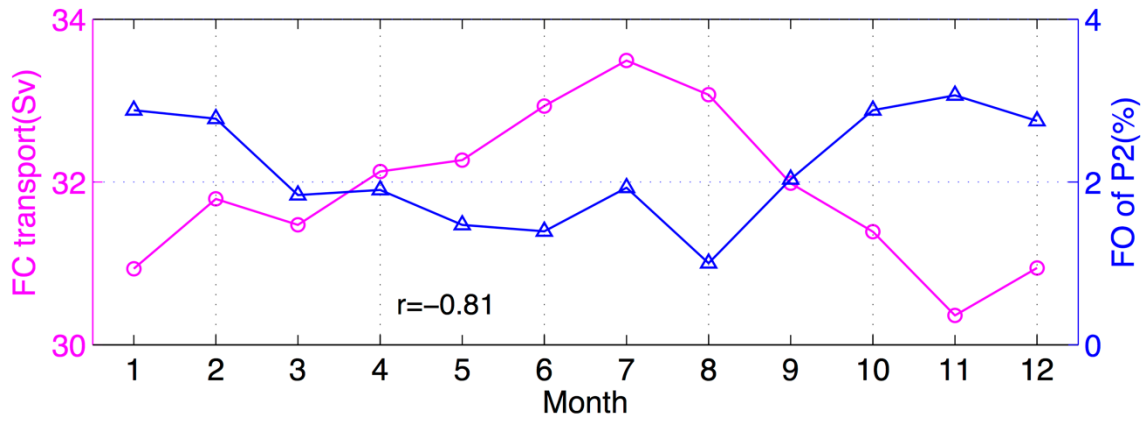
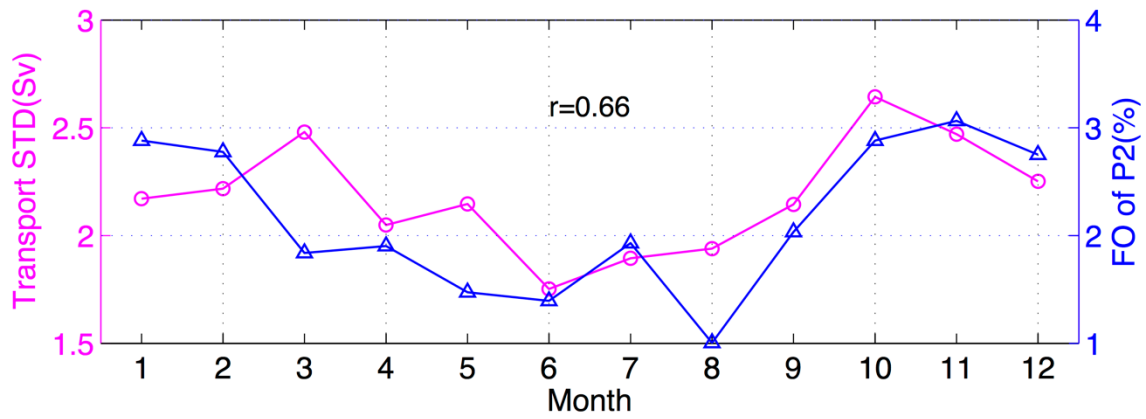


Figure 5. Self-Organizing Map analysis of the Gulf Stream path in the South Atlantic Bight. (a) Weakly (P1) and strongly (P2) deflected patterns. The numbers are corresponding frequency of occurrence (FO) for each pattern. The mean path is indicated by the cyan curve. (b) Monthly FOs of the two patterns in (a).

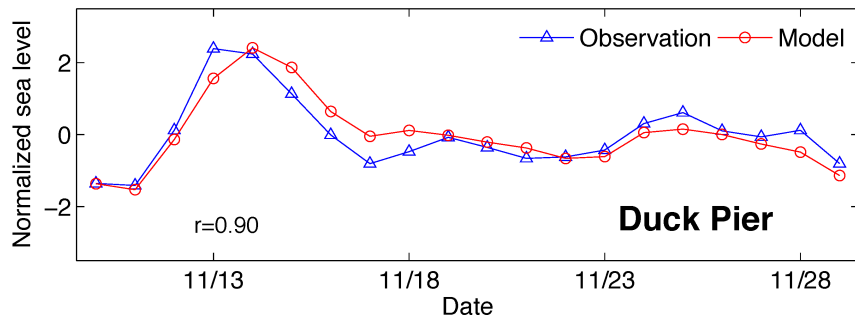


(a)

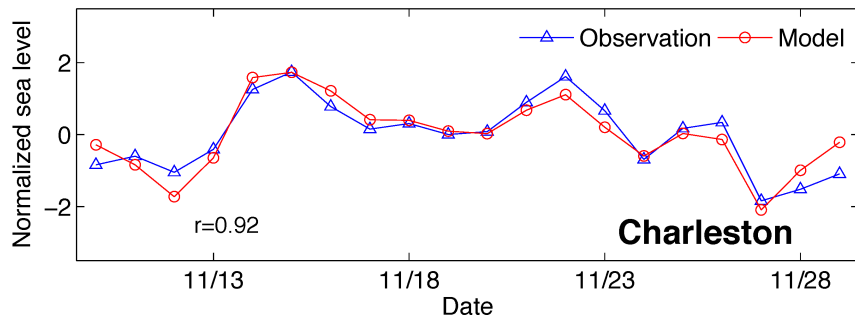


(b)

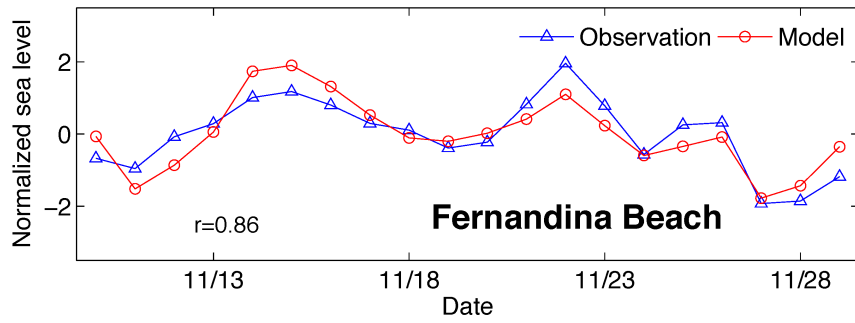
Figure 6. Comparisons between Florida Current (FC) transport and monthly FO of strongly deflected pattern (P2). (a) Monthly mean FC transport (Sv) and FO of P2 (%). Correlation coefficient is -0.81. (b) Monthly standard deviation (STD) of FC transport (Sv) and FO of P2 (%). Correlation coefficient is 0.66.



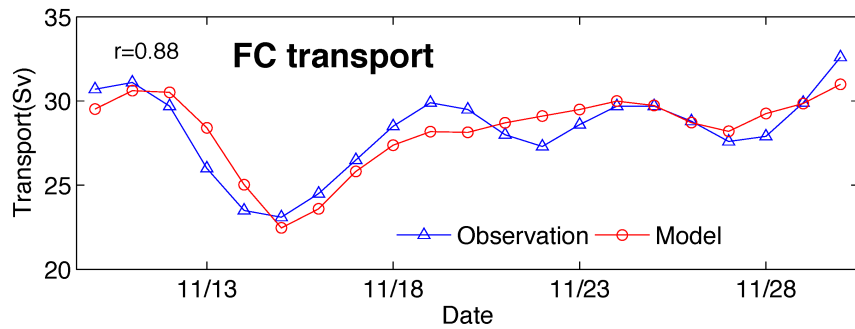
(a)



(b)



(c)



(d)

Figure 7. Observed (blue) and simulated (red) daily sea level at three stations (a, b, and c) along the SAB, and water transport through the Florida Straits (d). Sea level data are normalized (minus mean divided by the corresponding standard deviation). Locations of the three stations and the FC transect is shown in Figure 8a.

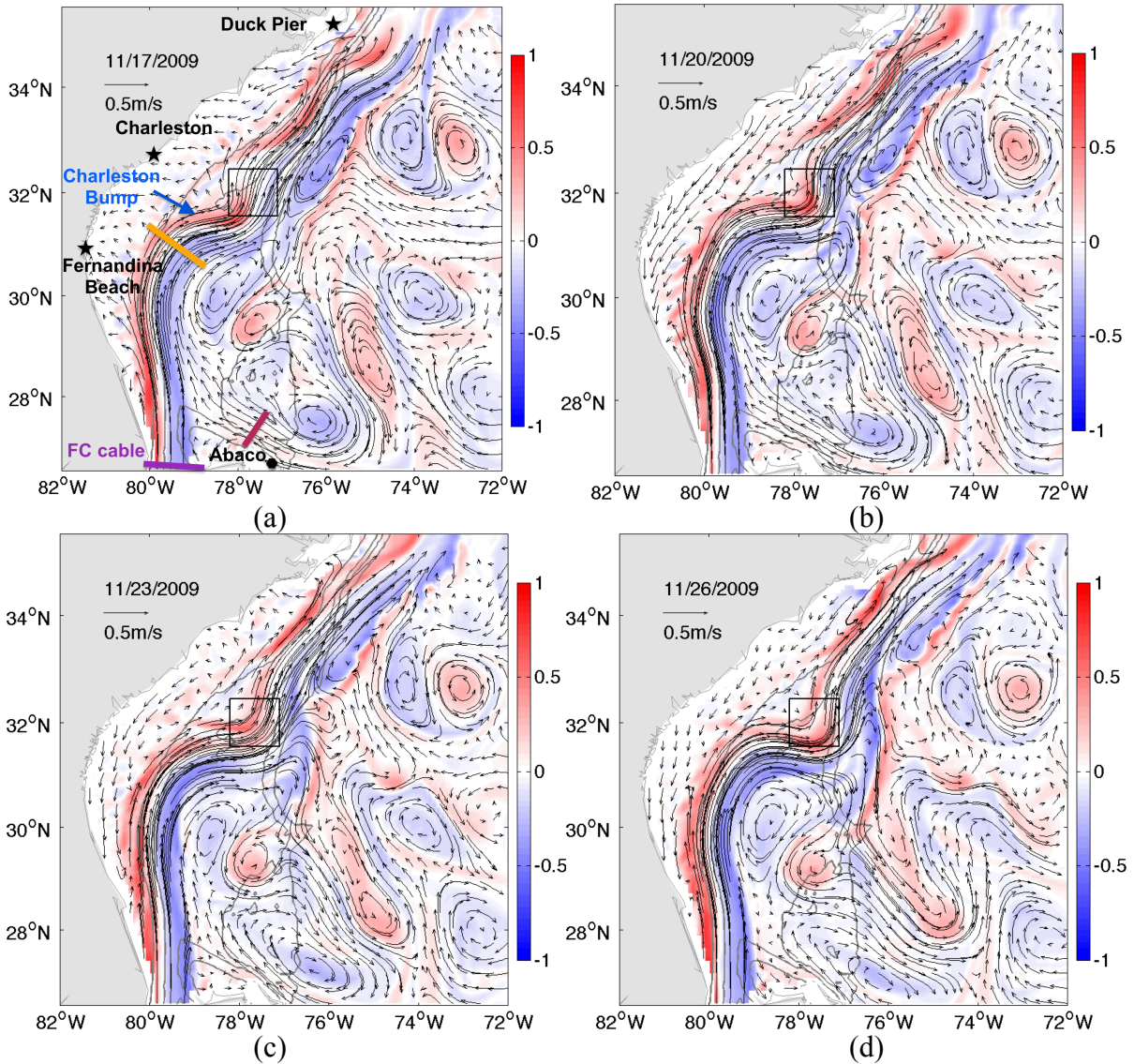


Figure 8. Simulated surface velocity (vectors) and relative vorticity (color shading) from Nov. 17 to 26, 2009, every three days. Relative vorticity is normalized by dividing by the Coriolis parameter. Black stars in (a) indicate the location of the three sea level stations, and black hexagon represents Abaco Island. Purple solid line in (a) represents the location of the cable measuring the Florida Current (FC) transport. Black box (same as the one in Figure 3) delineates the region for index function calculation. Gray lines are the 200, 600, 1000, and

2000 m isobaths. The purple, red, and yellow transects in (a) are sites where water transport was calculated for the FC, Antilles Current, and Gulf Stream, respectively.

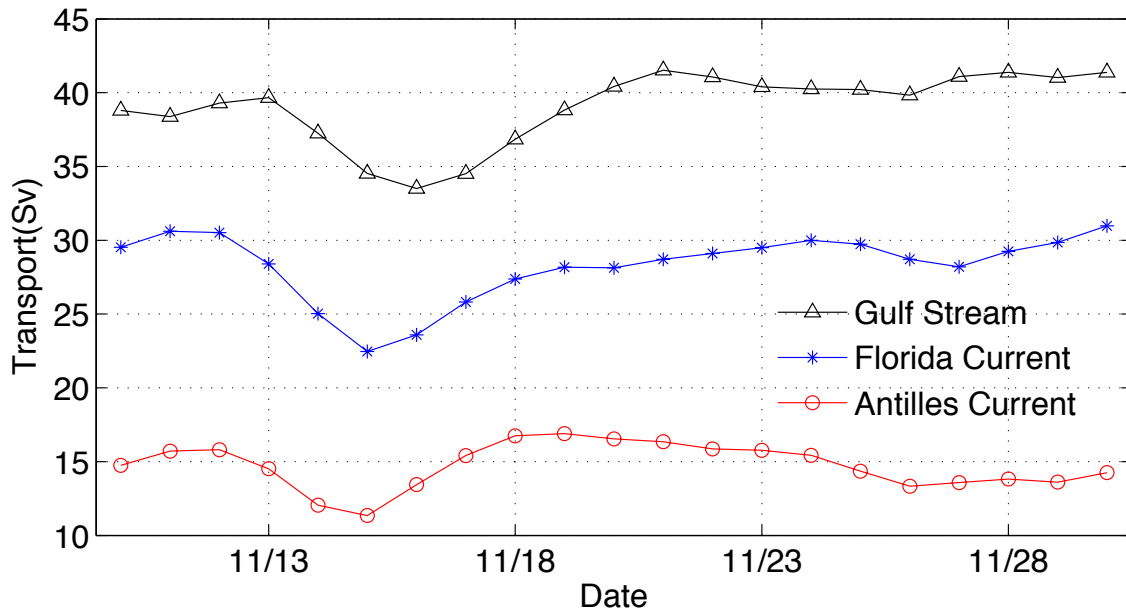
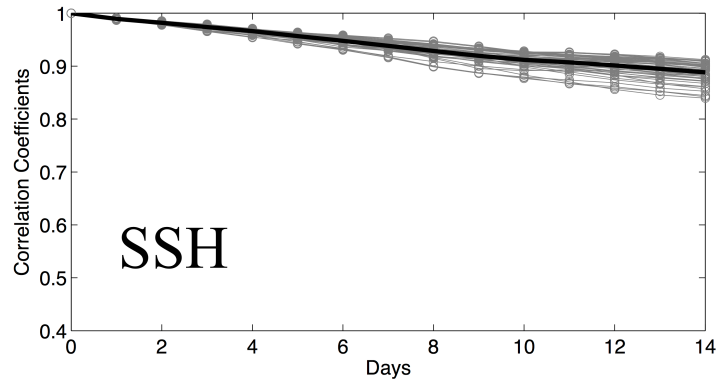
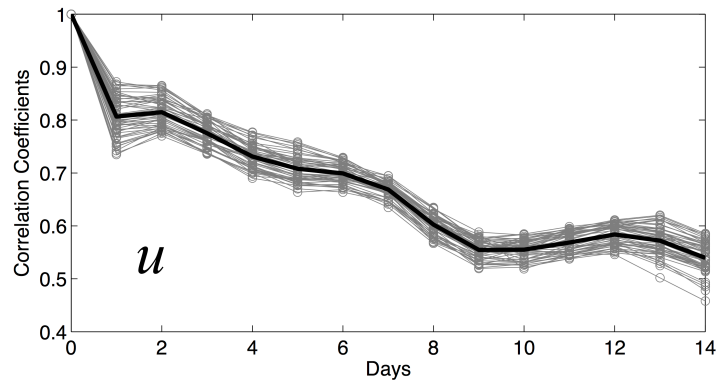


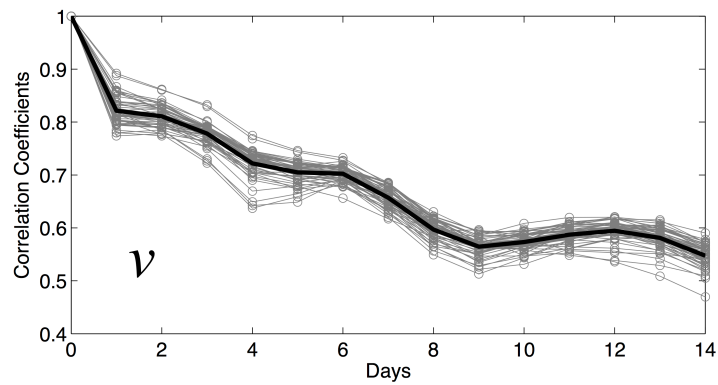
Figure 9. Simulated water transport through the three transects in Figure 8a. These indicate the water transport of Florida Current, Antilles Current, and Gulf Stream.



(a)



(b)



(c)

Figure 10. Comparisons between the nonlinear perturbation runs and tangent linear model solutions in terms of sea surface height (SSH) and velocity ( $u$  and  $v$ ). Gray lines represent the 50 perturbation experiments, and solid black lines are the corresponding mean.

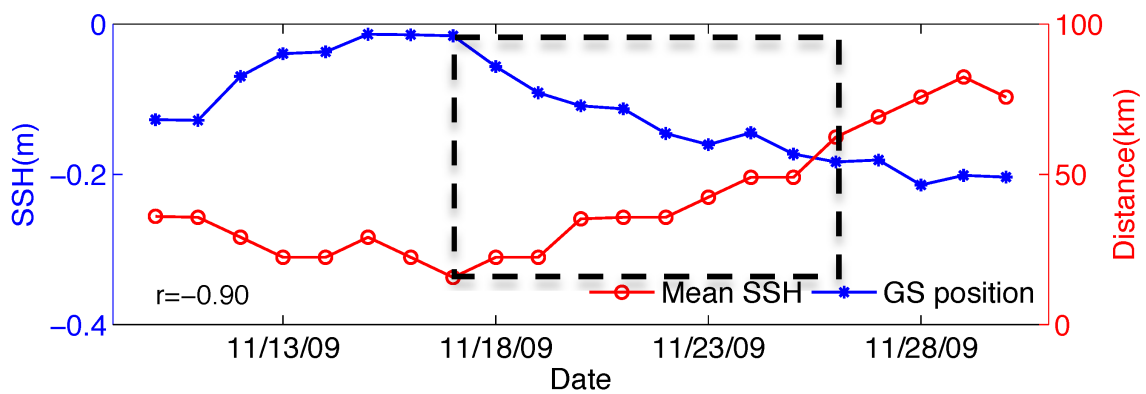


Figure 11. Comparison between daily mean sea surface height (SSH, blue) in the box and Gulf Stream (GS) position (red) relative to the mean path along transect 2 in Figure 3. The dashed rectangular box indicates the time window for adjoint sensitivity analysis.

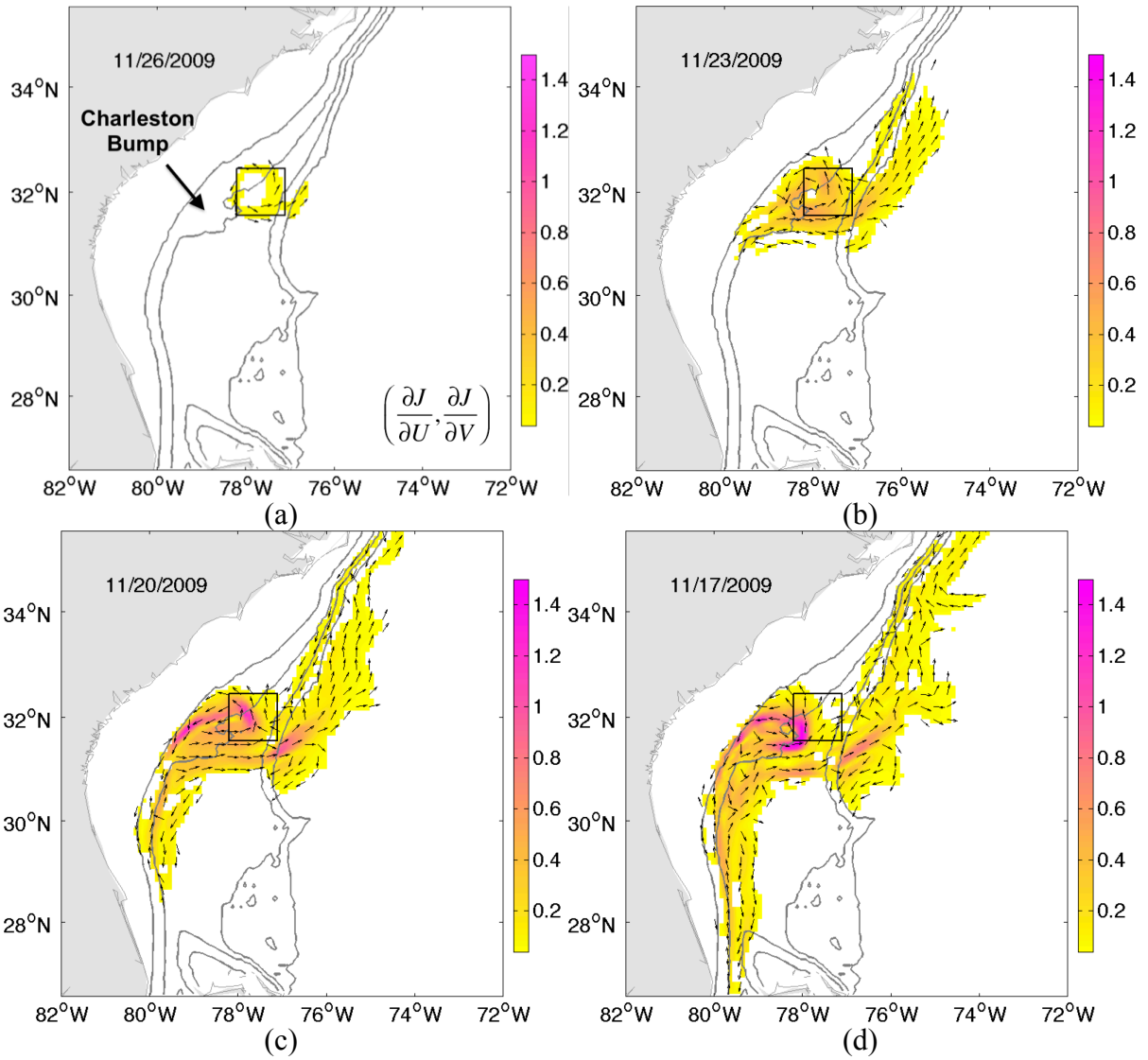
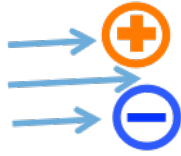


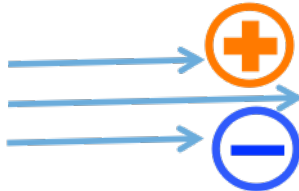
Figure 12. Adjoint sensitivity to depth-averaged velocity. Vectors represent direction. Color indicates magnitude (unit: 1/s). Gray lines are the 200, 600, 1000, and 2000 m isobaths.

Black boxes are the region for index function calculation.

**(a) Gulf Stream Jet (normal)**



**(b) Increased transport without Bump**



**(c) Increased transport with Bump**

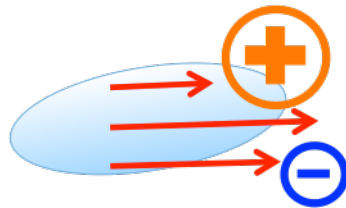


Figure 13. Schematics of positive relative vorticity perturbation formation. Orange circles with plus signs indicate positive relative vorticity. Blue circles with minus signs represent negative relative voracity. Vectors are velocity fields. Shaded ellipse represents the Charleston Bump.

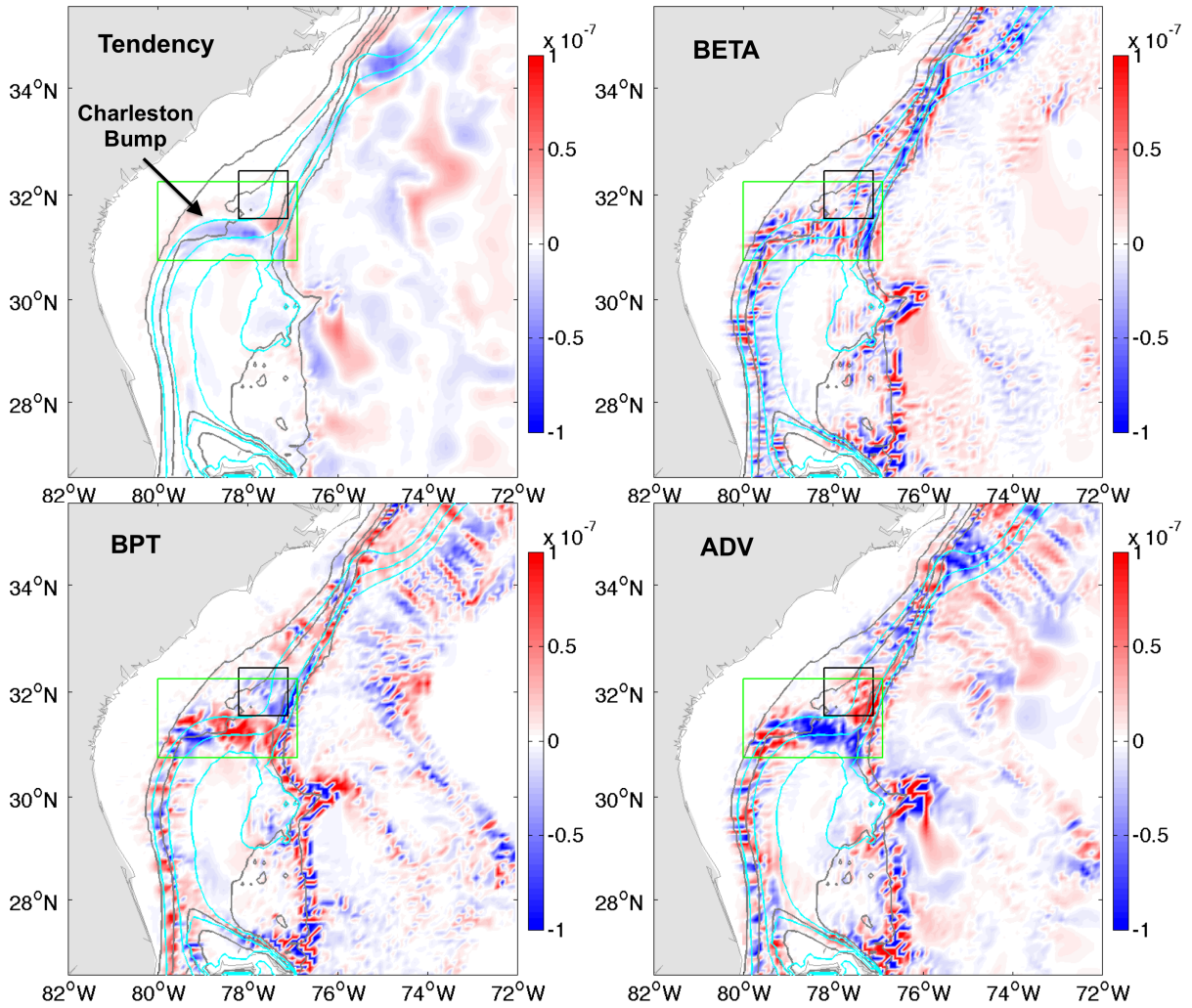


Figure 14. Ten-day (Nov. 17-26, 2009) averaged tendency, planetary vorticity advection (BETA), bottom pressure torque (BPT), and nonlinear advection (ADV) terms in the barotropic vorticity equation (unit:  $\text{m/s}^2$ ). Gray lines are the 200, 600, 1000, and 2000 m isobaths. Cyan lines are the 1, 21, and 41 Sv barotropic streamlines (integrated from coastlines). Green boxes define the region for the time series plot in Figure 16. Black boxes indicate the region for the index function calculation.

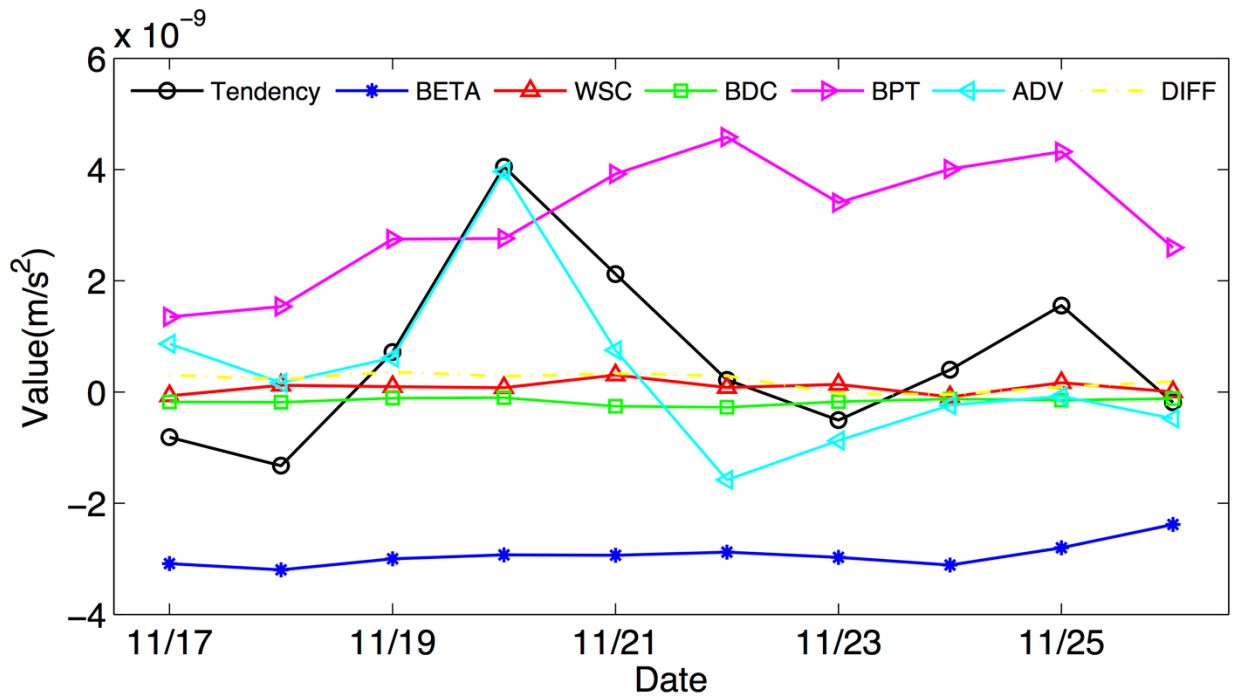


Figure 15. Spatial averaged terms of the barotropic vorticity equation (Eq. 11) within the green box in Figure 14 (unit:  $m/s^2$ ).

## Chapter V: Summary

As one of the most prominent features of ocean circulation in the North Atlantic, the Western Boundary Current system has drawn and will continue drawing research interests in the ocean science community. Many previous studies have focused on the large scale West Boundary Current dynamics, air-sea interactions, influence on marine ecosystem, and impacts on the climate system. This dissertation examined two components of the Western Boundary Current system in regional settings: the Loop Current (LC) in the Gulf of Mexico (GoM) and the Gulf Stream (GS) in the South Atlantic Bight (SAB). Focuses were on the long-term patterns of the flow system, their predictability and mechanisms triggering the variation.

The first part of this dissertation documented an analysis of two decades' satellite altimetry data using the Self-Organizing Map (SOM) method. Three patterns and their corresponding temporal evolution of LC sea surface height (SSH) were extracted. As revealed by the SOM analysis, in most cases, the LC evolution follows a normal–extension–retraction cycle. Transitions from normal pattern to extension pattern and from extension pattern to retraction pattern mainly occur in June and the end of August, respectively. The weekly frequency of occurrence (FO) analysis of the LC retraction pattern indicates that the increase of wind stress curl in the Caribbean Sea from June to November favors the LC eddy shedding during that period. On the interannual time scale, a significant relationship between Oceanic Nino Index and annual FO of the LC retraction pattern exists, suggesting a possible teleconnection between Pacific climate and LC eddy shedding frequency, which requires further investigation.

With better understanding of the LC variation from the SOM analysis, the second part of this dissertation presented a novel approach to predict LC variation and its eddy shedding process in the GoM based on an artificial neural network and empirical orthogonal function (EOF) analysis method. The methodology is a three-step procedure: the EOF analysis method was first applied on two decades' satellite altimetry SSH data to decompose the SSH data into spatial patterns (EOFs) and time-dependent principal components (PCs). Then the nonlinear autoregressive neural network was used to predict leading PCs of the GoM SSH six weeks ahead. Finally, the future SSH of the GoM was constructed by multiplying the spatial EOFs of the GoM SSH and the predicted PCs. The sensitivity of prediction results to different variance percentage levels were tested, and the 95% level (with 18 PCs) was selected for skill assessment and analysis. To independently evaluate the prediction skill of this methodology, weekly predictions, each with 6-week sliding prediction window were continuously performed over 3 years. The spatial correlation coefficients and root mean square errors (RMSEs) between predicted and observed SSH during the 3 years were calculated. Several other skill assessment metrics between prediction and persistence, such as the SSH skill score and RMSE, and the frontal position RMSE of the LC and LC eddies were also evaluated. For SSH prediction, the 3-year mean RMSE of prediction is about 30% less than that of persistence at week 6. The 3-year mean skill score of SSH prediction is about 0.5 compared to 0.1 for persistence at week 6. The RMSE of the frontal position also shows better skill of prediction (60 km) over persistence (80 km). Generally, the model can accurately capture the LC variation and eddy shedding process 4 weeks ahead, and in some cases, 5 and 6 weeks ahead is possible.

The third part of this dissertation focused on the variability of the GS in the SAB. The variation of GS path was first evaluated using satellite altimeter data in the last two decades, and clustered using the SOM. The variability of the GS cross-shelf position generally increases from the Florida Straits to Cape Hatteras. Consistent with previous studies, two patterns: the weakly and strongly deflected patterns of the GS are identified. Overall, the weakly deflected pattern happens more frequent than the strongly deflected pattern. The strongly deflected pattern is more likely to occur in winter when the water transport through the Florida Straits is relatively low but the corresponding variability is high. Over the last two decades, the largest GS offshore meander occurred in November 2009 - April 2010. To explore the triggering mechanism of this extreme meander event, a forward ocean model was developed to hindcast the circulation. In addition, adjoint sensitivity analysis was applied to elucidate the dynamics and ocean state structures during a ten-day window (Nov. 17-26, 2009). The sensitivity of GS offshore meander to the depth-averaged velocity field shows an increase in the ocean volume and velocity along the GS core path, which interacts with the local bathymetry (Charleston Bump) to generate asymmetric velocity shear. As a result, a net increase of positive relative vorticity occurs, forcing the GS to move further offshore in order to conserve the potential vorticity of the flow field. Tracking back to upstream, this process corresponds to the water transport increase through the Florida Straits starting from Nov. 15, 2009. Quantitative barotropic vorticity budget analysis further confirms such a finding.

Despite long-term satellite data observation and advance of numerical modeling, understanding and accurately predict instabilities of the Western Boundary Current system

will remain a big challenge in oceanography. This work is an initial attempt to embrace this challenge. Further progress will require advanced data assimilation methodologies combined with comprehensive observing systems that can observe both regional and basin scale ocean states, as well as provide direct measurements of both surface and subsurface conditions of boundary currents.